skb.se

SKB TR-25-03

ISSN 1404-0344
ID 2074572
August 2025

The glacially induced stress field in Forsmark

Simulations with past and future ice sheet models and various earth models

Peter Schmidt, Björn Lund
Uppsala University

Keywords: Glacial isostatic adjustment, Glacially induced stress, Forsmark

Summary

In this study we have simulated the evolution of stresses induced in the crust beneath Forsmark, Sweden, using reconstructions of the Saale and Weichselian glaciations as well as three scenarios of future glaciation. For each ice sheet, five different Earth models have been used. The main focus of this report is on the stress evolution at Forsmark at 500 m depth, the location of the future nuclear waste repository.

The present study is in many ways a continuation of the study by Lund et al. (2009), which focused on a particular reconstruction of the Weichselian glaciation and the effects of that glaciation on the stress and fault stability evolution at Forsmark. Here we extend the stress part of that study by adding four more ice sheet simulations and by investigating the effect of those ice sheets on five different earth models. In addition, we study the effect of a prolonged residence time of the ice sheet at glacial maximum by introducing hiatuses of 25 kyr and 50 kyr at that time. We also investigate the impact of multiple glaciations on the stress field. We use a methodology similar to that of Lund et al. (2009), a glacial isostatic adjustment (GIA) simulation using a flat-earth finite element formulation based on Wu (1992, 2004) and Schmidt et al. (2012).

The five ice models we study are (i) the Weichselian reconstruction (SKB 2010) used in Lund et al. (2009), (ii) a transient evolution of the large Saalian glacial cycle (Colleoni and Liakka 2020), (iii) a future projection of ice evolution where the governing temperatures are based on CO_2 -levels using the Representative Concentration Pathway 4.5 (RCP 4.5) until the year 2300 and then a fast CO_2 decline onward (Thölix et al. 2019), (iv) the same RCP 4.5 scenario until the year 2300 followed by a slow CO_2 decline (Thölix et al. 2019) and (v) using the RCP 8.5 scenario to the year 2300 followed by a slow CO_2 decline (Thölix et al. 2019). The latter three ice models start in the year 2010 and evolve 120 thousand years into the future. These five ice models cover a wide range of glacial sizes, thicknesses and evolutions in Fennoscandia. We combine the ice models with five earth models with varying thicknesses of the mechanically strong lithosphere and various mantle viscosities, in order to cover a range of plausible models for the earth structure in and around Forsmark.

As expected, in our 25 GIA simulations we find that the ice models are the first order drivers of the evolution of the stress field induced in the crust. The different earth models modulate the stresses, in magnitude and also to some degree in the timing of the development. Comparing the regional patterns of the direction and magnitude of the maximum horizontal stress we find that for a particular ice model, the regional stress distribution is rather similar between earth models, with some differences mostly around the outer parts of the ice sheet. The glacially induced vertical stress is directly proportional to the local weight of the ice column. The horizontal stresses depend on the flexure of the lithosphere, which in turn depends on the elastic and rheological parameters of the earth model. The maximum horizontal stress tends to grow to magnitudes similar to the maximum vertical stress, if the ice resides long enough at a particular configuration. During glacial periods, none of the earth models used here produce horizontal stresses which are more than a few MPa larger than the maximum vertical stress and most models never reach horizontal stresses as large as the vertical stress. In the models in this study we found a maximum compressive horizontal stress of 30.4 MPa at 500 m depth in Forsmark. Tensional induced horizontal stresses develop around the edges of a stationary ice sheet, and can also develop at ice free locations as an ice sheet advance toward them. In this study we found up to 11.4 MPa induced tensional stress at 500 m depth in Forsmark.

We studied how displacement and stress evolve if the glacial maximum is extended for longer time periods, with the same resident ice volumes. The results show that none of the earth models are in isostatic equilibrium at the original glacial maximum but that subsidence and horizontal stresses continue to increase with residence time, even after a 50 kyr hiatus. We also investigated what effect a prior glaciation has on the stress and displacements during the next glaciation. There is, naturally, a significant initial difference, which depends on the time between glaciations and the viscosity of the earth model. The effect decreases during growth of the next ice sheet and is generally very small (up to about 1 MPa depending on earth model) at the next glacial maximum.

Stress data from beneath Forsmark accompany this report. For each of the 25 + 18 ice-earth combinations (excluding the case of multiple glaciations), data is provided at 1 km intervals from 500 m to 14.5 km depth, for every 1000 year throughout the simulations.

Sammanfattning

I detta arbete har vi simulerat hur spänningarna i jordskorpan utvecklas under en nedisning. Vi har använt modeller av både Saale och Weichselisarna samt tre modeller av tänkbara framtida nedisningar. Varje ismodell har använts tillsammans med fem olika jordmodeller för att också studera jordmodellens inverkan på spänningsutvecklingen. Fokus för rapporten ligger på spänningsutvecklingen på 500 m djup i det framtida slutförvaret för använt kärnbränsle i Forsmark.

Den här studien är på många sätt en fortsättning av arbetet i Lund et al. (2009) som undersökte spänningar inducerade i jordskorpan av Weichselisen och hur dessa påverkar förkastningars stabilitet. Här utökar vi spänningsdelen av det arbetet genom att undersöka ytterligare fyra olika ismodeller och hur de samverkar med fem olika jordmodeller. Dessutom studerar vi effekten på spänningstillståndet av en förlängning av den tid då isarna befinner sig i maximal storlek med 25 000 respektive 50 000 år. Vi undersöker även hur återkommande nedisningar påverkar spänningarna. Vi använder en metodik liknande den in Lund et al. (2009) genom att simulera hur jorden isostatiskt svarar på nedisning i platta jordmodeller, efter Wu (1992 2004) och Schmidt et al. (2012).

De fem ismodeller vi använder är (i) den Weichselrekonstruktion (SKB 2010) som användes i Lund et al. (2009), (ii) en transient utveckling av den stora Saale-isen mellan 240 till 135 tusen år före nutid (Colleoni and Liakka 2020), (iii) en framtida isutveckling där temperaturen bestäms av CO_2-nivåer enligt IPCC:s ”Representative Concentration Pathway 4.5” (RCP 4.5) fram till år 2300 och sedan en snabb minskning av CO_2 (Thölix et al. 2019), (iv) Samma RCP 4.5-scenario men med en efterföljande långsam minskning av CO_2 (Thölix et al. 2019) och (v) RCP 8.5 modellen till år 2300 och sedan en långsam minskning av CO_2 (Thölix et al. 2019). De tre senare ismodellerna startar år 2010 och varar i 120 000 år framåt. Dessa fem ismodeller spänner över glaciationer med mycket olika storlekar, tjocklekar och utvecklingar. Ismodellerna kombineras med fem olika jordmodeller med varierande tjocklek av den mekaniskt starka delen av litosfären och varierande mantelviskositet för att utvärdera olika möjliga modeller av jordens egenskaper runt och under Forsmark.

Som förväntat visar våra 25 simuleringar att glaciationens utveckling till första ordningen bestämmer hur spänningsfältet i jordskorpan utvecklas. De olika jordmodellerna modulerar spänningarna, i storlek men också delvis i tidsutvecklingen. På en regional skala, för en specifik ismodell, är både riktning och storlek av den största horisontella spänningen relativt lika mellan olika jordmodeller, de största skillnaderna återfinns i istäckets ytterkanter. Den isinducerade vertikala spänningen är direkt proportionell mot den lokala islasten. De inducerade horisontella spänningarna beror på hur litosfären böjer sig under lasten, vilket beror av jordmodellens elastiska och reologiska egenskaper. Den maximala horisontella spänningen växer till en storlek liknande den vertikala spänningen, om isen ligger oförändrad under tillräckligt lång tid. Ingen av de jordmodeller vi studerat här producerar horisontella spänningar som är mer än några megapascal större än den vertikala spänningen och i de flesta simuleringarna når de horisontella spänningarna aldrig samma storlek som de vertikala under glaciala perioder. Våra simuleringar ger en maximal horisontell kompressiv spänning om 30,4 MPa vid 500 m djup i Forsmark. Horisontella dragspänningar induceras runt kanterna på en stationär is och även på vissa isfria platser när istäcket avancerar mot dessa. I våra simuleringar finner vi upp till 11,4 MPa inducerad dragspänning på 500 m djup i Forsmark.

Vi undersöker hur de inducerade spänningarna påverkas om isarna skulle ligga under långa tidsperioder med sin maximala utsträckning och tjocklek. Resultaten visar att ingen av jordmodellerna kommer i isostatisk jämvikt vid det glaciala maximat i ismodellernas originalform, landsänkning och horisontella spänningar fortsätter att öka med längre liggtid, även efter 50 000 års stillestånd. Vi undersöker också vilka effekter en tidigare nedisning har på hur rörelser och spänningar utvecklas under nästa nedisning. Vi ser en signifikant effekt under den tidiga delen av nästa glaciation, som beror av tiden mellan de två nedisningarna och jordens viskositet. Effekten minskar när nästa is växer till och är generellt sett mycket liten vid nästa glaciala maximum, upp till cirka 1 MPa beroende på jordmodell.

Den här rapporten åtföljs av digitalt data för de glacialt inducerade spänningarna. För varje simulering (25 + 18 is-jordkombinationer, utom de för multipla nedisningar) finns data för Forsmark från 500 till 14,5 km djup med intervaller om en kilometer och 1000 år.

Content

1 Introduction

Spent nuclear fuel is potentially hazardous for hundreds of thousands of years, a time frame which in Fennoscandia is enough that one, or more, continental ice sheets may cover the repository for some time. It is therefore important to assess how a large ice sheet affects the stresses in the repository rock mass, both from a construction point of view and in order to evaluate if those stresses may cause rapid fault motion, i.e. earthquakes. In this report we use numerical modelling to investigate the stresses induced in five different models of the Earth using five different ice sheet evolutions, with different areal extents, different total ice volumes and different ice thicknesses over Forsmark. A previous SKB study on the effect of a Weichselian ice sheet on stresses and fault stability at Forsmark (Lund et al. 2009, L2009 hereafter) used one particular ice sheet reconstruction based on the University of Main Ice-Sheet Model (UMISM - SKB 2010). The current study includes results with the UMISM reconstruction, and adds one ice sheet simulation of the much larger Saalian ice sheet (Colleoni and Liakka 2020) and three simulations into the future, using the climate evolution models Representative Concentration Pathway (RCP) 4.5, RCP 4.5e and RCP 8.5 as starting points (Thölix et al. 2019).

The process by which the solid earth responds to a glacial load on its surface is called Glacial Isostatic Adjustment, GIA. Using a simplified description, the Earth can be considered to consist of an outer elastic shell, the mechanically strong lithosphere, surrounding a viscoelastic medium in the interior, the mantle. To complicate the picture, the thickness of the outer elastic shell is known to vary laterally and in addition, the rheological parameters also vary both laterally and with depth. On short time scales, less than a year, the immediate response of the Earth to changes in the glacial load will be elastic while on long time scales, thousands of years, it approaches that of a viscous medium overlain by an elastic layer. Estimates of the viscosity in the uppermost regions of the mantle ranges from 10^{21}-10^{22} Pa s beneath cratonic regions (e.g. Mitrovica et al. 2007, Steffen and Wu 2011, Schmidt et al. 2014) down to 10^{19} beneath mid-oceanic ridges and in hotspots (e.g. Schmidt et al. 2013). As a consequence, in cratonic regions covered by ice sheets during the last ice age, such as Fennoscandia, adjustment is still ongoing today, some 10 000 years after the end of glaciation, with uplift velocities in excess of 10 mm/yr (e.g. Kierulf et al. 2021). In regions underlain by a mantle with an elevated temperature, e.g. Iceland, the GIA process may have finished as soon as 1000 years after the deglaciation (e.g. Sigmundsson 1991). During growth of an ice sheet, stresses in the subsurface below the load will increase. In the viscoelastic mantle this will cause a flow of mantle material down- and outwards from the region directly beneath the growing ice sheet, causing the loaded surface to subside. The flow of material at depth will at the same time cause regions at a distance to be uplifted, commonly referred to as a fore-bulge. Conversely, during times of decay of the ice sheet, stresses in the subsurface will decrease, causing the region that was depressed to start uplift while the fore-bulge will initially uplift further due to elastic expansion of the compressible earth and then collapse/subside. However, important to note here is that as areal extent changes during the waxing and waning of the ice sheet, the node-line (separator between uplifted and subsided regions) will migrate. Thus, the vertical displacement at a site located away from the centre of the ice sheet or outside the ice margin, may, during the course of a glacial cycle, include periods of subsidence as well as periods of uplift. Further, due to the high viscosity of the mantle there will never be equilibrium during times of ice sheet changes. In fact, if the ice sheet were to remain fixed at any given configuration, the Earth beneath would continue to deform for thousands to several tens of thousands of years, depending on the mantle viscosity, during which time the stresses would also change. This effect is observed today in the present-day uplift in Fennoscandia, which is continuing long after the end of the glaciation.

Since the realization that Fennoscandia is uplifting because of a previous ice sheet, a large number of GIA models have been developed to explain the phenomenon. An overview of earlier models can be found in Steffen and Wu (2011). Since then, and the publication of L2009, there have been new studies and models of the Fennoscandian surface velocity field, the thickness of the mechanically strong lithosphere and the viscosity of the mantle: Zhao et al. (2012), van der Wal et al. (2013), Schmidt et al. (2014), Steffen et al. (2014), Nordman et al. (2015), Root et al. (2015), Simon et al. (2018), Vestøl et al. (2019) and Kierulf et al. (2021). A new book on Glacially Triggered Faulting (Steffen et al. 2021) which contains extensive information on GIA and glacially triggered, or postglacial, faults has also been published.

2 Numerical modelling of glacial isostatic adjustment

Over the years several approaches for numerical modelling of the Earth's response to glacial load changes at the surface have been developed such as spectral decomposition (e.g. Peltier 1974, Wu and Peltier 1982, Wolf 1991), finite difference - spectral (Martinec 1999), finite volume (Latychev et al. 2005) and finite element (e.g. Gasperini and Sabadini 1990, Wu 1992), as well as mixed methods. In this study we will make use of the Finite Element (FE) methodology following the same approach as used in L2009. Here we will only give a brief summary of the methodology while L2009 should be consulted for further details and discussion on simplifying assumptions.

2.1 Modelling methodology used in this study

We solve the linearized equation of motion for the glacial isostatic adjustment (GIA) problem which can be expressed as:

$$\nabla \cdot \sigma - \nabla(\mathbf{u} \cdot \rho_0 g_0 \hat{\mathbf{r}}) - \rho_1 g_0 \hat{\mathbf{r}} - \rho_0 \nabla \Phi_1 = 0 \quad (1)$$

$$\nabla^2 \Phi_1 = 4\pi G \rho_1 \quad (2)$$

$$\rho_1 = -\rho_0 \nabla \cdot \mathbf{u} - \mathbf{u} \nabla \cdot \rho_0 \quad (3)$$

where σ is the stress tensor induced by the GIA process (i.e. not including lithostatic, tectonic or other stress contributions), $\mathbf{u}$ the displacement vector, $\hat{\mathbf{r}}$ a unit vector in the radial direction, ρ the density and g, Φ and G the gravitational acceleration, potential and constant, respectively. Subscripts 0 and 1 refer to the initial and perturbed states respectively (e.g. Wu and Peltier 1982, Wolf 1991, Wu 2004).

Assuming an incompressible Earth and neglecting self-gravitation (fourth term in Equation 1) equations 1-3 reduces to a single equation (Wu 2004):

$$\nabla \cdot \sigma - \nabla(\mathbf{u} \cdot \rho g \hat{\mathbf{r}}) = 0 \quad (4)$$

Although we assume an incompressible earth in the mathematical description of the problem, we allow for compressibility in the elastic description of the material. The first term in equation 4 is the divergence of stress and the second term the pre-stress advection. We solve Equation 4 using the commercial finite element (FE) software ABAQUS (Abaqus 2007) with the second term accounted for by boundary conditions implemented as spring elements (Schmidt et al. 2012).

As our region of interest is confined to Fennoscandia, the lateral scale allows for modelling of the Earth as a flat Earth. The effect of this on the model predictions has been shown to be partly compensated by neglecting self-gravitation (Amelung and Wolf 1994, Schotman et al. 2008). The implementation has shown to generate vertical displacements and displacement rates in good agreement with models solving the full set of equations on a spherical earth (Spada et al. 2011).

Each simulation is split into two model runs, one regional model and one local sub-model. The regional model covers the entire ice sheet over Fennoscandia (Figure 3-1) with a FE-mesh of approximately 50 × 50 km lateral resolution and vertical resolution increasing from 5 km at shallowest depth to approximately 330 km at the core-mantle boundary. To minimize boundary effects the model is embedded in a half-sphere of radius about 22 times the ice sheet dimension (Lund 2005). The sub-model uses a finer mesh (approximately 10 × 10 km lateral resolution and 1 km vertical resolution) in a 450 × 450 km region centred at Forsmark, Sweden, and extending down to a depth of 30 km. The sub-model is fully confined to the elastic lithosphere and therefore purely elastic. In order to have manageable model sizes and computation times, the regional model is run using linear elements with reduced integration and hourglass stabilization.

The sub-models, however, are run using full integration as otherwise the stress solution close to the model boundaries displays clear fluctuations. For each GIA model, a regional flat earth model is first run, loaded by the ice-sheet reconstruction/projection. Displacements are then extracted from the regional model over the surfaces of the local sub-model. Finally, the local sub-model is driven by applying the temporal evolution of the displacements in the regional models to all six bounding outer surfaces of the local sub-model. The sub-model therefore does not contribute with any information to the solution not already present in the regional model but rather acts as an elaborate way of interpolating the solution in the regional model onto a finer mesh based on the FE framework.

2.2 Recent developments

Since the publication of L2009, two new FE methods using commercial FE-software for modelling the GIA phenomenon have been published, Wong and Wu (2019) and Hampel et al. (2019). The work by Wong and Wu (2019) extends the findings by Bängtsson and Lund (2008) that the technique presented in Wu (2004) cannot be fully generalized to a compressible earth. In order to properly implement compressibility, and thus be able to account for all four terms in Equation 1, Wong and Wu (2019) suggests an iterative scheme. Initially the equation:

$$\nabla \cdot \sigma = 0 \tag{5}$$

is solved subject to the appropriate boundary conditions and surface load and the resulting displacement vector is extracted. Using the solution to Equation 5, Equations 2 and 3 can be solved and numerical values of terms 2-4 in Equation 1 can be computed as volumetric averages over each element. These are then implemented as body forces acting on the individual elements after which Equation 5 is solved again. The scheme is repeated until the solution for the displacement vector converges. In the next time step the converged displacement vector from the previous time step is used as an initial value in computing the body forces on each element after which Equations 5, 3, and 2 are iterated until convergence. The feasibility of this approach was, however, only demonstrated for axi-symmetric (essentially 2D) GIA problems. An extension of his methodology was presented in Huang et al. (2023), allowing for the solution of fully 3D GIA problems.

Hampel et al. (2019) use the commercial finite-element software Abaqus and the keyword NLGEOM, which performs the simulations with a geometrically non-linear formulation, a “large displacements” approach. This methodology produces the correct stresses directly in the model, without the need for post-processing of the stress result, something which allows direct calculations of e.g. fault motion. Using the NLGEOM keyword instead of elastic foundations or springs, Hampel et al. (2019) finds that the resulting surface displacement field is in agreement with the foundations approach by Wu (1992), when used with the same incompressible models. They do not show results for the stress field, or for GIA models with compressibility. Instead they use models of floating columns and find that the NLGEOM simulations predict the results for compressible columns better than the elastic foundation simulations. There is ongoing discussion in the community about the applicability of the NLGEOM approach to large scale GIA models. The methodology was benchmarked in Reusen at al. (2023) to approaches using both spectral methods as well as the FE methodology with emphasis on the horizontal displacements. The study concluded that for smaller ice-loads (up to approximately 200 km radius) the methodology yielded acceptable results.

Recently the elastic springs approach to GIA modelling in commercial finite-element packages (Schmidt et al. 2012) has also been used with the COMSOL software (Comsol 2021), with results equal to those obtained with Abaqus (Vachon et al. 2022).

3 Ice sheet models

The main purpose of this study is an analysis of the effects of various potential future ice sheet evolutions on the crustal stress field at Forsmark. We use five different ice sheet models: a Saalian type ice sheet (NH40 - Colleoni and Liakka 2020), a reconstruction of the Weichselian glaciation (UMISM - SKB 2010) which was also used in L2009, and three future projections based initially on future climate projections (RCP45, RCP45e, RCP85 - Thölix et al. 2019). The volume and areal extent of the ice sheets varies significantly, with NH40 being the largest and RCP85 the smallest, covering a wide range of possible future glacial scenarios. None of these ice sheets were developed jointly with any of the earth models we will use, described in section 4, implying that the ice-earth model combinations are not self-consistent in a GIA sense. We will briefly review the ice models below, and discuss features of importance to this study. For more in-depth information the reader is referred to the cited original sources.

The UMISM ice sheet reconstruction is a regional model including only the region of the Weichselian ice sheet. All other ice sheet models include ice in the entire northern hemisphere. A region as large as the entire northern hemisphere is not compatible with the flat-Earth approximation used for the FE model in this study. In addition, as the main target of this study is a rather restricted area close to the centre of the Fennoscandian ice sheet, the ice load at great distance from Forsmark (outside Fennoscandia) will not be of importance to our results (see e.g. section 3.1). We therefore only consider the ice sheet covering Fennoscandia and surrounding areas in our GIA models. For the RCPxx models, the ice in this area is clearly delimited from the other northern hemisphere ice sheets and occupy the same region as that covered by the UMISM reconstruction. For the NH40 ice model we have to make special arrangements, see below.

In this study, we define the Glacial Maximum, GM, as the time when the ice has its greatest volume, with the exception of the NH40 Saalian type ice sheet reconstruction. In NH40, the time of greatest thickness (within the region we use) has been used as GM, as this only differs by 500 years from the time of greatest volume and additionally coincides with the time of greatest thickness at Forsmark. The RCP45 model has two pulses of ice growth of similar size, where the earlier is slightly larger but the later correlates better in terms of model time with the GM of the other ice sheets, hence we refer to the peak volume of the later pulse.

The End Of Glaciation, EOG, is not well defined for all ice models as many are not fully ice-free at the last time-step in the models. In these, we select as EOG a point in time at which the decrease in volume and glacier extent appears to level out. This is defined slightly ad hoc, but is suitable for the purpose of this study. The GM and EOG times used for the different ice models in this study are listed in Table 3-1 in terms of thousands of years (kyr) since the start of the ice sheet model simulation, a measure we will refer to as model years.

3.1 NH40 – a Saalian type ice sheet

The Saale ice sheet was significantly larger than the Weichselian ice sheet. In order to investigate the induced stress effects of a very large ice sheet, both spatially and in thickness, we use the simulation of a Saalian type ice sheet by Colleoni and Liakka (2020), hereafter referred to as NH40. The ice sheet simulation starts at 245 kyr before present (BP) and runs for 130 kyr until 115 kyr BP at a resolution of 500 years and approximately 40 × 40 km. We add another 45 kyr to the time history to reach the time when the Weichselian ice sheets starts to grow significantly, with the ice load assumed constant from 115–70 kyr BP. During this time there is ice only on the islands in the Barents Sea and north of the Russian north coast. Due to significant timing uncertainties in the climate data used for the NH40 simulation, the time of 0 BP is not well defined. For the remainder of this report, where relevant, we will however assume 0 BP to equal the year 1950.

At glacial maximum, 131 kyr BP, NH40 is more or less continuous from the British Isles through Scandinavia, Siberia, across Bering's Strait, over northern North America and Greenland (Figure 3-1). This is considerably larger than the region covered by any of the other ice sheets used in this work. We therefore increased the model domain for the GIA models where the NH40 was used, see Figure 3-1 , using a 50 × 50 km resolution (similar to the resolutions of the mesh used in the other GIA models) and an azimuthal projection such that nodes in Scandinavia in the two meshes are within 2-3 km or less.

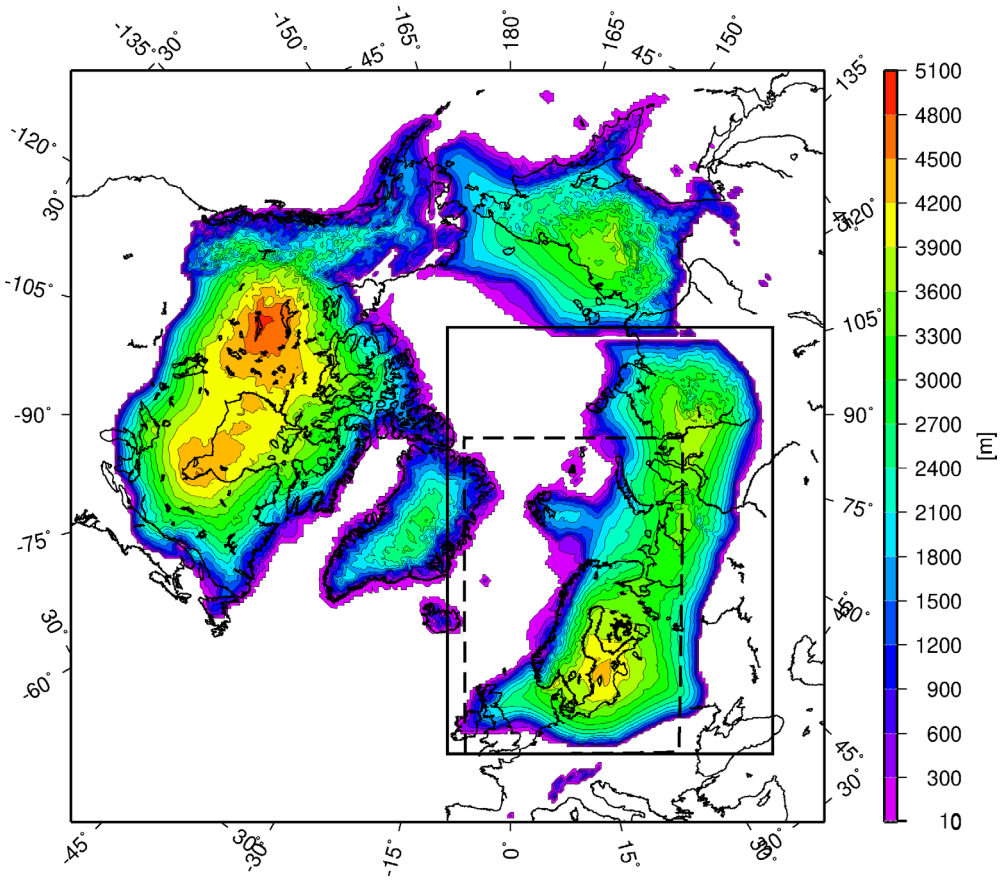

Figure 3-1. *Thickness of the NH40 Saalian type ice sheet at glacial maximum, 131 kyr BP. The solid box shows the area used for the regional NH40 GIA model. For comparison, the dashed box shows the area used for the regional models loaded by the UMISM and RCPxx ice sheets. Ice in Greenland, Iceland and Jan Mayen included in the boxes was not used in this work.*

Transfer of the NH40 onto the GIA mesh was performed using the tools *surface* (with tension factor 0.35) and *grdtrack* (using bi-cubic interpolation) of the Generic Mapping Tools V5.4 (Wessel et al. 2019). The areal extent, ice-volume and maximum thickness of the ice sheet before and after the transformation differ by less than a few percent.

Comparison of the shallow subsurface stress predicted at Forsmark using NH40 transferred onto either the smaller GIA mesh used for the other ice sheets or the larger NH40 mesh show less than a few percent difference at all times. Increasing the region covered by the NH40 FE mesh further is therefore expected to have little impact on the predicted stresses at Forsmark. Snapshots of the ice sheet at select times can be seen in the upper row of Figure 3-2 and the temporal evolution of the areal extent, volume, maximum thickness as well as thickness at/distance to Forsmark can be seen in Figure 3-3. Despite NH40 being the overall largest ice sheet of five studied here, the duration of ice coverage at Forsmark is exceeded by two of the other models (UMISM and RCP45). In NH40 Forsmark is covered by ice in two periods of 7.5 kyr and 10.5 kyr, separated by 11 kyr during which the ice margin is located 50-100 km north of Forsmark. NH40 displays the greatest ice thickness at Forsmark among all studied ice sheets, reaching 4031 m at GM. The load centre of the ice sheet (as well as maximum thickness) varies with time (Figure 3-2) but is at GM located furthest south among the ice sheets used herein.

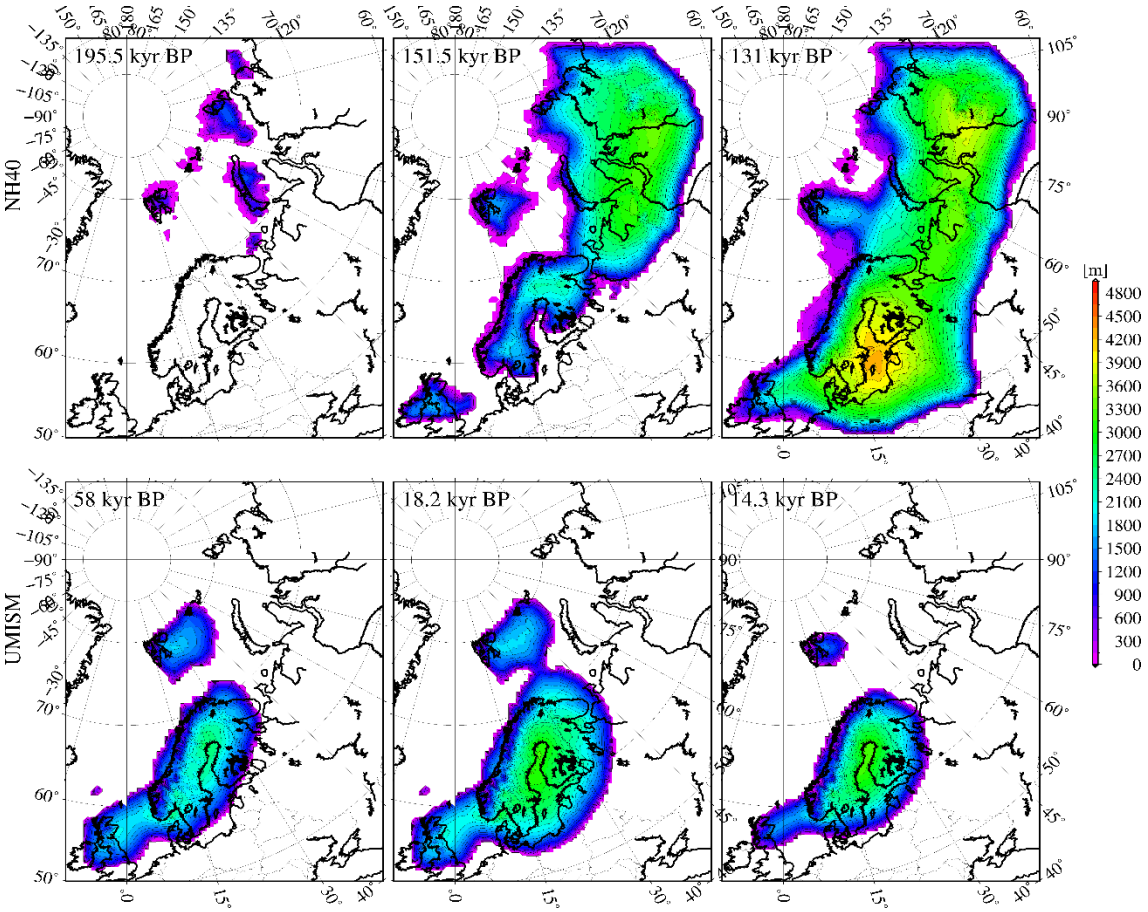

Figure 3-2. *Maps of the thickness of the NH40 Saalian type ice sheet (upper row) and the UMISM reconstruction of the Weichselian ice sheet (lower row) at selected points in time (also indicated in Figure 3-3). Note that the NH40 ice sheet has been limited to the region indicated by the solid box in Figure 3-1. Maximum extent of the NH40 ice is at 131 kyr BP and of the UMISM ice at 18.2 kyr BP.*

3.2 UMISM – a Weichselian ice reconstruction

The University of Main Ice-Sheet Model, UMISM (SKB 2010), is a numerical model used to reconstruct the Weichselian ice sheet. This reconstruction was used in L2009 and is included here both as a reference and as a scenario for a future Weichselian type ice sheet. The UMISM reconstruction starts at 120 kyr BP and runs up until year 0 BP, equivalent to year 1950 (note that in L2009 only the later stages of the reconstruction, from 68 kyr BP onward, were used). The UMISM model has a spatial resolution of approximately 50 × 50 km and a temporal resolution of 1000 years until 20 kyr BP when the resolution increases to 100 years. The area covered is indicated in Figure 3-1 and illustrations of the ice sheet at various points in time are given in Figure 3-2 and Figure 3-6.

The evolution of the ice sheet is characterized by two major advances with the latter being the largest. Maximum areal extent and volume are reached at the Last Glacial Maximum, LGM, at 18.2 kyr BP. The temporal evolution of the areal extent, volume, maximum thickness as well as thickness at/distance to Forsmark can be seen in Figure 3-3 and Figure 3-4 together with the temporal evolution of the other ice sheets. In comparison to the part of NH40 used in this work, the maximum areal extent and volume of the UMISM reconstruction is only about 41 % and 30 % of that of NH40. Forsmark is covered by ice during both the major advancements in the UMISM reconstruction with the ice thickness reaching a maximum of 2937 m 800 years after LGM. In contrast to the NH40 model, the load centre and maximum thickness in the UMISM is relatively stable over the central Bay of Bothnia throughout the reconstruction (Figure 3-2).

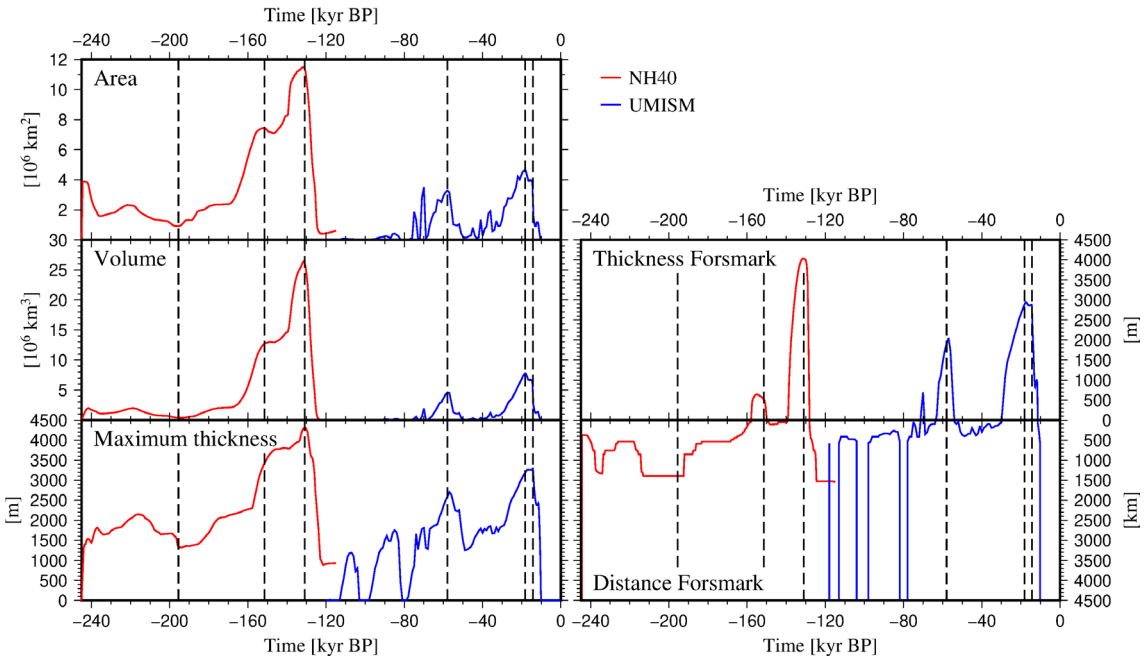

Figure 3-3. *Temporal evolution of the NH40 Saalian type (red; limited to the solid box in Figure 3-1) and the UMISM Weichselian (blue) ice sheets. Left: areal extent, volume and maximum ice thickness. Right: ice thickness at, and closest distance to the ice margin from, Forsmark. Dashed lines indicate times at which maps of the ice sheets are shown in Figure 3-2. Peak values are summarized in Table 3-1.*

Worth noting in the UMISM reconstruction is that while LGM occurs at 18.2 kyr BP, the maximum thickness occurs at 14.3 kyr BP (Figure 3-2 and Figure 3-3, Table 3-1) and the ice sheet remains thick over Forsmark until this time. As a consequence, surface displacements and stress build-up in the crust beneath Forsmark, due to the load of the UMISM ice sheet, are expected to continue to increase for several thousands of years after LGM. No transfer of the UMISM model onto the FE mesh was required as the two meshes are identical.

3.3 RCPxx – projections of future ice sheets

In order to study potential future ice sheet scenarios, we use three ice models developed as climate models by Thölix et al. (2019). These are based on a three-pronged approach for CO_2-levels, first using Representative Concentration Pathways (RCP) developed for the Coupled Model Inter-comparison Project 5 (CMIP5) of the IPCC Fifth Assessment Report (IPCC 2013) up until the year 2300, then a subsequent model of CO_2 declines down to 280 ppm, and finally a regression equation, calculating CO_2 from sea surface temperatures. The three models are:

- RCP45: Approximate total radiative forcing of 4.5 W/m^2 in or shortly after 2010 with respect to pre-industrial time, followed by a fast CO_2 decline from year 2300 onward.
- RCP45e: Same as RCP45 until year 2300 followed by a slow CO_2 decline.
- RCP85: Approximate total radiative forcing of 8.5 W/m^2 in or shortly after 2010 with respect to pre-industrial time, followed by a slow CO_2 decline from year 2300 and on.

Under these emission scenarios, virtually all contemporary studies indicate that the onset of the next glaciation in the Northern Hemisphere will be significantly delayed – occurring at least 100 kyr from now under RCP4.5 and several hundred thousand years under RCP8.5 (SKB 2023, Section 3.4.5 and references therein). However, in contrast to these studies, Thölix et al. (2019) project that glaciation in the Northern Hemisphere, including Fennoscandia, will occur much sooner. This discrepancy arises because the simulations in Thölix et al. (2019) are excessively cold, producing significantly more ice over Fennoscandia in the present day than is actually observed. This cold bias then carries over into their future projections, resulting in Fennoscandian glaciations at times when they are not expected based on the broader scientific literature.

In summary, the timing of ice coverage projected by Thölix et al. (2019) is not considered realistic and does not align with conclusions from other SKB reports (e.g. SKB 2023). However, for the purpose of this study, i.e. to examine how different ice models influence the evolution of stress fields induced in the crust, the exact timing of glaciations is not critical. Therefore, despite their unrealistic timing, the ice configurations simulated by Thölix et al. (2019) are still used in this analysis.

The RCPxx projections cover 120 kyr starting from year 2010 with a temporal resolution of 100 yrs for the first 10 kyr and 1 kyr thereafter and a spatial resolution of 0.75° in latitude × 0.5° in longitude. However, since there is initially none-zero ice thickness over Svalbard and the Scandes, our GIA models loaded by the RCPxx projections start with ice-free conditions at the year 1010 and ramp up the ice linearly to the 2010 starting ice thicknesses. This has little impact on the features of interest in this study, such as maximum induced stress, fore-bulge stress and fault stability, but results in erroneously predicted uplift velocities at Forsmark at present. Since these ice models have significantly more ice in the Scandes mountains at year zero than what is actually present there today, Forsmark is located in the model fore-bulge at year 2010. The GIA models loaded by the RCPxx projections have been run for 201 kyr, assuming a constant ice-load for the last 80 kyr of the simulation (i.e. using the load at the last time step of the particular ice model). The RCPxx ice sheet models were transferred onto the FE mesh using the methodology described above for the NH40 ice sheet model. The areal extent, ice-volume and maximum thickness of the ice sheets before and after the transformation differ by less than a few percent.

Evolutions of the RCPxx projections of future Fennoscandian ice sheets are shown in Figure 3-4 with peak values summarized in Table 3-1. Maps of the ice sheets at selected points in time can be seen in Figure 3-5 and Figure 3-6. For comparison, the UMISM reconstruction of the Weichselian ice sheet is included in Figure 3-4 and Figure 3-6. Interestingly, the general temporal trends in terms of areal extent and volume are very similar between the RCPxx ice sheet models and the UMISM, see Figure 3-4. All models have two pronounced periods of glacier advance, separated in time by about 42 kyr, and almost ice-free conditions in-between. The main difference between them is that the UMISM ice sheet grows almost twice as large during the second advance as it was during the first peak, while the RCP45 and RCP45e ice sheets have approximately the same sizes during the two main advances. In terms of areal coverage, the RCP45 ice grows larger than the UMISM during both periods of glacier advance, while in terms of volume the UMISM ice sheet grows larger than the RCP45 during the last advance. The duration of the glaciated periods is longer in the RCP45 projection than in the UMISM reconstruction and the evolution of the maximum thickness, as well as the thickness at Forsmark, indicates that the RCP45 ice sheet advances rapidly at the onset of each glacial period, then slowly advances to the peak after which it rapidly retreats. This is in contrast to the UMISM reconstruction which seem more dynamic in nature with a rapid advance followed more or less immediately by an even faster retreat.

In the RCP45 projection, Forsmark is covered by ice in two periods spanning 28 and 32 kyr, respectively, with the thickness reaching a maximums of 2047 m and 2006 m (cf. 4031 m in the NH40 simulation and 2937 m in the UMISM, see Table 3-1). Among the ice models used herein the RCP45 projection displays by far the longest period of ice coverage over Forsmark. In the RCP45e projection the ice margin barely reaches Forsmark at the glacial maximum (Figure 3-4 and Table 3-1) while in the RCP85 projection Forsmark is ice-free during the entire simulation, with the ice margin located no closer than about 180 km north of the site.

The load centre and maximum thickness in the RCPxx projections is located further north than in the UMISM and NH40. Taken together, the NH40 simulation, the RCPxx projections and the UMISM reconstruction cover a wide range of ice sheet scenarios at Forsmark, ranging from extended periods of ice cover to ice free conditions with Forsmark located in the fore-bulge. These simulations also include models where the ice sheet centre is located at either higher or lower latitudes.

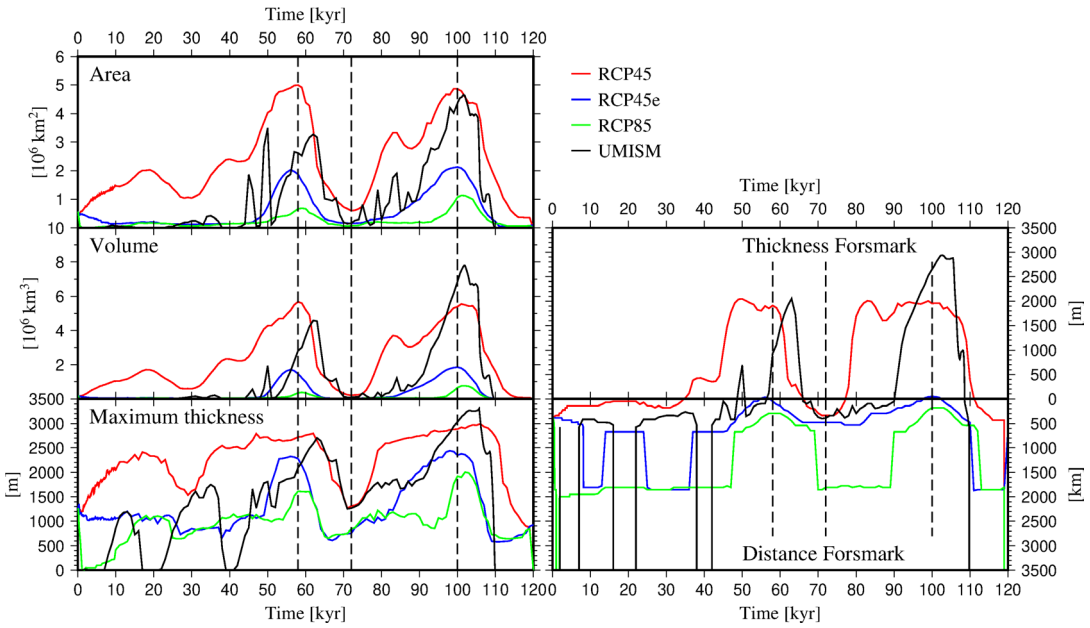

Figure 3-4. *Temporal evolution of the RCP based Fennoscandian ice sheet models and the UMISM Weichselian ice sheet reconstruction. Left: areal extent, volume and maximum thickness of the ice sheets. Right: ice thickness at, and closest distance to the ice margin from, Forsmark. Dashed lines indicate times at which maps of the RCPxx and the UMISM ice sheets are shown in Figure 3-5 and Figure 3-6. The time in the RCP projections as well as the UMISM reconstruction is in model years.*

Table 3-1. Summary of maximum area, volume, regional ice thickness and ice thickness at Forsmark and End Of Glaciation, EOG, as seen in Figure 3-3 and Figure 3-4 for all ice sheet models. In all the RCPxx models as well as in the UMISM, two major advances of the ice sheet are present. For all except RCP45, the maximum area, thickness, volume and thickness at Forsmark are reached in the later advancement while in RCP45 the two advances are of similar size. Therefore, RCP45 peak values are given for both ice sheet maxima. Times are given in terms of kyr since the start of ice sheet models and times in bold font mark the Glacial Maximum, GM, as defined and used herein.

Ice sheet	Max area		Max volume		Max thickness				Max thickness Forsmark		EOG
	[10^6 km^2]	[kyr]	[10^6 km^3]	[kyr]	[m]	[kyr]	Lat.	Lon.	[m]	[kyr]	[kyr]
RCP45	5.01	57	5.68	58	2796	62	67.32	22.79	2047	50	-
	4.88	99	5.55	**101**	2993	106	67.32	22.79	2006	99	116
RCP45e	2.13	100	1.86	**100**	2440	99	67.32	22.79	49	100	111
RCP85	1.13	101	0.77	**102**	2008	102	68.07	21.10	-	-	113
NH40	11.50	113.5	26.39	113.5	4313	**114**	58.02	17.64	4031	114	123
UMISM	4.66	101.6	7.80	**101.8**	3305	105.7	64.47	22.29	2937	102.6	109.9

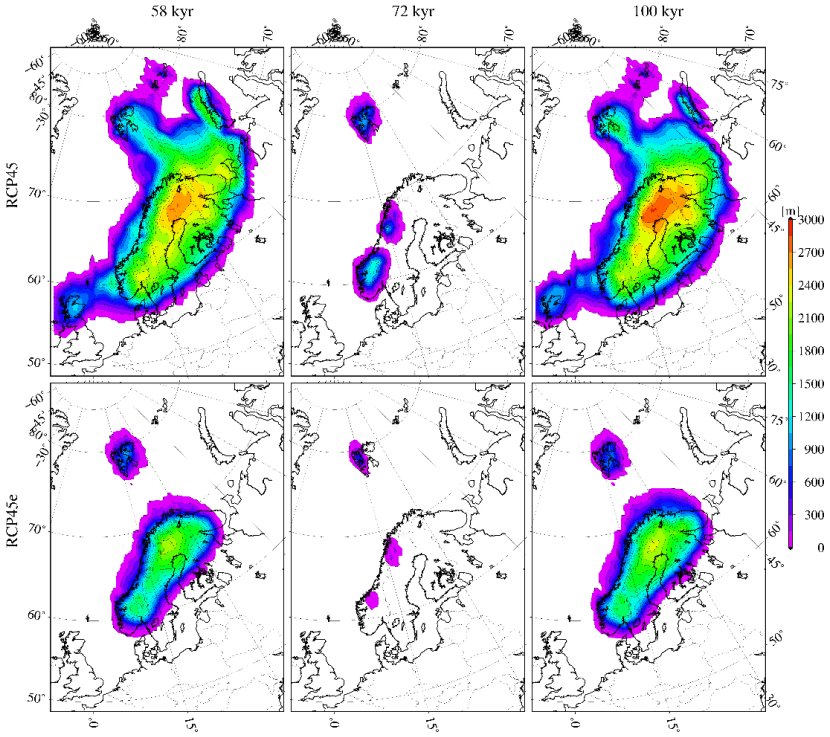

Figure 3-5. *Maps of the thickness of the RCP45 and RCP45e ice sheets at selected points in time, as indicated in Figure 3-4. At the times in the first and last map in each row the ice sheets are close to their maximum areal extents. Time is given in years since start of the ice sheet models.*

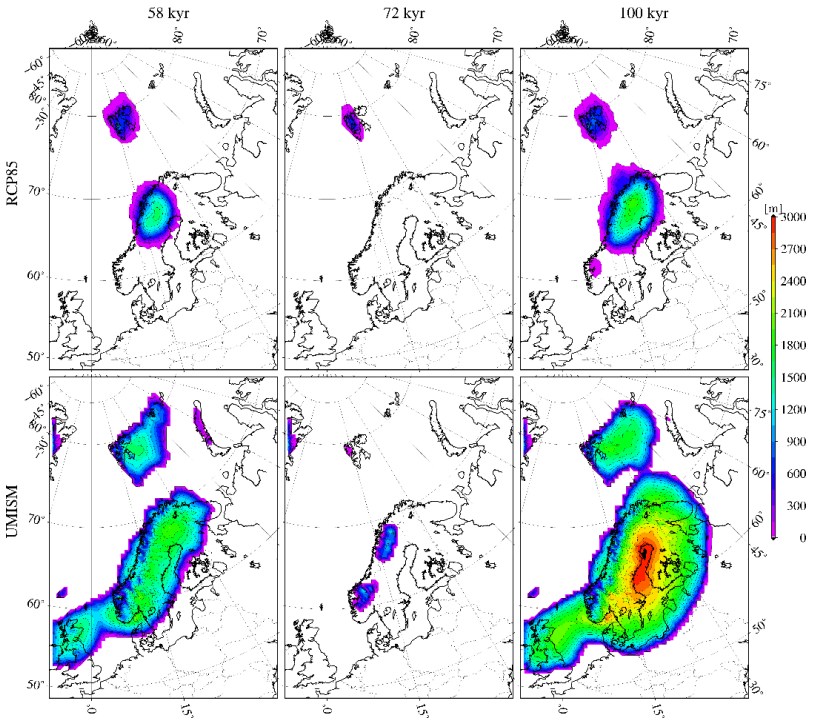

Figure 3-6. *Maps of the thickness of the RCP85 and UMISM ice sheets at selected points in time as indicated in Figure 3-4. At the times in the first and last map in each row the ice sheets are close to their maximum areal extents. Time is given in years since start of ice sheet models. For the UMISM reconstruction (lower row) the slices from left to right are equivalent in time to 62, 48, and 20 kyr BP.*

3.4 Extended residence time of the ice configuration at glacial maximum

In order to study the effect of extended residence time of the GM ice configuration we prepare two additional scenarios of the UMISM, NH40, and RCP45e models. In these we maintain the GM ice sheet configuration for periods of 25 kyr and 50 kyr, respectively, before proceeding with the deglaciation phase in the simulations. 50 kyr is similar to the projected maximum time an ice sheet could be situated over Forsmark during future glaciations (Liakka et al. 2024). This allows the earth to adjust to the GM ice load for longer time periods and allows us to study how close to isostatic equilibrium the models develop.

3.5 Repeated glaciations

The current ice age, the Quaternary, started 2.58 million years ago. Since then, the ice sheets in the northern and southern hemispheres have been advancing and retreating in so called glacial periods. During the last 800 kyr the average duration of a full glacial and interglacial period has been of the order of 100 kyr, with interglacial periods typically 10-30 kyr long (Past Interglacial Working Group of PAGES 2016). We have seen that a dynamically evolving ice sheet prevents the Earth under the load to reach isostatic equilibrium and that reaching such an equilibrium may take several tens of thousands of years after the ice disappears or stops evolving. A relevant question is therefore how large the effect of previous ice sheets on the GIA response of a following ice sheet is?

To study the impact of repeated glaciations a special version of the RCP45 ice sheet, RCP45x, has been prepared where we remove all ice during the first 70 kyr of the model. This is the time period of the first phase of advance and retreat of the RCP45 ice sheet, see Figure 3-4. Although the RCP45 model is not fully ice-free at 70 kyr, between 67 and 77 kyr the ice is confined to the Scandes and Svalbard with relatively small changes to the ice-sheet volume compared to the periods just before and just after. After the first ice free 70 kyr, the RCP45x model is ramped up linearly to the minimum ice configuration at 73 kyr in the original RCP45 model.

The original RCP45 model will serve as an example of repeated glacials separated by a 10 kyr interglacial, while RCP45x will serve as a model of only the second glacial. Hence the difference between the RCP45 and RCP45x models will measure the effect of the first glacial on the second. The duration of the interglacial here is in the lower end of estimated interglacial durations during the last 800 kyr (Past Interglacial Working Group of PAGES 2016). Further it has been estimated the current Holocene interglacial will last at least another 100 kyr from present day (e.g. Liakka et al. 2024). For a longer interglacial period than that considered here, the effect of the previous glacial will have relaxed further. Thus, the impact of repeated glaciations studied in this work should be considered upper estimates.

4 Earth models

The selection of earth models used in this study is based on the results in Lund and Schmidt (2011) and in Schmidt et al. (2014), where the predicted present-day uplift velocities in response to the UMISM model were compared to the uplift in Fennoscandia observed using cGPS (Lidberg et al. 2007, 2010). Based on the overall fit as well as the fit at Forsmark to the current uplift, the models M14, M118 and L11 have been selected for this work. The M14 and M118 models have a laterally uniform thickness of all material layers, while the L11 model has a laterally varying elastic thickness of the lithosphere (see Figure 4-1) based on truncated and scaled elastic thickness estimates from gravity data and Bouguer coherence modelling over northern Europe (Pérez-Gussinyé et al. 2004, Pérez-Gussinyé and Watts 2005) and seismic data over Greenland and northern Russia (Priestly and McKenzie 2006, Artemieva and Thybo 2008).

In addition to the M14, M118, and L11 models, two earth models inferred from global GIA studies of the last glacial period have been used. The VM5a model by Argus et al. (2014) and the model by Lambeck et al. (2017), here referred to as L2017. The rheological structure of the models is presented in Table 4-1. Elastic properties and densities in all models are volume averages taken from the Preliminary Reference Earth Model (Dziewonski and Andersson 1981, Table 4-2). Predicted present day uplift velocities and remaining land uplift at Forsmark for all five earth models loaded by the UMISM ice sheet are presented in Table 4-3.

As Table 4-1 and Table 4-2 show, models M14, M118, VM5a and L2017 have laterally uniform thicknesses of all material layers. M14 and M118 have a 120 km thick fully elastic lithosphere layer, L2017 has a slightly thinner fully elastic layer of 102 km whereas VM5a has a 60 km thick fully elastic layer and then a 40 km thick layer with viscosity 10^{23} Pa s, which will act very similar to a fully elastic layer on the time scales of the ice histories herein, 120–200 kyr. Models VM5a and L2017 thus have almost identically thick elastic lithospheres which are 20 km thinner than the M14 and M118 models. The two former will therefore have slightly lower flexural rigidity than the two latter, and allow for more short wavelength displacements.

The L11 earth model comes in two versions, one larger used with the Saalian ice sheet reconstruction, NH40, and one smaller used with the other ice sheets. The original data have been truncated and scaled to yield minimum and maximum elastic thicknesses of 60 km and 288 km in both L11 models and mean thicknesses of 120 and 139 km in the smaller and larger L11 model respectively. In both models the elastic thickness beneath Forsmark is 130 km with thickening to the east and thinning to the west. Test simulations with the UMISM ice sheet on the two L11 earth models yield negligible differences in the surface displacement and stress tensor at Forsmark.

Table 4-1 shows that the viscosities in the upper mantle, beneath the lithosphere, are very similar in all earth models considered. There is only a factor of three difference between the lowest, models M14 and VM5a, and the highest, model L11, while in the lower mantle the viscosity differences span more than an order of magnitude. The earth models used herein represent optimal models to three different reconstructions of the Weichselian ice sheet that differ in spatial and temporal evolution. This therefore indicates that the viscosity in the lower mantle has a limited effect on the resulting present-day surface velocities (available observations are in terms of velocities, not displacements) in Fennoscandia, in agreement with most previous studies. In this study we have not considered laterally varying viscosities.

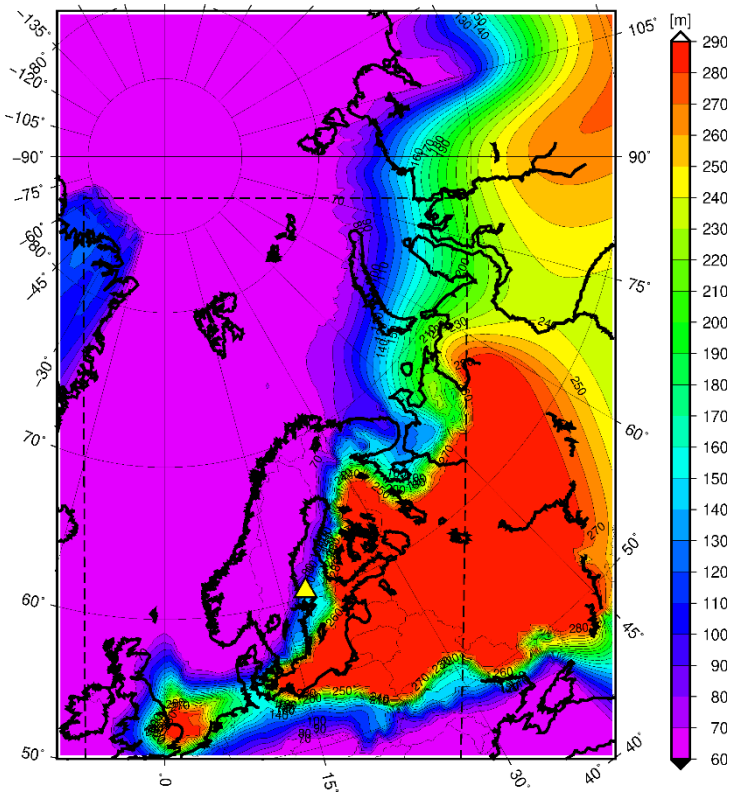

Figure 4-1. *Elastic thickness of the lithosphere used in the L11 model. The smaller dashed rectangle shows the region used for all ice sheets except the NH40 which used the full model. Variation of elastic thickness outside the region used varies according to closest boundary of region. Yellow triangle marks location of Forsmark.*

Table 4-1. Rheologic structure of earth models used in this study. For the upper and lower mantle, the table contains the depth interval and the viscosity. CMB is the Core Mantle Boundary

Model	Lithosphere [km, rheology]	Upper mantle [km, Pa s]	Lower mantle [km, Pa s]
M14	120, elastic	120–670, 5×10^{20}	670–CMB, 30×10^{20}
M118	120, elastic	120–670, 10×10^{20}	670–CMB, 300×10^{20}
VM5a	60, elastic 60–100, viscoelastic 10^{23} Pa s	100–670, 5×10^{20}	670–1250, 15.8×10^{20} 1250–CMB, 31.6×10^{20}
L2017	102, elastic	102–670, 5.1×10^{20}	670–CMB, 130×10^{20}
L11 small	60–288 (mean 120; 130 at Forsmark), elastic	Lithosphere–CMB, 15×10^{20}	
L11 large	60–288 (mean 139; 130 at Forsmark), elastic		

Table 4-2. Elastic parameters and densities used in the earth models, based on volume averages of PREM (Dziewonski and Andersson 1981). LAB – Lithosphere Asthenosphere Boundary with depth given in Table 4-1. CMB – Core Mantle Boundary. * 60 km in VM5a

Layer depth extent [km]	0–15	15–50*	50*–LAB	LAB–410	410–670	670–CMB
Young's modulus [GPa]	64	156	170	182	263	552
Poisson's ratio	0.28			0.30		
Density [kg/m3]	2750	3251	3378	3433	3837	4853

Table 4-3. Present day uplift rate and remaining land uplift at Forsmark predicted by the five earth models loaded by the UMISM reconstruction of the Weichselian ice sheet (SKB 2010). For comparison, the uplift rates observed by GNSS in three studies at station MAR6, located in Gävle approximately 65 km east-north-east of Forsmark, are included under "Data". The difference in the three studies mainly reflects differences in the reference system used when processing the GNSS data. Estimate of the remaining uplift is not available, n/a, in these studies

Model	**Uplift rate [mm/yr]**	**Remaining uplift [m]**
M14	6.9	44
M118	8.0	132
L11	6.6	52
VM5a	5.4	29
L2017	9.4	89
Data		
Lidberg et al. (2007)	7.3	n/a
Lidberg et al. (2010)	8.9	n/a
Kierulf et al. (2021)	7.7	n/a

5 Vertical surface displacements

In this section we study the magnitude and temporal evolution of the vertical displacements at Forsmark induced by the ice sheet scenarios on the different earth models used. We also present the impact of an extended residence time of the ice sheet configuration at GM, as well as that of repeated glaciations, on the vertical displacements.

5.1 Vertical surface displacements at Forsmark

Vertical surface displacements at Forsmark for all earth models loaded by the NH40 and UMISM ice models can be seen in Figure 5-1. Maximum subsidence ranges from 565 - 823 m and 479 - 687 m for NH40 and UMISM, respectively (see Table 5-1). For both ice models the greatest vertical displacement occurs in the VM5a earth model, closely followed by the M14 earth model, while the least subsidence occurs in the M118 earth model. Interestingly, the vertical displacements in the L11 earth model are greater than in the L2017 model when loaded by the NH40 ice history but not when loaded by the UMISM reconstruction. This is likely both because the thickest part of the ice sheet is located south of Forsmark in the NH40 but north of Forsmark in the UMISM (see Table 5-1) and because the thickness of the lithosphere varies laterally in the L11 earth model. It is further noticed that the maximum subsidence is not only regulated by the viscosity of the upper mantle. Both the VM5a and M14 earth models have the same viscosity in the upper mantle but in the uppermost part of the lower mantle the viscosity in the VM5a is about half that of the M14 earth model (Table 4-1). The viscosity in the upper mantle of the L2017 earth model is only slightly higher than that in the VM5a and M14 earth models (5.1×10^{20} Pa s vs. 5.0×10^{20} Pa s) yet the maximum vertical displacement at Forsmark in the L2017 model is 9–19 % less than that in the VM5a and M14 earth models. However, the viscosity of the lower mantle in the L2017 model is a factor ~4.3 greater than that in the VM5a and M14 earth models. Finally, the L11 earth model has the highest upper mantle viscosity of all Earth models herein, yet it does not display the smallest maximum subsidence at Forsmark among the studied earth models. The lower mantle in the L11 earth model is however the weakest among the Earth models, while comparable to that in the shallow lower mantle in the VM5a model, it is a factor 9–20 lower than that in the L2017 and M118 earth models respectively, thereby compensating for the stronger upper mantle in the L11 model. It can therefore be concluded that while the viscosity of the lower mantle has a limited impact on present day uplift rates (post-glacial phase) it does play an important role for the vertical displacements during the inter-glacial phase of the GIA process in Fennoscandia.

Maximum subsidence in the earth models loaded by NH40 and UMISM occurs some 1.5–2 kyr and 3.7 kyr, respectively, after GM (see Table 3-1 and Table 5-1), i.e. during times when the ice sheets have started to retreat. This results from the steady growth of the ice sheets up until the GM and the short residence time of the GM ice configuration prior to deglaciation. The Earth will not have reached isostatic equilibrium at GM, implying that the Earth's surface continues to subside until a balance between the vertical displacement and the contemporary ice load has been achieved. Locally at Forsmark, maximum subsidence occurs at the same model time for all earth models when loaded by the NH40 reconstruction while when loaded by the UMISM reconstruction, peak vertical displacement in the L2017 and M118 earth models occurs 100 years later than in the other models (Table 5-1). This is most likely a result of the higher mean viscosity in the mantle in these two models, causing them to be further from isostatic equilibrium than the other three earth models. For both the ice models and all earth models, uplift at Forsmark above the initial equilibrium line only occurs at early times, prior to any major build-up of ice, reaching at most 3.7 m for the L2017 earth model loaded by the NH40 reconstruction.

Following the maximum subsidence after the GM, the surface at Forsmark rapidly rebounds. In general, we see a clear relation between the maximum vertical displacement and the speed of the rebound process. But as observed for the maximum vertical displacement, the L11 earth model again breaks the clear trend when loaded by the UMISM reconstruction but not the NH40. Potentially this is due to the difference in the size of the NH40 and UMISM ice sheets, where the larger NH40 ice sheet activates deeper parts of the mantle than the smaller UMISM ice sheet, thereby decreasing the impact of the combined effect of a lateral variation of the elastic thickness in the L11 earth model and a load centre located south vs north of Forsmark in the NH40 and UMISM reconstructions respectively. The problem is complex though and a well-founded understanding of the cause and consequence would require a larger set of models than run in this study.

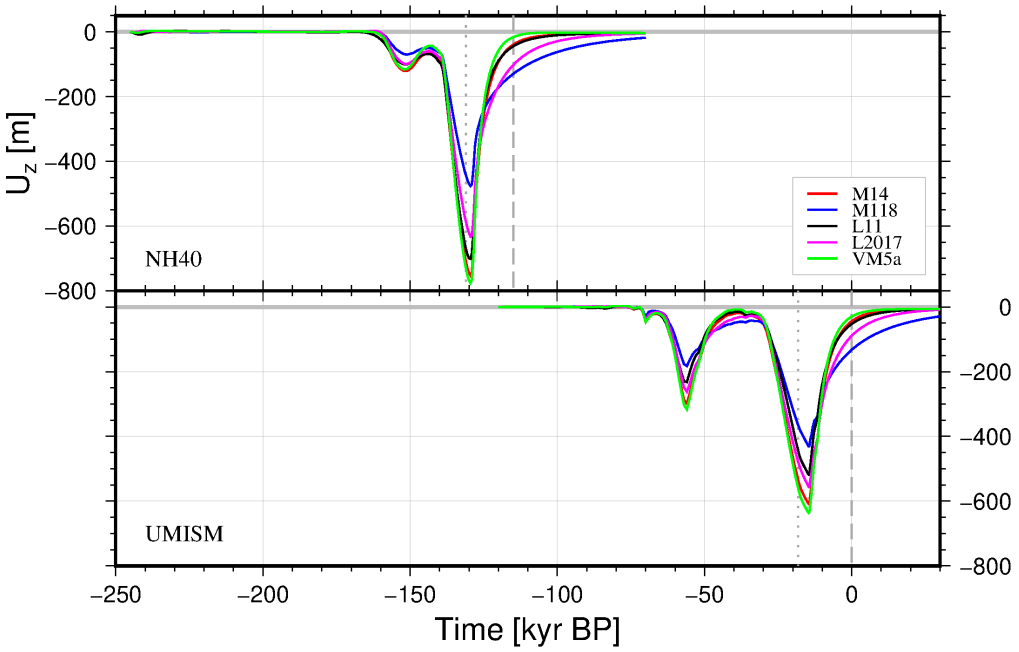

Figure 5-1. *Vertical displacement, Uz, at Forsmark for earth models loaded by the NH40 Saalian type ice sheet simulation in the upper panel and the UMISM reconstruction of the Weichselian ice sheet in the lower panel. Vertical dashed line in upper panel displays the end of the NH40 ice sheet, the later evolution assumes constant load for the remaining time, while for the UMISM ice sheet the same applies from time 0 and onward. Vertical dotted line mark GM defined in Table 3-1.*

Allowing the GIA simulation to continue to run with constant load at the end of the ice sheet simulations we see that for all earth models except the strongest, M118, the remaining vertical displacements are less than a few meters after about 45 kyr. Thus, all these models have come close to isostatic equilibrium. In the M118 earth model the remaining uplift at Forsmark 45 kyr after the end of the ice sheet simulation amounts to 16.6 to 18.1 m for the UMISM and NH40 simulations, respectively, or about 3.8 % of the maximum subsidence.

The RCPxx projections span a large range in terms of size of the ice sheets from the largest, RCP45, which is comparable to the UMISM ice sheet in terms of maximum areal extent (albeit thinner and with longer duration of the glacial pulses, including slower build-up and melting) to the smallest, RCP85, in which the ice margin is never closer than 180 km to Forsmark (Figure 3-4). The vertical displacements induced by RCP45 follow the general trends as was seen for the UMISM and NH40 ice sheets but again the L11 earth model breaks the trend and is the earth model with smallest maximum vertical displacement at Forsmark (Figure 5-2, uppermost panel). Interestingly, this is a local observation as inspecting the maximum vertical displacements over entire Fennoscandia (Table 5-1), the L11 model displays the second greatest subsidence of the Earth models herein. The load centre in the RCP45 projection is located further away from both Forsmark and the eastward thickening of the lithosphere (Figure 3-5 and Figure 4-1) than the UMISM and the NH40 simulations (Figure 3-2).

Forsmark is therefore located further away from the centre of subsidence beneath the RCP45 ice sheet and more affected by the longer wavelength of the surface deformation caused by the thickening of the lithosphere to the east, than is the case when loaded by the UMISM and the NH40 ice sheets. The timing of the maximum subsidence beneath Forsmark when loaded by the RCP45 projection displays a larger spread between the earth models than observed for the UMISM and NH40 reconstructions. The weakest (in terms of low mantle viscosity) earth models, M14 and VM5a, peak at the time of maximum thickness of the ice at Forsmark, which occur 1 kyr prior to the GM (Figure 5-2, Table 3-1 and Table 5-1). The stronger the mantle (higher viscosity) in the earth models, the further delayed in time does the peak subsidence occur, reaching a delay of 4 kyr for the M118 earth model (Table 5-1). The longer period between the GM and maximum subsidence in Forsmark when loaded by the RCP45 projection compared to the UMISM and NH40 can be traced back to the slower thinning of the RCP45 ice sheet following the GM.

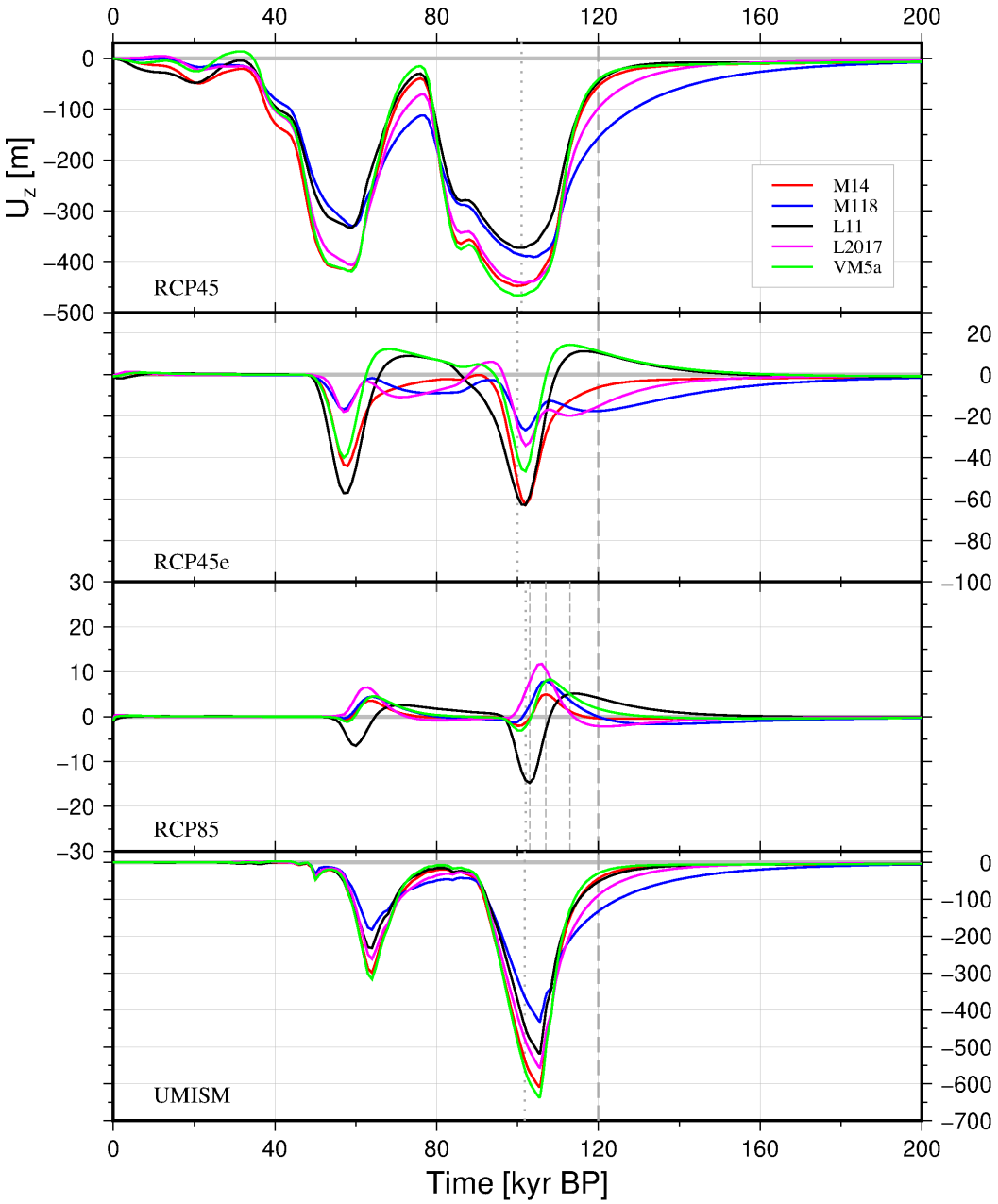

Figure 5-2. *Vertical displacement, Uz, at Forsmark for earth models loaded by the RCP ice sheets: RCP45 (top panel), RCP45e (second), RCP85 (third) and the UMISM ice reconstruction (bottom panel). Time axis is in model years. Thick dashed vertical line running through all panels indicates the last time step of the ice models. For the further 80 kyr of GIA simulations the ice loads have been kept constant. Thin vertical dashed lines in the RCP85 panel display times at which maps of the displacement field in Fennoscandia are shown in Figure 5-3 and Figure 5-4. Dotted vertical line mark GM defined in Table 3-1. Note the different scales on the vertical axes.*

Table 5-1. Maximum subsidence, -Uz, in Fennoscandia and Forsmark and maximum uplift, Uz, at Forsmark. Time is given in terms of kyr since onset of ice sheet model

		Max subsidence Fennoscandia				Max subsidence Forsmark		Max uplift Forsmark	
Ice	Earth	[m]	[kyr]	[Lat]	[Lon]	[m]	[kyr]	[m]	[kyr]
RCP45	VM5a	689	102	66.66	25.11	467	100	13.68	32
	M14	642	104	66.46	26.09	448	100	-	-
	L11	658	104	66.84	24.11	373	101	-	-
	L2017	638	106	66.46	26.09	441	102	4.3	12
	M118	572	106	66.25	24.65	391	104	-	-
RCP45e	VM5a	520	102	67.02	23.09	47	102	14.4	113
	M14	449	102	66.84	24.11	63	102	0.7	5.4
	L11	423	103	67.19	22.06	63	102	11.33	116
	L2017	453	102	66.84	24.11	34	102	6.2	93
	M118	360	103	67.02	23.09	27	102	0.9	6.2
RCP85	VM5a	299	104	67.36	21.01	3	101	8.3	108
	M14	258	104	67.19	22.06	2	100	5.0	107
	L11	204	105	67.36	21.01	15	103	5.2	114
	L2017	260	104	67.19	22.06	2	122	11.7	106
	M118	177	105	67.36	21.01	2	135	7.9	107
NH40	VM5a	823	116	63.90	26.60	776	115.5	3.2	139
	M14	771	116	63.04	23.59	753	115.5	1.7	8
	L11	739	115.5	65.10	23.34	701	115.5	3.1	12
	L2017	667	116	63.46	23.98	632	115.5	3.7	5
	M118	565	116	64.72	25.22	476	115.5	2.2	8
UMISM	VM5a	687	105.5	64.59	22.95	637	105.4	2.7	41
	M14	646	105.5	63.76	22.18	608	105.4	0.3	15
	L11	600	105.5	64.93	21.07	518	105.4	2.0	44
	L2017	600	105.5	64.18	22.56	556	105.5	2.6	38
	M118	479	105.5	64.35	21.64	431	105.5	1.6	38

For the smaller RCP45e and RCP85 ice sheets, the vertical deformation history at Forsmark becomes complex, including both subsidence and uplift, which is due both to the small size of the ice sheets and to the fact that they either only briefly cover Forsmark (RCP45e) or not at all (RCP85). For both ice sheet projections, all earth models predict subsidence at the GM in Forsmark (Figure 5-2) ranging from 1.2 m to 58.9 m for the RCP85 on M118 and RCP45e on L11 combinations, respectively. Following the GM, the fore-bulge migrates inwards towards the load centre turning subsidence into uplift in all earth models loaded by the RCP85 model as well as the earth models VM5a and L11 loaded by the RCP45e model. It is to be noted here that the peak of uplift occurs several kyr after the GM. This is not solely due to the migration of the fore-bulge during glaciation but also due to elastic expansion of the compressible Earth as the surface load decrease. Hence, while a fore-bulge does occur during build-up of the ice-sheets, the peak uplift in the fore-bulge does not occur until the earth decompresses during the removal of the load (see Figure 5-3 and Figure 5-4). The fairly simple relation seen before between the mantle strength and surface deformation, modulated by the lithospheric thickness, no longer dominates. While the maximum subsidence at Forsmark induced by the RCP45e ice sheet on earth models VM5a, L2017 and M118 still follows the trends observed under the load of the more massive ice sheets, the greatest subsidence is seen in the earth models M14 and L11. However, during deglaciation, the fore-bulge migrates in over Forsmark in the L11 model while in the M14 model it does not. Similarly, while the M14 and VM5a differ mainly by the elastic thickness of the lithosphere (120 km in M14 and effectively 100 km in VM5a, Table 4-1) and the viscosity in the upper 580 km of the lower mantle, in the M14 earth model the fore-bulge never reaches Forsmark due to the slightly greater elastic thickness leading to longer wavelengths of the surface deformation.

When loaded by the RCP85 ice sheet all earth models predict subsidence at Forsmark at the GM, as noticed above. However, following the GM, subsidence quickly turns into uplift as the fore-bulge migrates in over Forsmark in all earth models except the L11 (Figure 5-2). In the L11 earth model subsidence instead increases, to peak 3 kyr after the GM (Table 5-1). Rebound then sets in turning subsidence into uplift at 8 kyr after the GM and peaking 14 kyr after the GM. This behaviour significantly deviates from that of the other earth models. It can further be noted that the subsidence following the peak uplift in the L11 model acts on a longer timescale than that displayed by the other earth models. Looking at the vertical displacement field over the full FE-model (Figure 5-3 and Figure 5-4) it is clear that the signal seen at Forsmark is not solely due to the inward migration of the fore-bulge but also a build-up of the fore-bulge over longer time scales in the L11 earth model than in the other earth models tested in this study. The origin of this deviation can probably be related to the fairly small size of the RCP85 ice sheet, mobilizing primarily the upper mantle. The relatively low viscosity of the lower mantle in the L11 earth model cannot compensate for the relatively high viscosity of the upper mantle. Therefore, the L11 earth model is effectively the stiffest earth model seen by the GIA process associated with the RCP85 ice sheet. It is finally worth noting that for the L2017 and M118 earth models the node line (i.e. the separator between subsided region and the fore-bulge) start migration outwards as the rebound continues, turning uplift into subsidence once more at Forsmark after which the region slowly approaches steady state.

The GIA simulation has been run for an additional 80 kyr following the end of the RCP ice sheet simulations, assuming no further changes in the ice sheets. With the exception of the strongest earth model, M118, all earth models are close to isostatic equilibrium at Forsmark 40–50 kyr after the end of the RCP ice sheet models. In the M118 model, similar conditions are not reached until the end of the 80 kyr additional GIA simulation. Similar GIA simulations using the UMISM reconstruction have been run for an additional 80 kyr from the end of the UMISM model. These simulations also show that all earth models except M118 are close to relaxed after 40–50 kyr while M118 requires the full additional 80 kyr to achieve the same state.

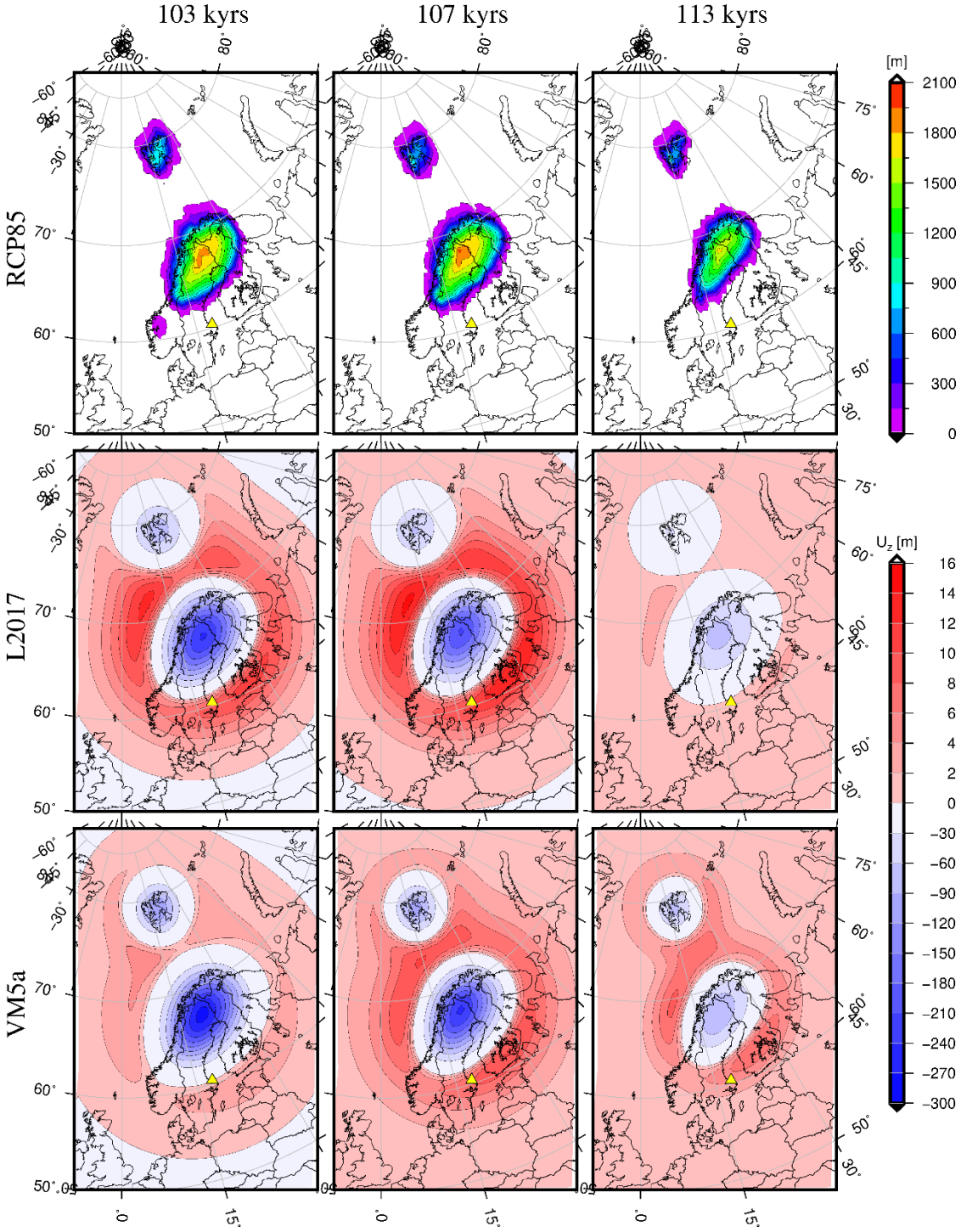

Figure 5-3. *RCP85 ice sheet model (top) and resulting vertical displacement, Uz, field in Northern Europe for earth models L2017 (middle) and VM5a (bottom) at times 101 (left), 103 (middle) and 105 kyr (right) into the model (as indicated in Figure 5-2). Note the different scales used for uplift (red) and subsidence (blue). Contour between white and light red marks the node line (no displacement relative to the start of the model). The location of Forsmark is marked by a yellow triangle.*

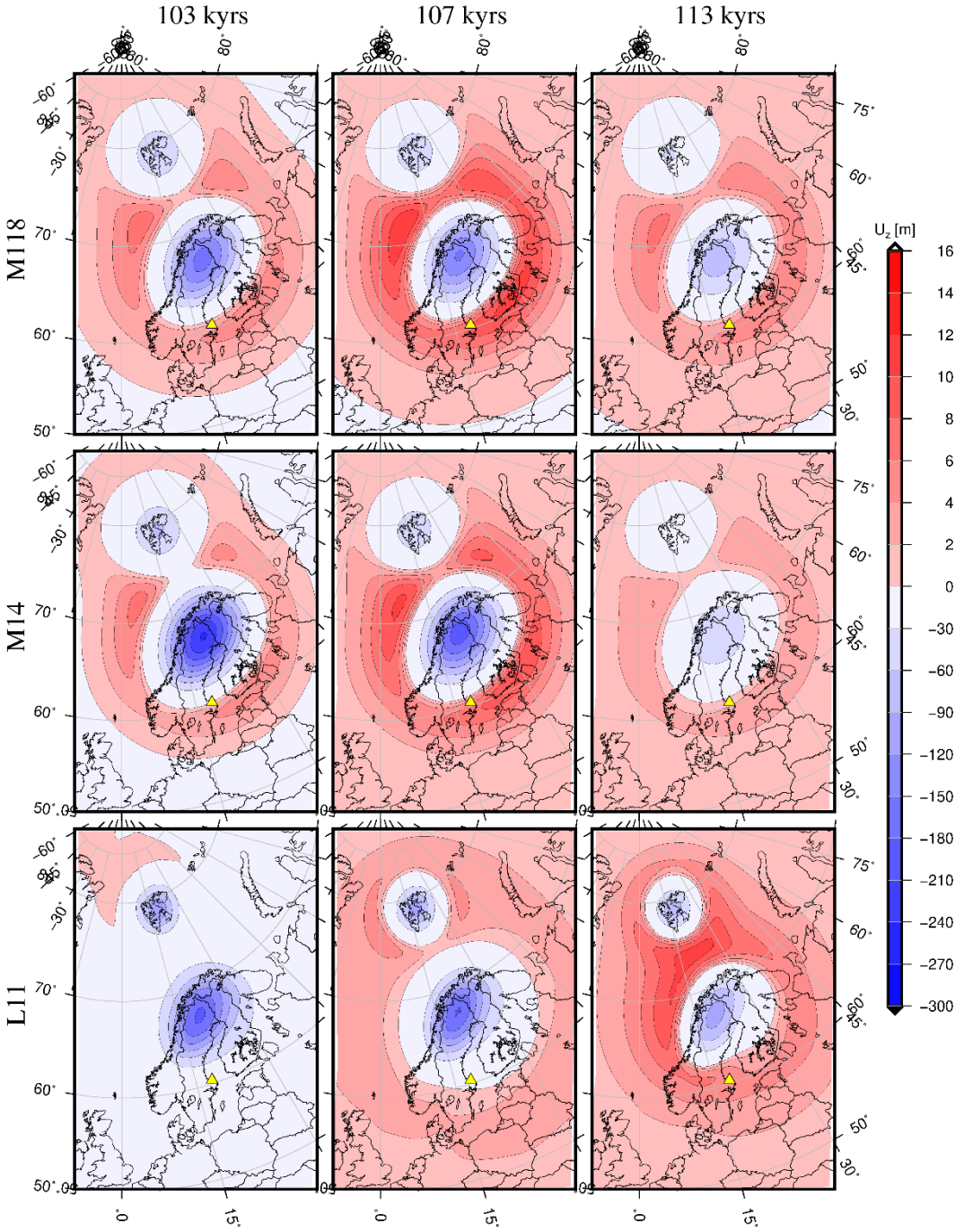

Figure 5-4. *Vertical displacement, Uz, fields in Northern Europe for earth models M118 (top), M14 (middle) and L11 (bottom) loaded by the RCP85 ice sheet at selected times (as indicated in Figure 5-2, see Figure 5-3 for the ice sheet). Note the different scales used for uplift (red) and subsidence (blue). Contour between white and light red marks the node line (no displacement relative to the start of the model). The location of Forsmark is marked by a yellow triangle.*

5.2 Impact of extended glacial maximum on vertical displacements

In order to investigate how far away from isostatic equilibrium the earth models are at glacial maximum in the different ice models we introduce a hiatus of 25 and 50 kyr of constant ice configuration following GM (Table 3-1) in the UMISM, NH40 and RCP45e models. We only test the earth models M14, VM5a and L11. Figure 5-5 displays the vertical surface displacements at Forsmark for all the perturbed glacier models on all the considered earth models.

Neither the UMISM nor the NH40 models with extended GM offer any surprises in Figure 5-5, subsidence continues although the load is constant, indicating that isostatic equilibrium is not reached. We saw already above how the subsidence continues in the original models for a few kyr after the GM, indicting non-equilibrium at the GM in both the NH40 and the UMISM. For the UMISM, we also noted in section 3.2 that following the GM there is a period of 3.9 kyr during which the ice load changes only slightly before the fast deglaciation phase sets in. Taken together, these two arguments explain why we see a continued subsidence after GM for both the NH40 and the UMISM reconstructions and why this lasts longer under the UMISM ice sheet. As Figure 5-5 shows for NH40 and the UMISM, even after a GM hiatus of 50 kyr, during which subsidence increases approximately 20 % from the start of the hiatus, subsidence is still increasing for all three earth models.

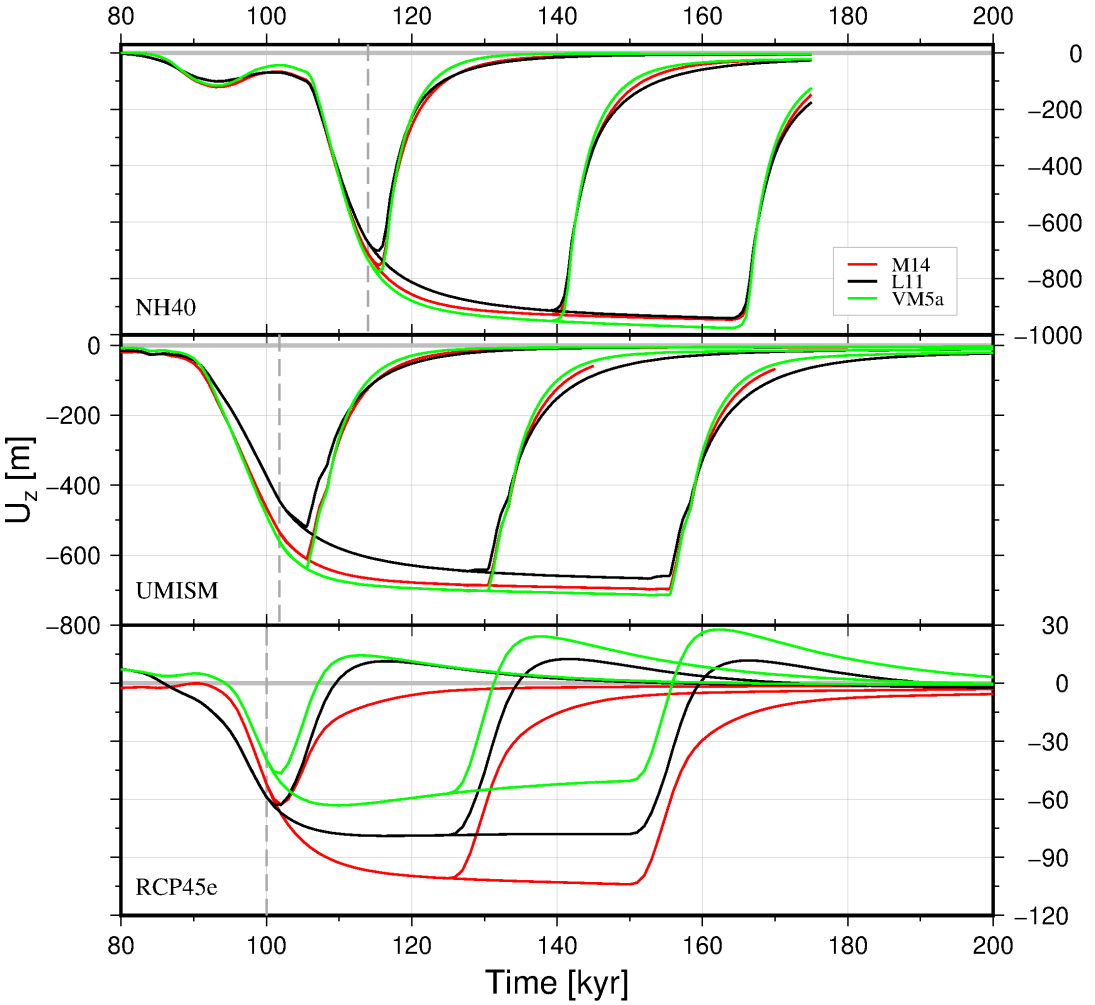

Figure 5-5. *Vertical displacement, Uz, at Forsmark for earth models M14 (red), L11 (black) and VM5a (green) loaded by NH40 (upper panel), UMISM (middle panel) and RCP45e (lower panel) ice sheets in their original ice configuration as well as with their respective GM ice configuration extended by 25 kyr and 50 kyr. Vertical dashed line displays the timing of GM in each ice sheet.*

The vertical displacements at Forsmark under the load of the RCP45e ice sheet and its extended versions show a greater complexity. While all three earth models initially continue to subside following the onset of the GM hiatus, only the M14 earth model continues to subside throughout the entire duration of the hiatus. The L11 earth model appears to reach isostatic equilibrium already after approximately 17 kyr, but this is an erroneous conclusion as we shall see when we study the stress evolution during the hiatus (and actually L11 starts to slowly uplift after 17 kyr). The subsidence at Forsmark in the VM5a model peaks after 10 kyr of GM hiatus after which it starts to uplift again. Following the end of the hiatus, during the deglaciation phase, the fore-bulge migrates in over Forsmark in both the L11 and the VM5a earth models and we note that the more the subsidence at Forsmark has decreased during the hiatus, the greater is the peak uplift during the deglaciation phase. As seen before, in the M14 earth model the fore-bulge never migrates in over Forsmark. We previously explained the differences between the earth model responses during and after the deglaciation phase as being due to differences in the flexural rigidity. This is also the plausible explanation for the behaviour observed here. The M14 earth model has a uniform elastic thickness of 120 km. While the elastic thickness in the L11 earth is 130 km locally beneath Forsmark, it quickly decreases to 60 km (Figure 4-1) towards the ice-sheet, lowering the effective flexural rigidity to below that of M14 despite the greater local elastic thickness. Consequently, the sensitivity to distant parts of the ice sheet quickly decreases. Over shorter time spans (a few kyr), the effective elastic thickness in the VM5a model is 100 km. However, the lower 40 km of the lithosphere in the VM5a model is in fact viscoelastic, albeit with a high viscosity. Thus, over longer time spans the effective elastic thickness in the VM5a model, as seen by the GIA process, decreases allowing for shorter wavelength deformations, i.e. an area gets more sensitive to the local load and less affected by load at a distance. As the RCP45e ice sheet margin barely covers Forsmark, the vertical displacement at Forsmark at GM is governed by distant parts of the ice-sheet. Since the effective flexural rigidity in the VM5a model decreases during the GM hiatus, the effect is that the vertical displacement at Forsmark decreases with time.

5.3 Impact of repeated glaciations on vertical displacements

Figure 5-6 shows the vertical displacement at Forsmark for the RCP45 and RCP45x ice histories for all earth models, as well as the difference between the RCP45 and RCP45x displacements. We see that the ice sheet prior to 73 kyr makes a significant difference in the GIA response at the onset of the next glaciation phase. As the ice grows, the previous ice load becomes less and less important. For the stiffest earth model, M118, the difference is appreciable even at the later glacial maximum, where the difference amounts to 38.7 m, about 10 % of the total vertical displacement. At the end of the model time (120 kyr) the difference has shrunk to 17.6 m. Whether or not this is a significant difference depends on the intended use of the predicted displacements, as well as on uncertainties in the ice sheet simulation.

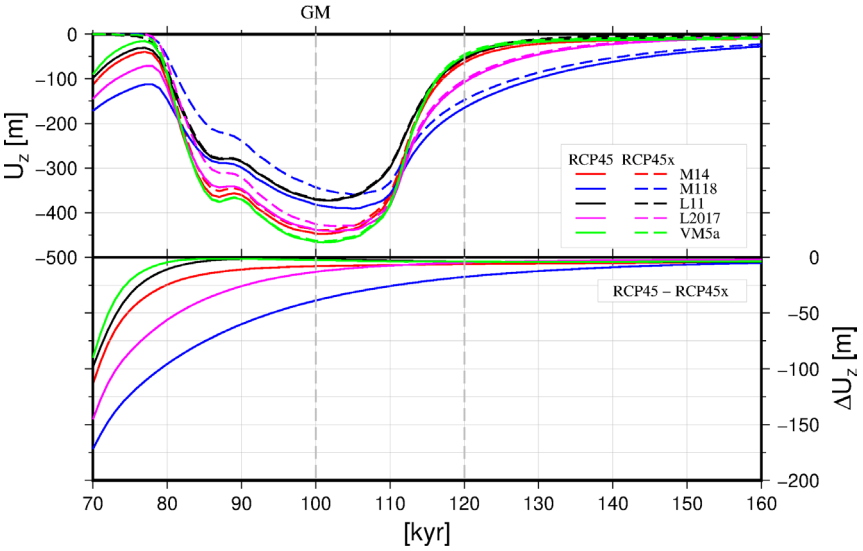

Figure 5-6. *Vertical displacement, Uz, at Forsmark for earth models M14 (red), M118 (blue), L11 (black), L2017 (magenta) and VM5a (green line) loaded by the RCP45 (solid) and RCP45x (dashed) ice sheet models. Upper panel shows U_z while lower panel shows the difference in U_z for each earth model loaded with the two ice sheet models. Vertical dashed lines indicate the glacial maximum (GM) and the last time step of the ice model.*

6 Glacially induced stresses

In this section we present the stress field in the upper crust induced by the ice-sheet models in the studied earth models. For the full field over Fennoscandia, stresses are presented at 2.5 km depth due to the resolution of the regional models. With a total of 25 ice-sheet – earth model combinations only the maximum horizontal stress, S_H, and maximum shear stress, $t_{max} = (S_1 – S_3)/2$, at GM and EOG (Table 3-1) are presented (S_1 and S_3 being the maximum and minimum principal stresses respectively). Locally at Forsmark we present the temporal evolution of S_H including declination, the minimum horizontal stress, S_h , the vertical stress, S_z , and t_{max} at 500 m depth. Finally, we present the impact on S_H of an extended GM ice sheet configuration as well as multiple glaciations. As is common in Earth Sciences we consider compressive stresses positive.

Stress tensors beneath Forsmark from all 25 ice-sheet - earth model combinations as well as the 18 models with extended GM configuration have been extracted from 500 m to 14.5 km depth at 1 km intervals every 1000 year throughout the simulations. These data are accompanying this report as ASCII files together with a README file describing the models, file format and file naming convention.

6.1 Maps of the glacially induced stress field at glacial maximum

Maps of the glacially induced S_H at GM (seen in Figure 3-3 and Figure 3-4 and defined in Table 3-1) are shown in Figure 6-1 to Figure 6-5 while maps of t_{max} are shown in Figure 6-6 to Figure 6-10. Each figure consists of five maps showing the response of the individual earth models for a particular ice sheet. In the maps of S_H, the magnitudes are shown by colours and contour lines while the directions are shown by short black bars.

As expected, we see in Figure 6-1 to Figure 6-5 that the ice models have first order impact on the magnitudes and directions of the induced S_H at GM, whereas the various earth models modulate the general behaviour of the induced stresses. The NH40 ice induces the highest S_H magnitudes of all ice models, spread over a significantly larger area than the other ice models. The UMISM and RCP45 ice models also induce relatively high S_H magnitudes in the areas of maximum ice cover, and have, as does NH40, positive S_H stretching out over the North Sea to Great Britain where there is an ice bridge. The RCP45e and RCP85 ice models have significantly less ice and produce smaller areas of positive S_H, with lesser magnitudes. All models clearly show the transition from positive S_H under the ice load to negative S_H outside the load, with directions of S_H, in a general sense, being perpendicular to the long axis of the load under the ice and parallel to the load outside the ice. This behaviour of the direction of S_H can be understood from how the elastic lithosphere bends. Directly beneath the load centre the curvature of the lithosphere will be concave, i.e. in the upper part of the lithosphere is under compression (positive normal stress) while in the lower part undergoes extension (negative normal stress). If the load is elongated, the curvature perpendicular to the elongation axis of the load will be the greatest hence the direction of S_H will be perpendicular to the load. As we move away from the load centre, the curvature will switch from concave to convex indicating extension in the upper part of the lithosphere (negative normal stress) and compression in the lower part (positive normal stress) in the direction perpendicular to the load axis (or radially to the load centre). The curvature parallel to the load axis is smaller, implying less negative normal stress. As we define S_H as the largest horizontal normal stress (i.e. least negative in case both S_H and S_h are negative), the direction of S_H outside the load will flip to being parallel to the load axis (or perpendicular to the radial direction to the load centre). Note that the change from convex to concave curvature of the lithosphere in the direction perpendicular to the load axis (radial from the load centre) does generally not coincide with the node line between subsidence and the fore-bulge. Likewise, the curvature of the lithosphere parallel to the load axis (or perpendicular to the radial direction to the load centre) will not necessarily change from convex to concave or back in the same location (consider e.g. a saddle point), hence the change in the sign of S_H will generally not occur in the same region as the flip of the S_H direction. Finally, stretching of the lithosphere will further modulate the stress magnitudes and hence potentially both the sign and direction of S_H.

Forsmark is located in areas of positive S_H at the GM in ice models NH40, UMISM and RCP45 but in negative, or close to zero, S_H in models RCP45e and RCP85. Directions of S_H at Forsmark vary depending on the ice sheet considered but not so much between the earth models loaded by the same ice sheet, with the exception of the L11 earth model where an eastward rotation is seen when loaded by the larger ice sheets NH40, UMISM or RCP45.

The results in Figure 6-1 to Figure 6-5 show that although magnitudes and directions vary slightly between earth models, they produce rather similar S_H distributions under the same load. The directions of S_H vary most significantly in the vicinity of the transition from positive to negative S_H whereas the magnitudes show a more uniform scale difference. Earth model L11, with the varying lithospheric thickness, shows the most deviating results compared to the flat models, with a clear asymmetry in the behaviour east and west of the load centre.

Figure 6-6 to Figure 6-10 show how t_{max} varies with ice and earth model at GM. Overall, we see the characteristic pattern for an ellipsoidal ice sheet (Lund et al. 2009), with high shear stresses below the major axis of the ice sheet, and around the edges of the ice sheet. The NH40 ice is so large that that pattern cannot be seen in the Fennoscandian area. As expected, the results vary more depending on the ice model than on the earth model. The NH40 ice sheet produces the largest induced shear stresses, in the area of Estonia. The earth models show similar patterns for the same ice model, albeit with varying shear stress magnitudes. The highest shear stresses are observed in models M118 and L2017, indicating that the stronger mantle, especially the stronger lower mantle, does not allow stress relaxation as quickly as the weaker models. For ice model UMISM, the lower slope of the ice in the east produces slightly lower shear stress magnitudes in the east than in the west, where the slope is higher, albeit over a larger area. Again, models M118 and L2017 produce higher shear stresses than the other earth models but the difference is not as large as for the NH40 ice. The RCP45 ice sheet produces a more symmetrical pattern than the UMISM, but the magnitudes of shear stress are similar. The smaller RCP45e and RCP85 ice sheets induce correspondingly smaller shear stresses.

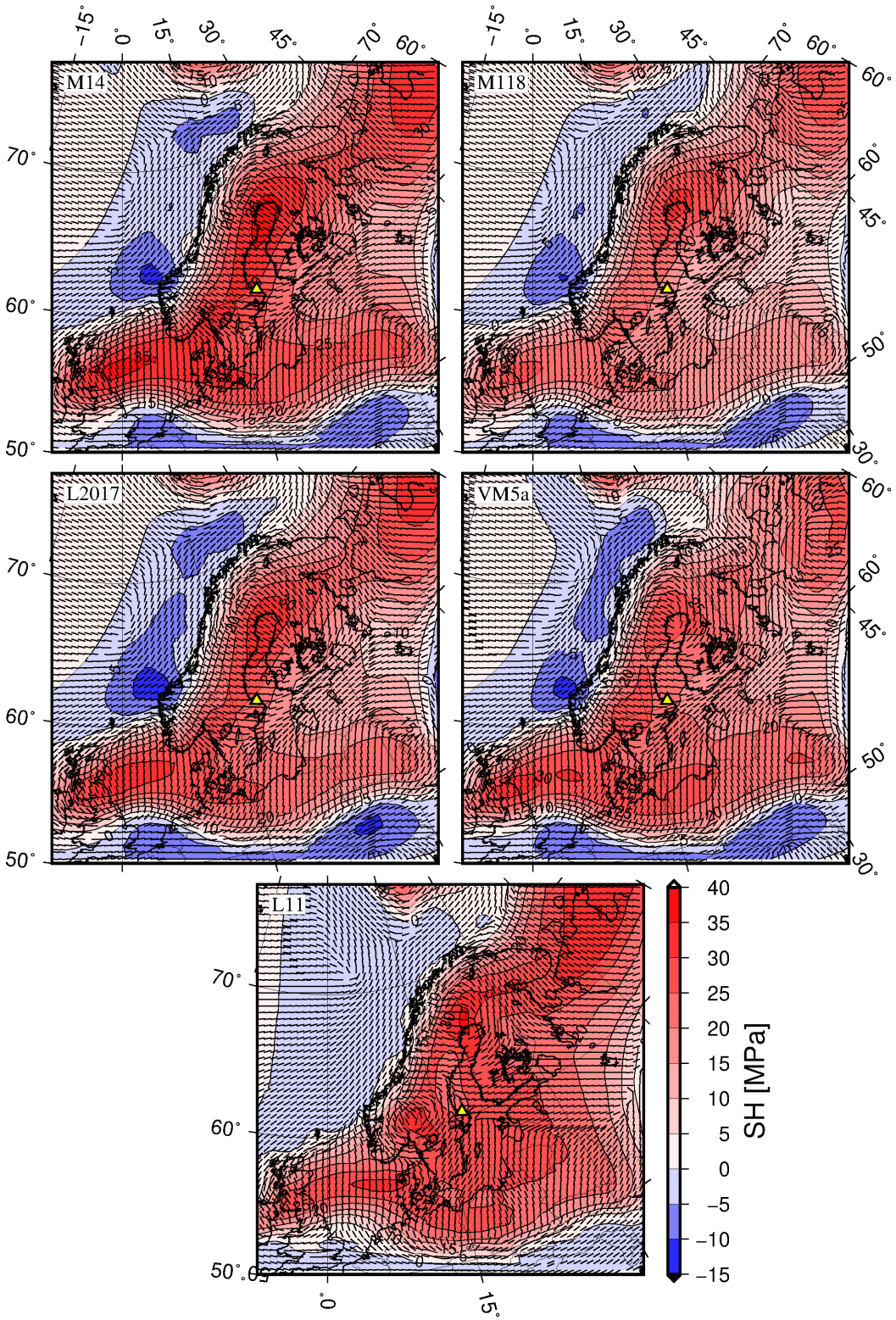

Figure 6-1. *Magnitude (color) and direction (black bars) of the glacially induced maximum horizontal stress, S_H, at 2.5 km depth at GM of the NH40 Saalian type ice sheet for all earth models. Location of Forsmark is marked by a yellow triangle.*

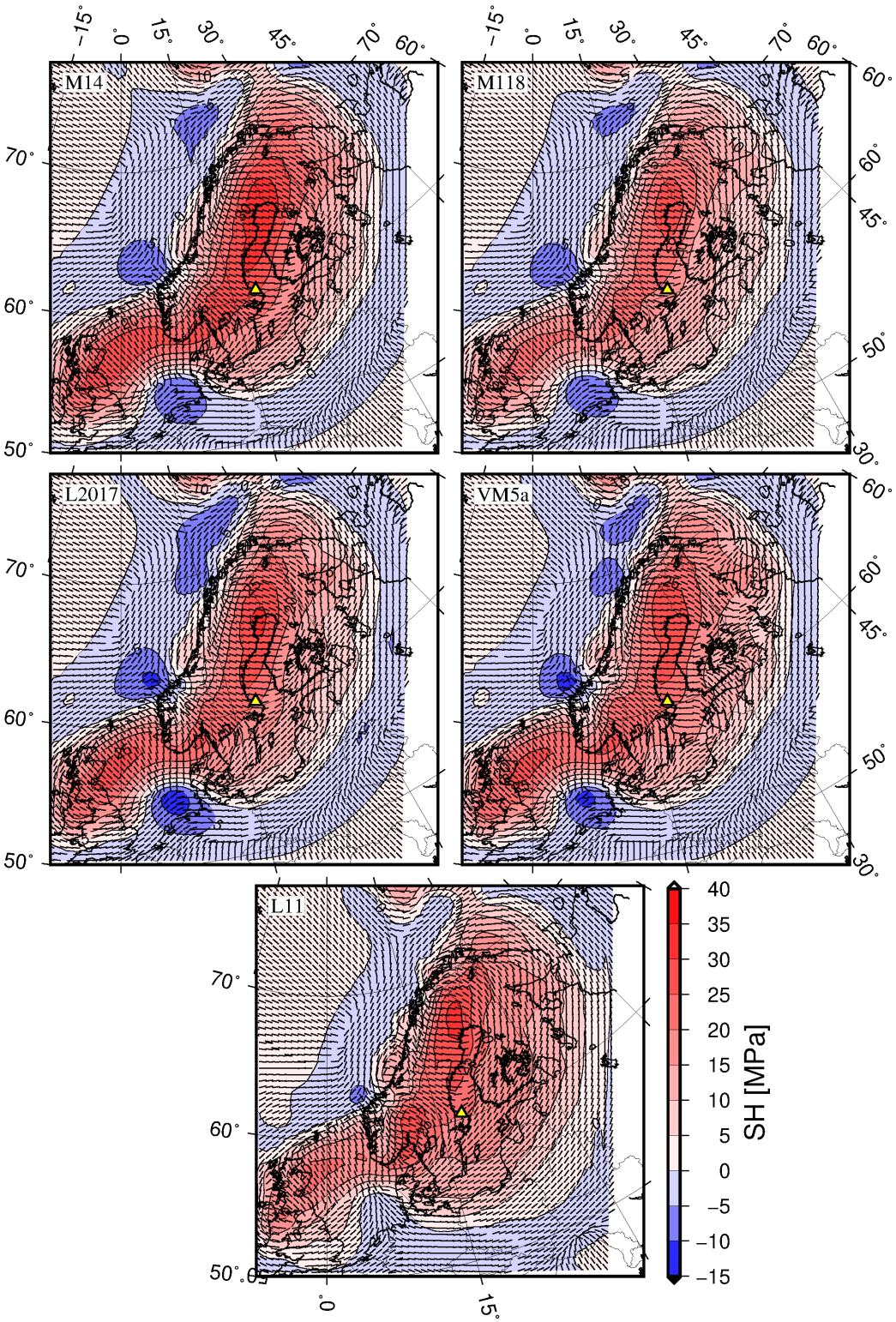

Figure 6-2. *Magnitude (color) and direction (black bars) of the glacially induced maximum horizontal stress, S_H, at 2.5 km depth at GM of the UMISM reconstruction of the Weichselian ice sheet for all earth models. Location of Forsmark is marked by a yellow triangle.*

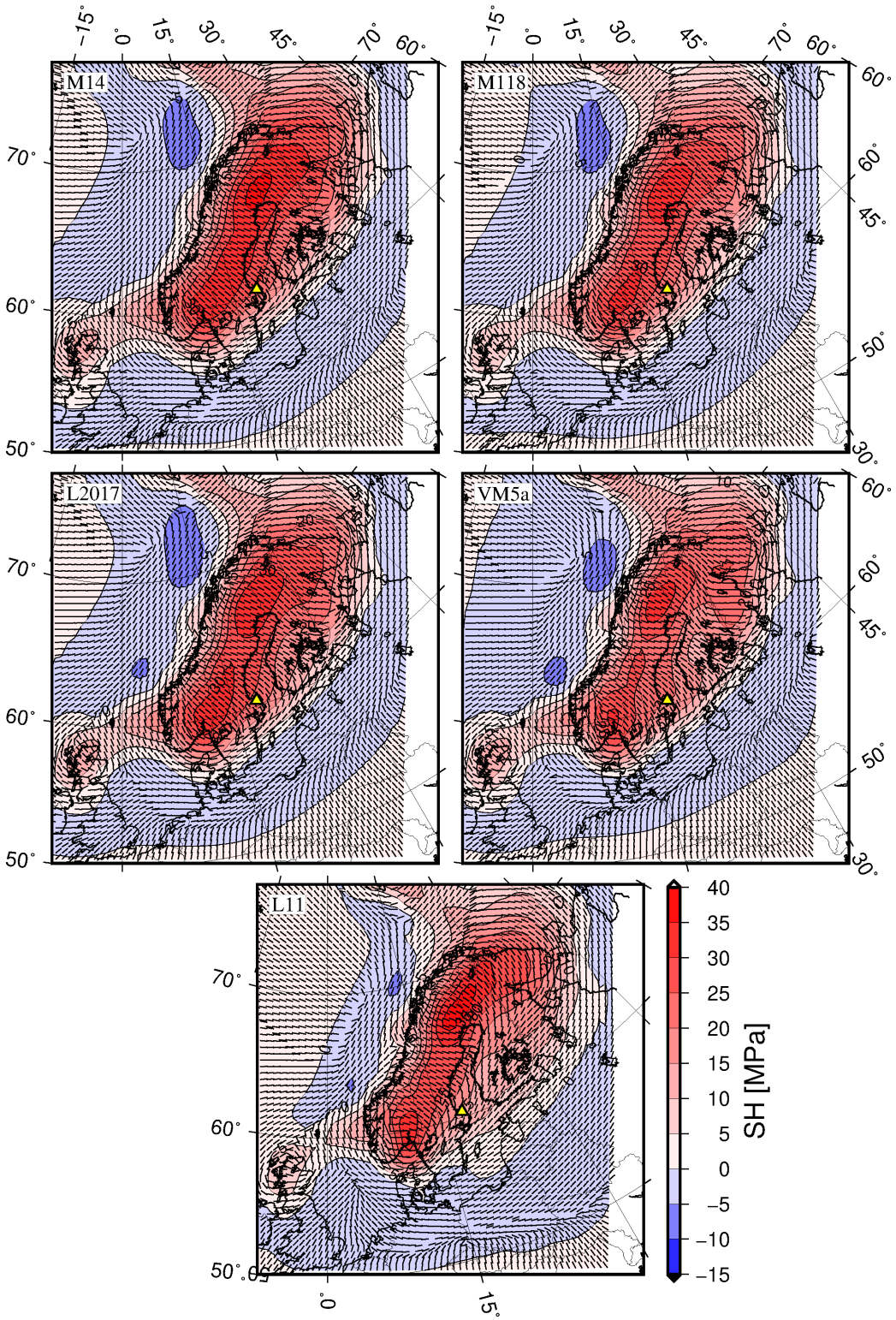

Figure 6-3. *Magnitude (color) and direction (black bars) of the glacially induced maximum horizontal stress, S_H, at 2.5 km depth at GM of the RCP45 ice sheet projection for all earth models. Location of Forsmark is marked by a yellow triangle.*

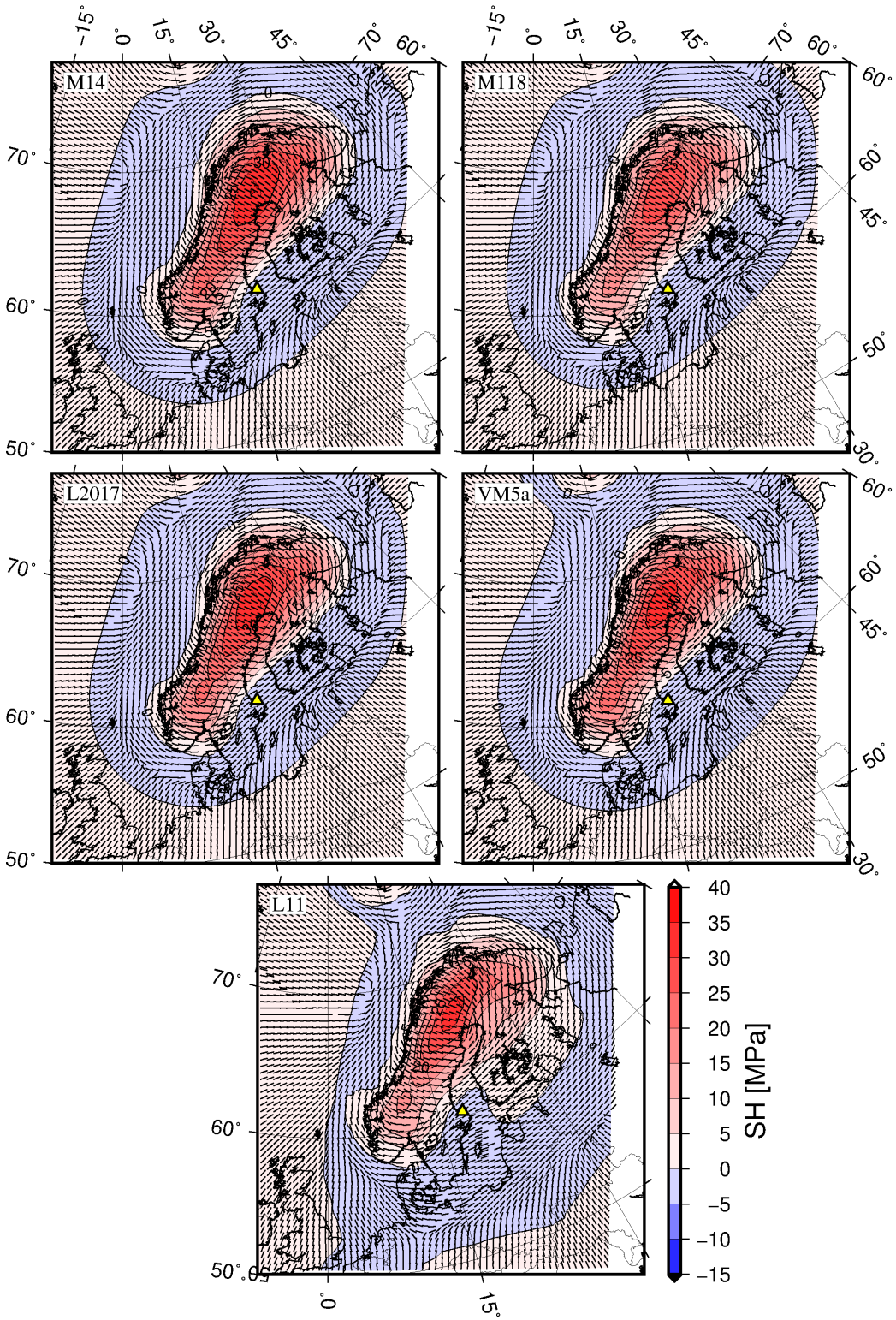

Figure 6-4. *Magnitude (color) and direction (black bars) of the glacially induced maximum horizontal stress, S_H, at 2.5 km depth at GM of the RCP45e ice sheet projection for all earth models. Location of Forsmark is marked by a yellow triangle.*

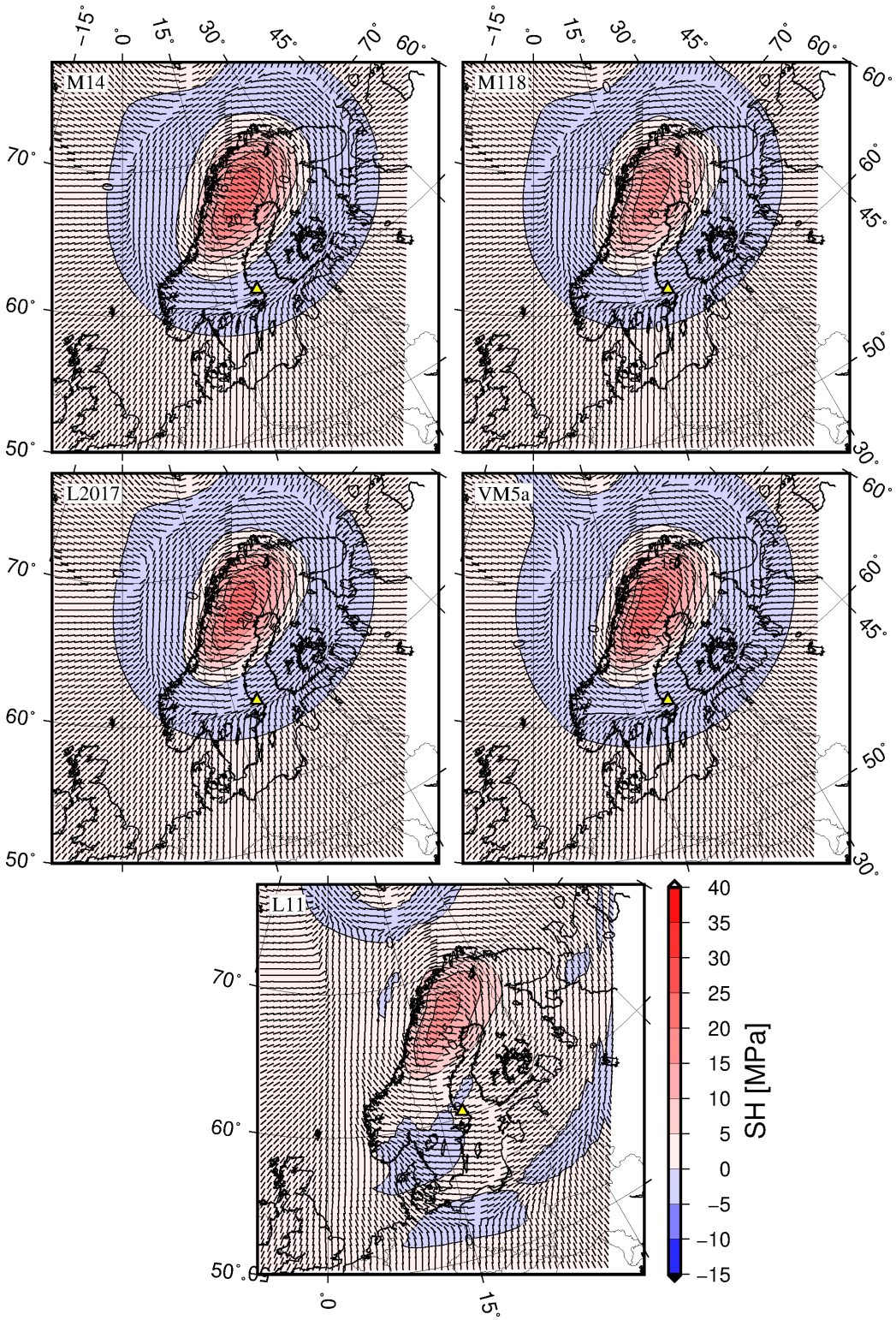

Figure 6-5. *Magnitude (color) and direction (black bars) of the glacially induced maximum horizontal stress, S_H, at 2.5 km depth at GM of the RCP85 ice sheet projection for all earth models. Location of Forsmark is marked by a yellow triangle.*

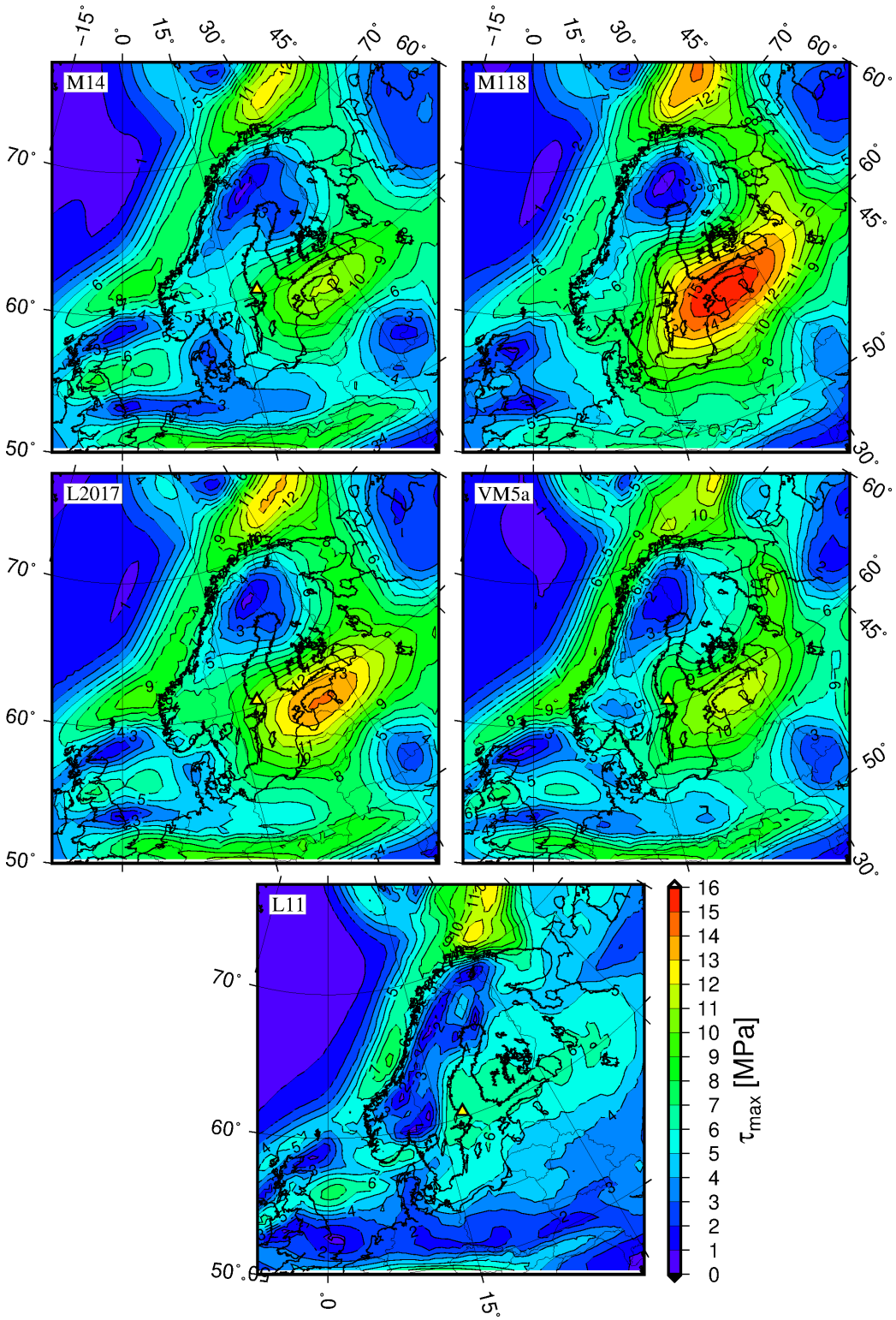

Figure 6-6. *Maximum glacially induced shear stress, t_{max}, at 2.5 km depth at GM of the NH40 Saalian type ice sheet for all earth models. Location of Forsmark is marked by a yellow triangle.*

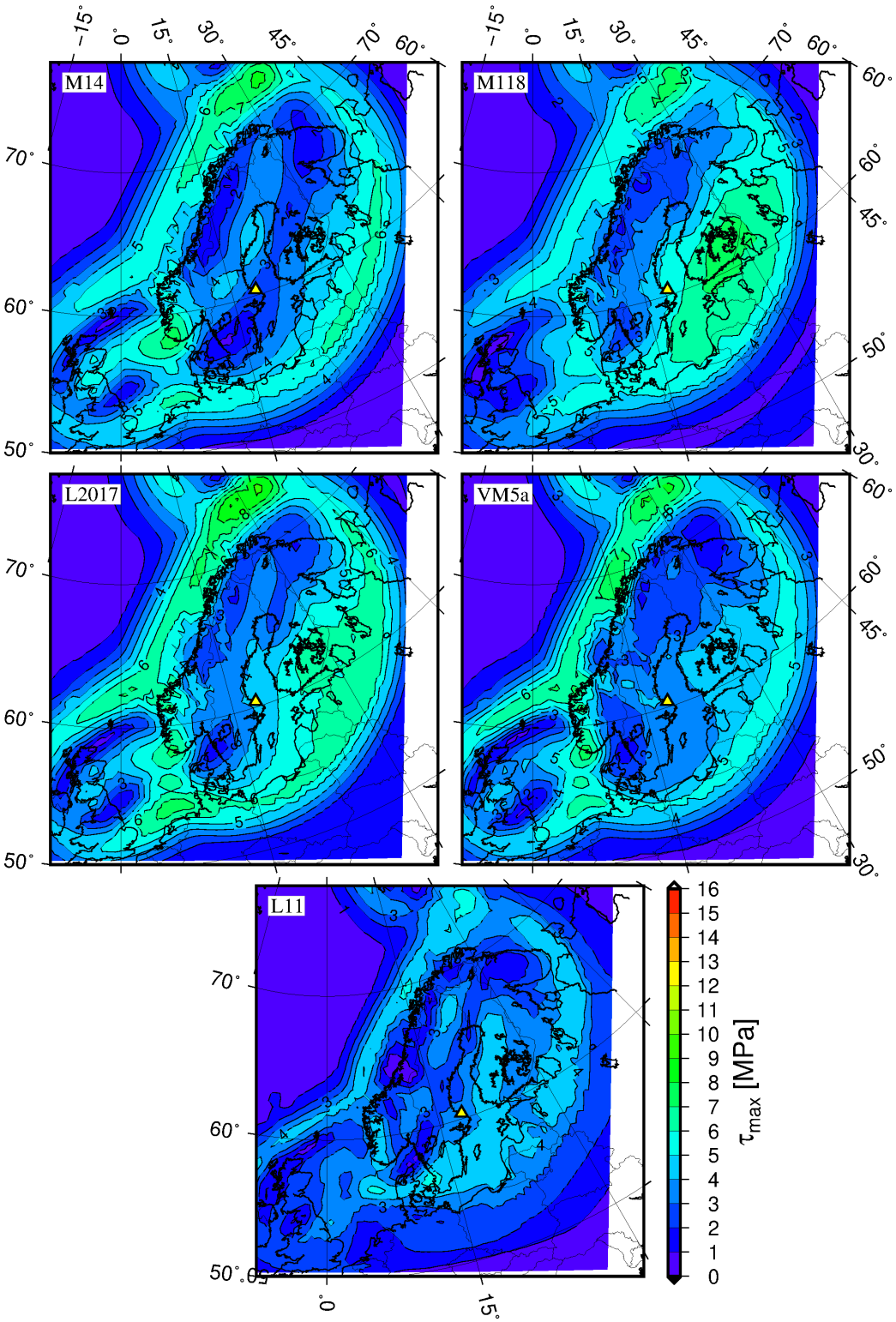

Figure 6-7. *Maximum glacially induced shear stress, t_{max}, at 2.5 km depth at GM of the UMISM Weichselian ice sheet reconstruction for all earth models. Location of Forsmark is marked by a yellow triangle.*

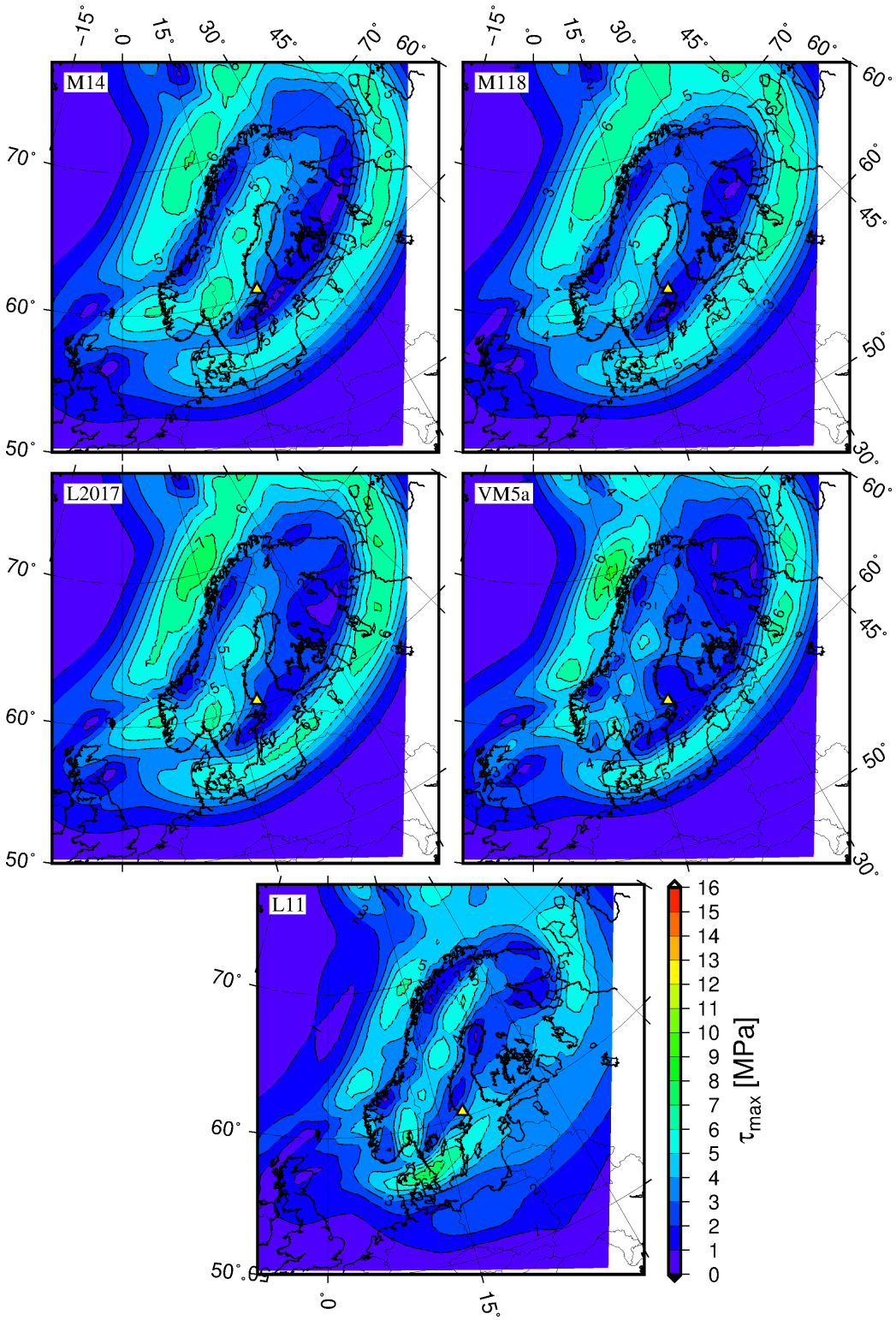

Figure 6-8. *Maximum glacially induced shear stress, t_{max}, at 2.5 km depth at GM of the RCP45 ice sheet projection for all earth models. Location of Forsmark is marked by a yellow triangle.*

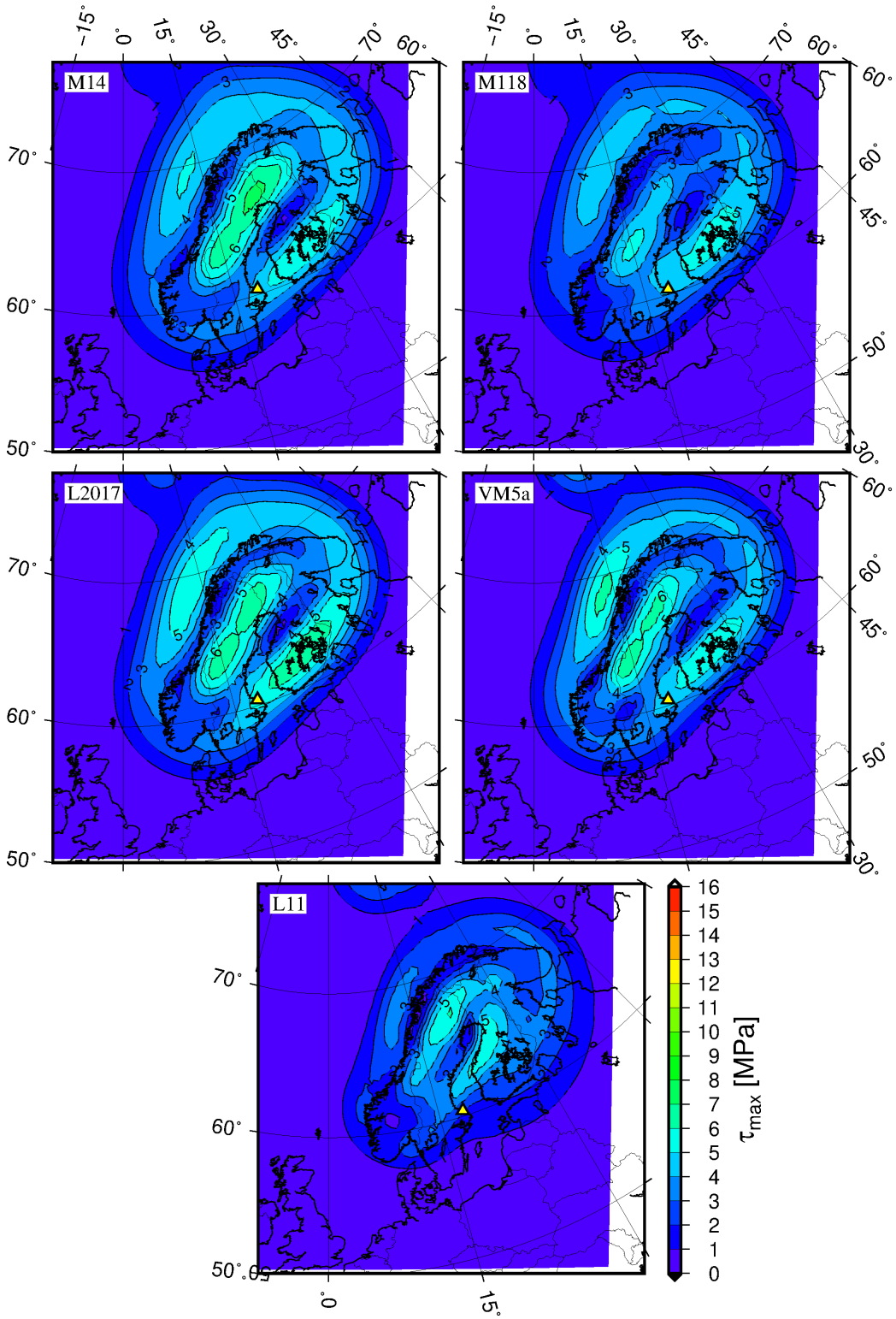

Figure 6-9. *Maximum glacially induced shear stress, t_{max}, at 2.5 km depth at GM of the RCP45e ice sheet projection for all earth models. Location of Forsmark is marked by a yellow triangle.*

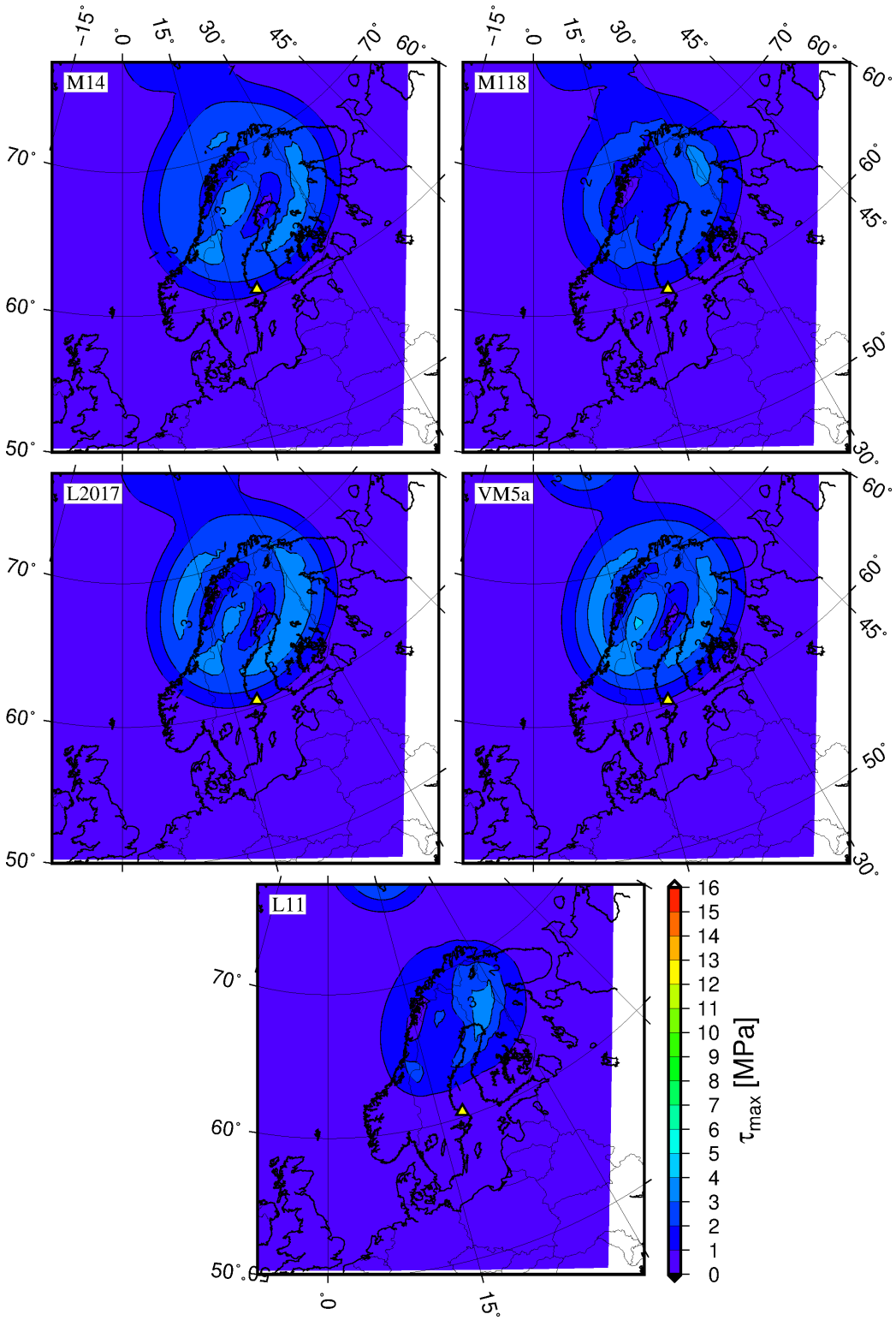

Figure 6-10. *Maximum glacially induced shear stress, t_{max}, at 2.5 km depth at GM of the RCP85 ice sheet projection for all earth models. Location of Forsmark is marked by a yellow triangle.*

6.2 Maps of the glacially induced stress field at the end of glaciation

Maps of the glacially induced S_H at EOG (seen in Figure 3-3 and Figure 3-4 and defined in Table 3-1) are shown in Figure 6-11 to Figure 6-15 while maps of t_{max} are shown in Figure 6-16 to Figure 6-20. Each figure consists of five maps showing the response of the individual earth models for a particular ice sheet. In the maps of S_H, the magnitude is shown by colours and contour lines while the direction by short black bars. The ice over Fennoscandia has mostly disappeared with at most some remnants up in the Scandes mountains in some of the ice sheet models. The induced vertical stress has therefore decreased to approximately zero. The flexure of the lithosphere under the former ice sheet, however, preserves horizontal stresses which decrease during glacial rebound.

Figure 6-11 to Figure 6-15 show the magnitude and direction of S_H at the EOG. We see that the pattern is generally rather similar to the pattern at the glacial maximum, for the same ice and earth model combination, but that the stresses are generally lower. In some models the nodal line between positive and negative S_H migrates inward but this is not the case for all models, or all areas in an individual model. Stress directions are generally preserved beneath the long axis of the former ice sheet while away from this, stress rotation can be observed in some regions but in others not. For the larger ice sheets, the VM5a earth model produces slightly lower stresses than the other earth models. Differences between the earth models are, however, not very large. Worth pointing out is also that while the S_H field is similar to the U_z field (compare leftmost maps in Figure 5-3 and Figure 5-4 to Figure 6-15) differences do exist, especially in the location of the node line (i.e. the separator between positive and negative U_z and S_H) of respective field, hence the S_H field at a particular location cannot be directly deciphered from the U_z field. This can easily be understood as the stress is not primarily a function of the displacement but rather the strain which is a tensor where the components are the spatial partial derivative of the displacement vector.

Figure 6-16 to Figure 6-20 show the t_{max} at the end of glaciation. The t_{max} distributions at the end of glaciation are rather different to those at the glacial maximum, as the largest t_{max} are now found under the centres of the former ice sheets. Much of the t_{max} distribution around the edges of the (former) ice sheet has become significantly lower in magnitude. It is interesting to note that the t_{max} are no longer largest in the models using the NH40 ice sheet, the models using the UMISM and RCP45 ice sheets focus the t_{max} at the end of glaciation more and induce higher shear. This is related to the size of the former ice sheet, the thickness of the elastic lithosphere and thus the amount of bending induced in the lithosphere. This was studied by Johnston et al. (1998), who found that there is an optimum relation between the size of the ice sheet and the thickness of the elastic layer which produces the largest shear stresses. None of the earth models consistently produces the highest, or lowest, t_{max} at the end of glaciation, instead the induced t_{max} show a rather intricate inter-dependency between the ice and earth models.

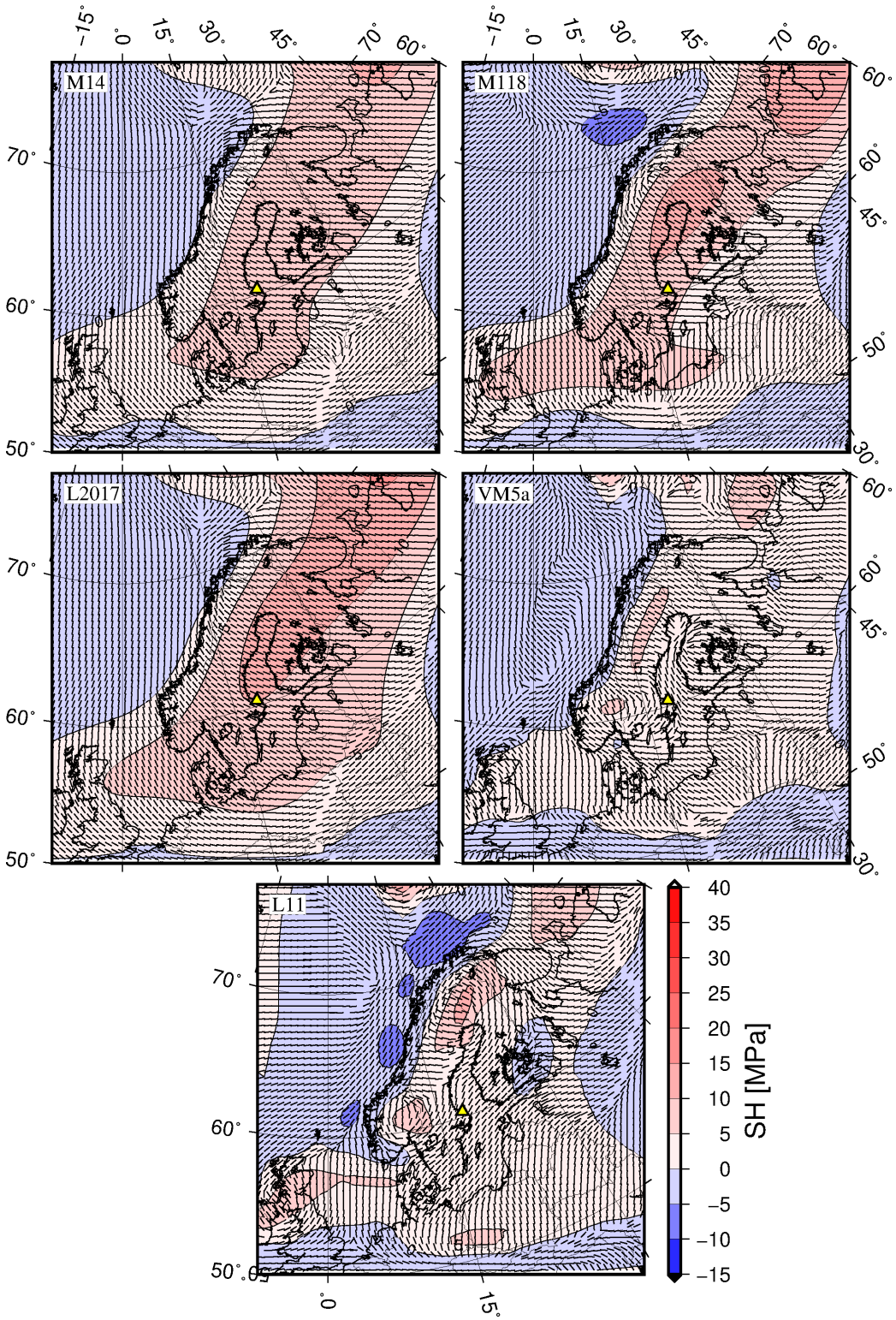

Figure 6-11. *Magnitude (color) and direction (black bars) of the glacially induced maximum horizontal stress, S_H, at 2.5 km depth at EOG of the NH40 Saalian type ice sheet for all earth models. Location of Forsmark is marked by a yellow triangle.*

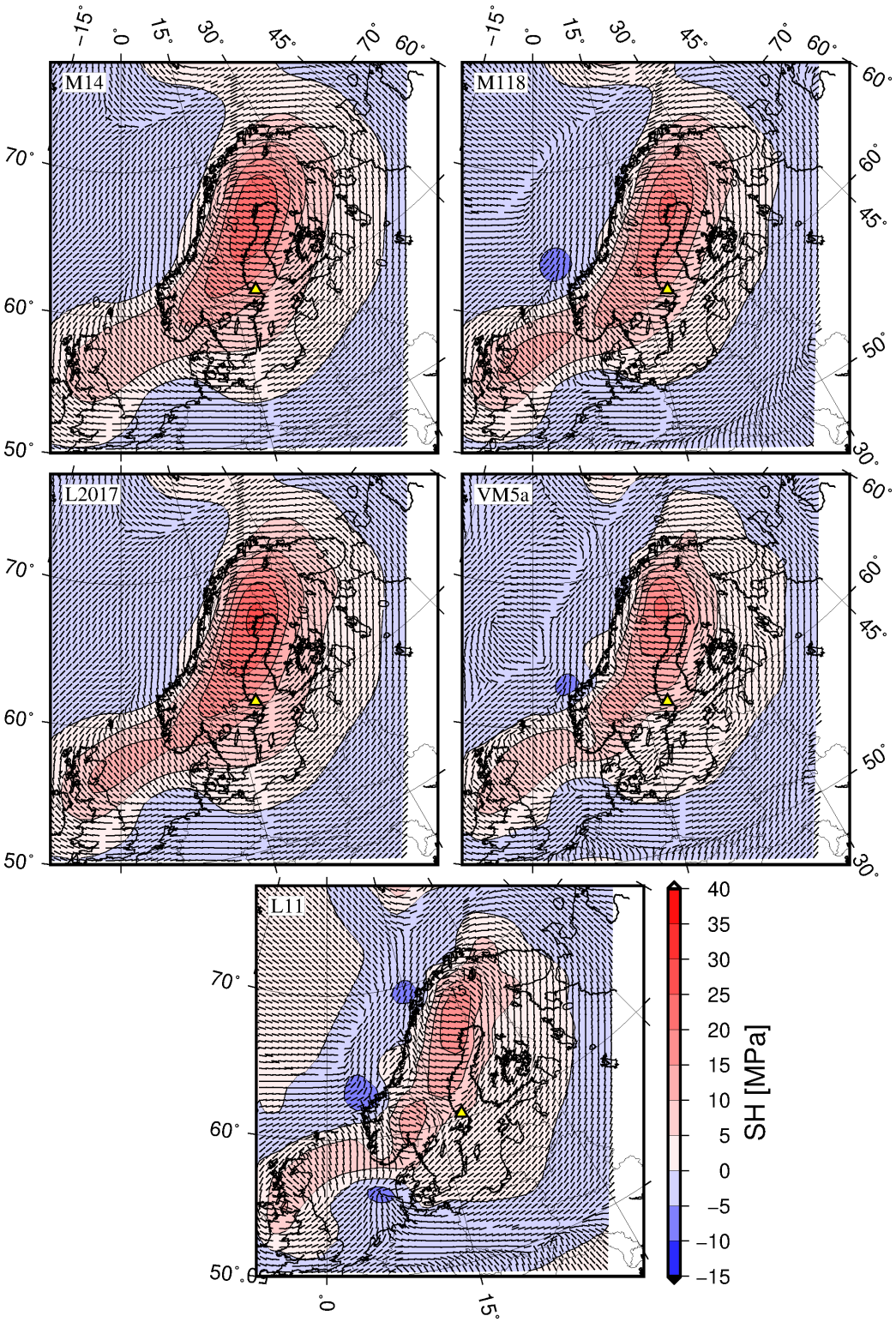

Figure 6-12. *Magnitude (color) and direction (black bars) of the glacially induced maximum horizontal stress, S_H, at 2.5 km depth at EOG of the UMISM Weichselian ice sheet reconstruction for all earth models. Location of Forsmark is marked by a yellow triangle.*

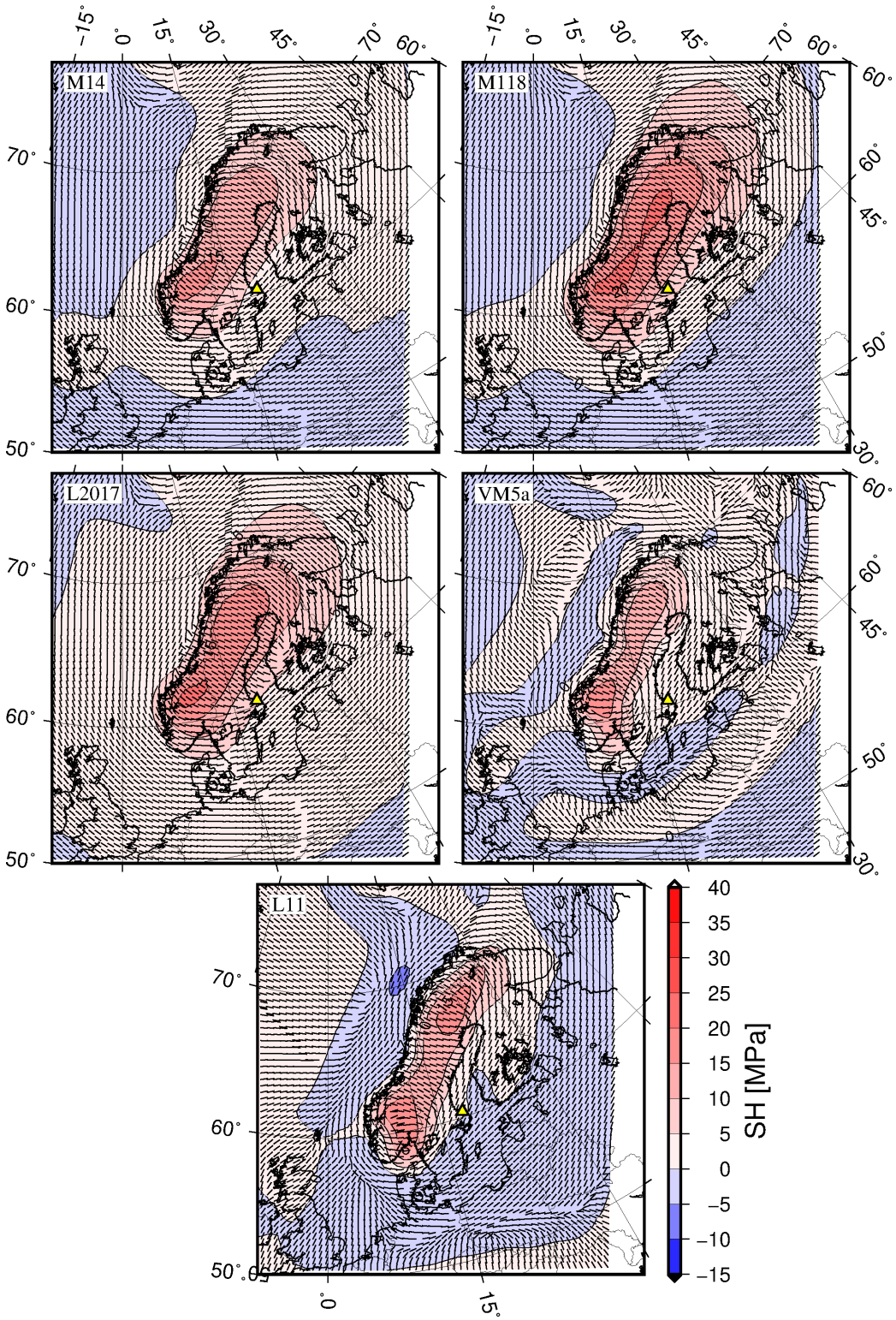

Figure 6-13. *Magnitude (color) and direction (black bars) of the glacially induced maximum horizontal stress, S_H, at 2.5 km depth at EOG of the RCP45 ice sheet projection for all earth models. Location of Forsmark is marked by a yellow triangle.*

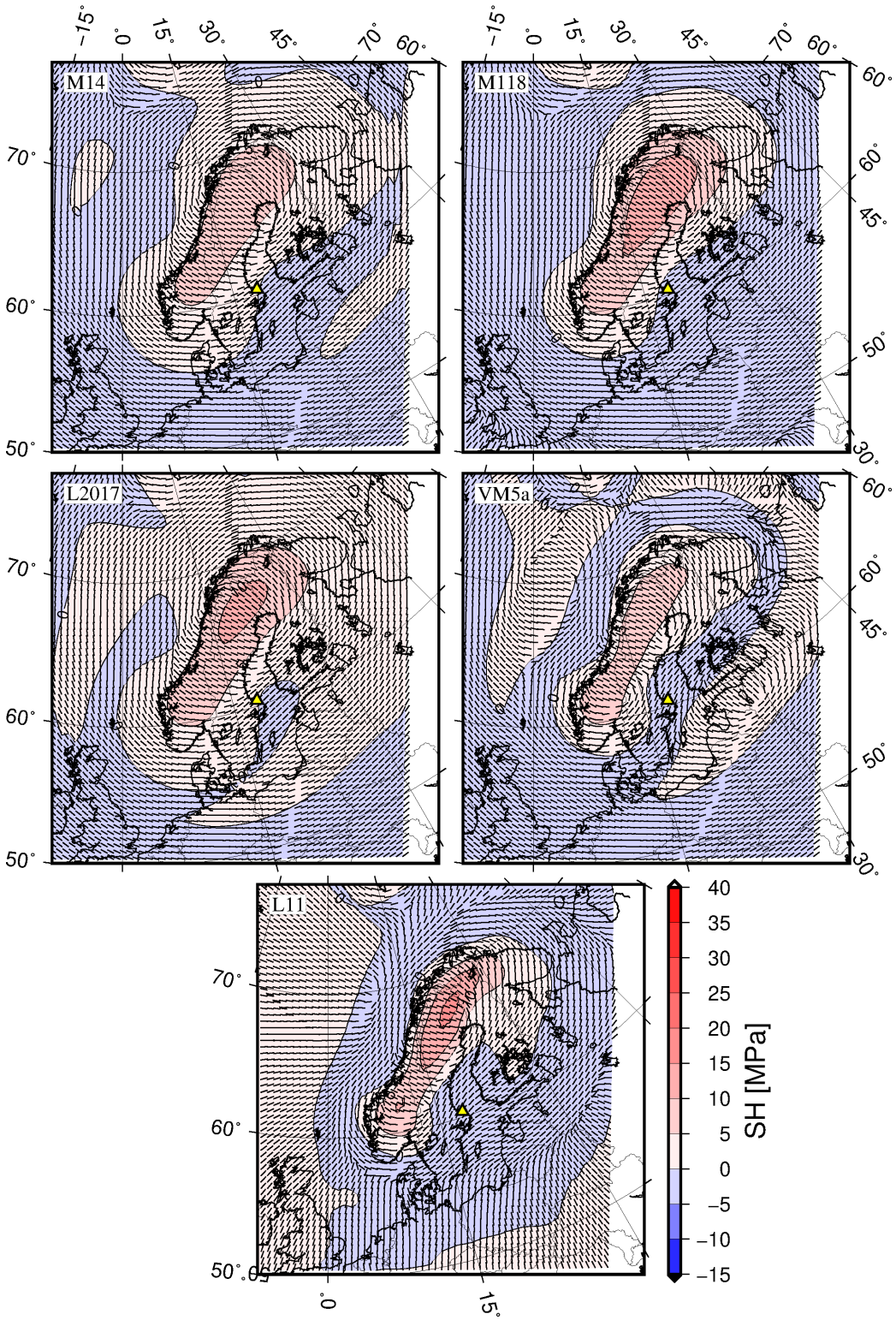

Figure 6-14. *Magnitude (color) and direction (black bars) of the glacially induced maximum horizontal stress, S_H, at 2.5 km depth at EOG of the RCP45e ice sheet projection for all earth models. Location of Forsmark is marked by a yellow triangle.*

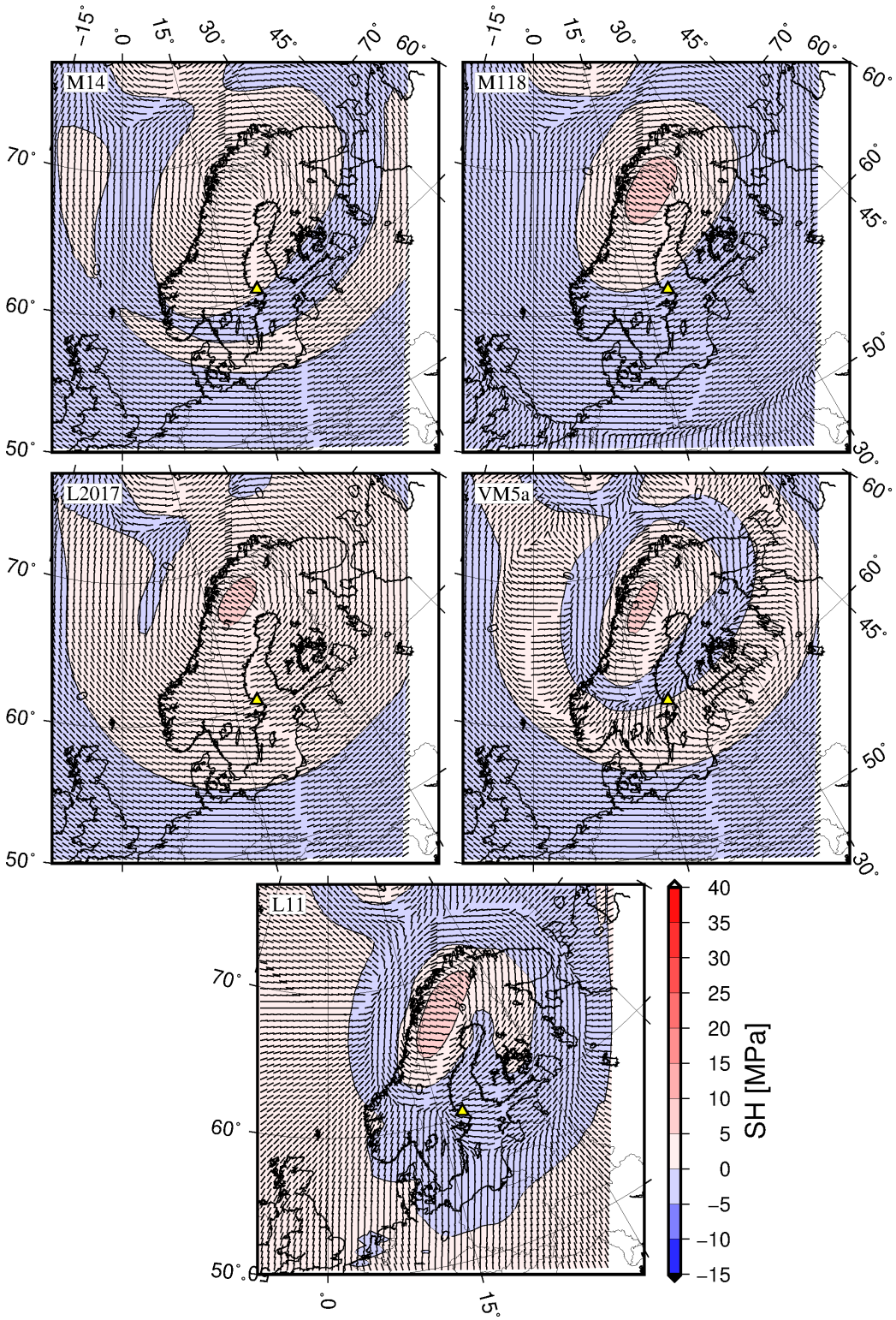

Figure 6-15. *Magnitude (color) and direction (black bars) of the glacially induced maximum horizontal stress, S_H, at 2.5 km depth at EOG of the RCP85 ice sheet projection for all earth models. Location of Forsmark is marked by a yellow triangle.*

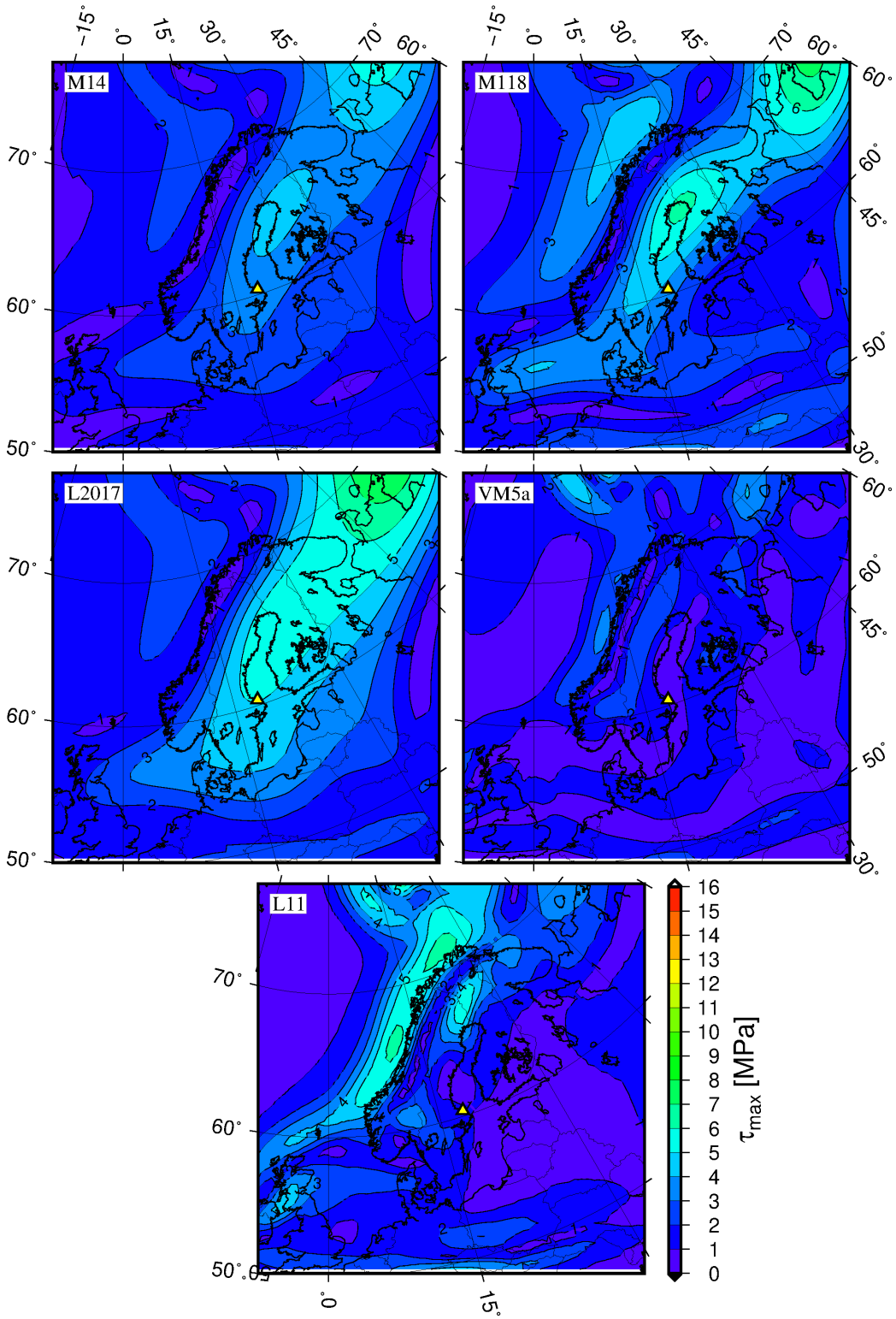

Figure 6-16. *Maximum glacially induced shear stress, t_{max}, at 2.5 km depth at EOG of the NH40 Saalian type ice sheet for all earth models. Location of Forsmark is marked by a yellow triangle.*

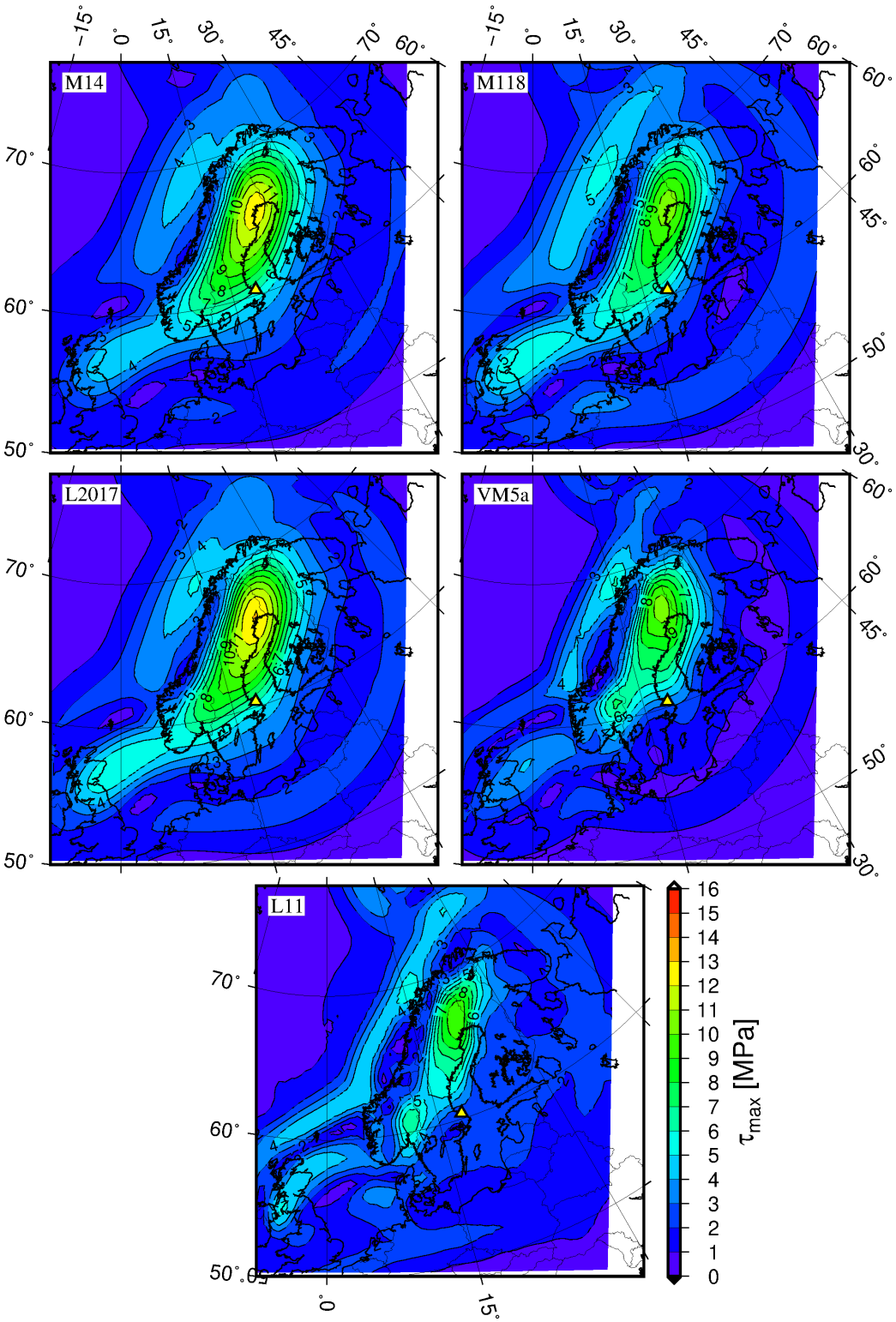

Figure 6-17. *Maximum glacially induced shear stress, t_{max}, at 2.5 km depth at EOG of the UMISM Weichselian ice sheet reconstruction for all earth models. Location of Forsmark is marked by a yellow triangle.*

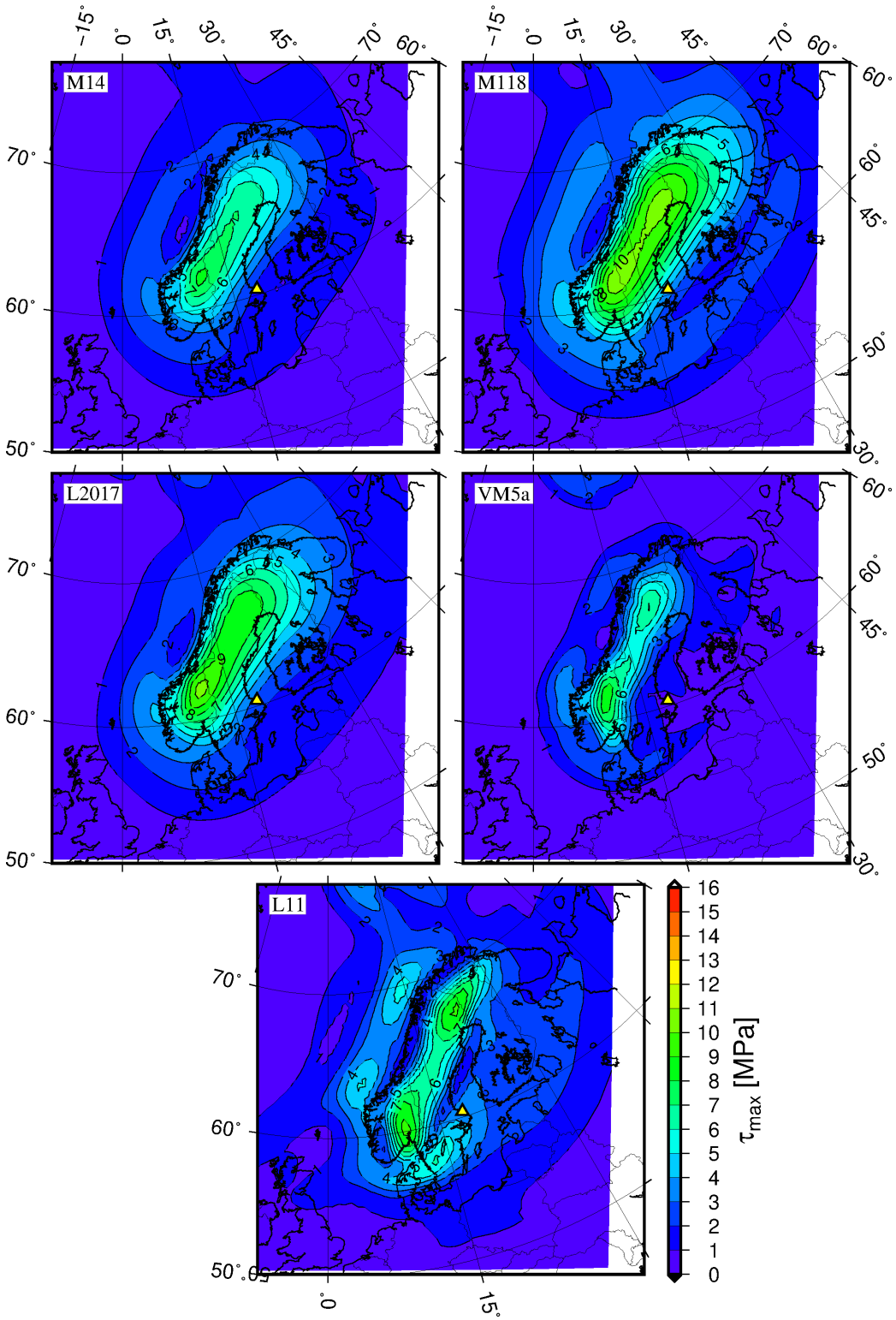

Figure 6-18. *Maximum glacially induced shear stress, t_{max}, at 2.5 km depth at EOG of the RCP45 ice sheet projection for all earth models. Location of Forsmark is marked by a yellow triangle.*

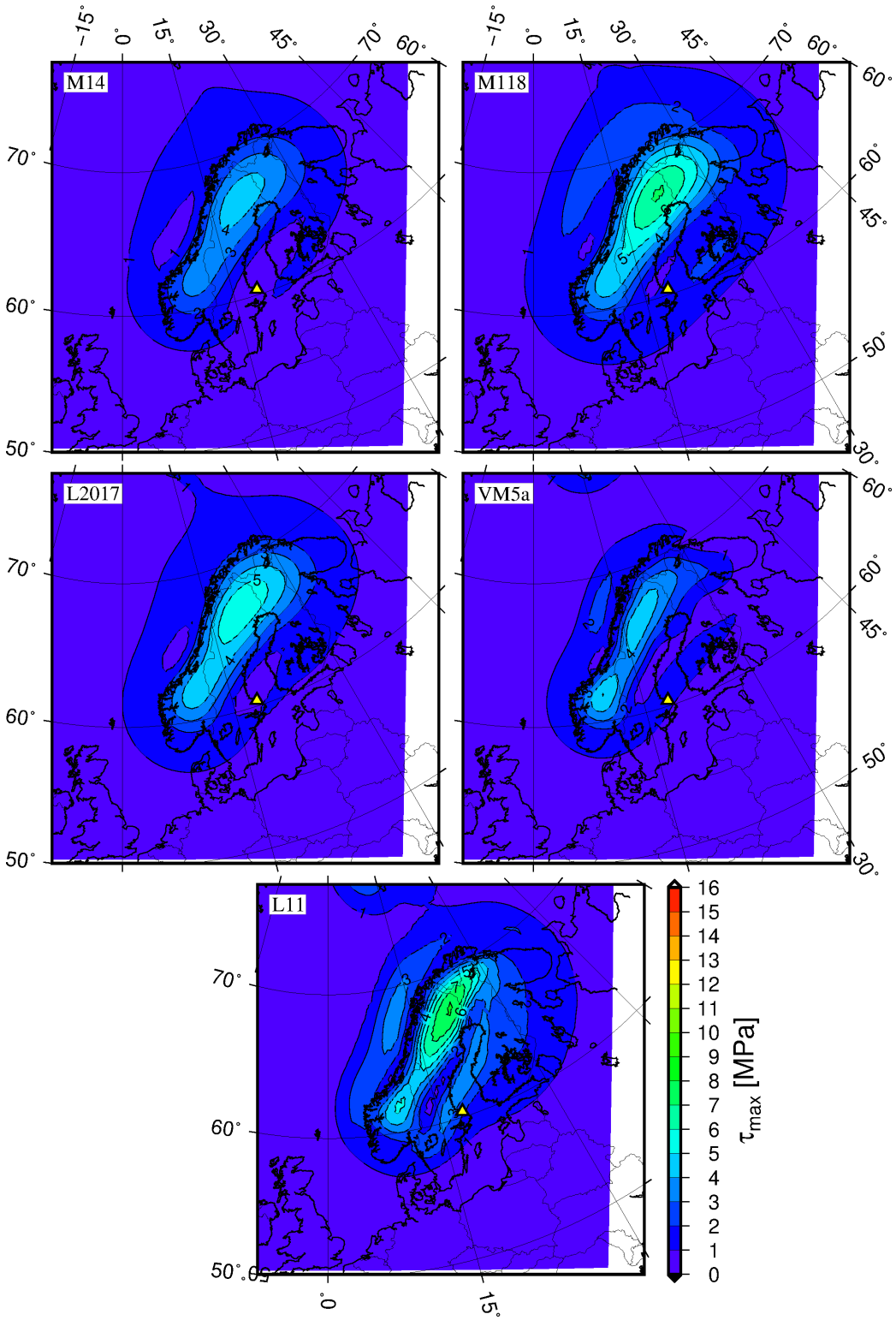

Figure 6-19. *Maximum glacially induced shear stress, t_{max}, at 2.5 km depth at EOG of the RCP45e ice sheet projection for all earth models. Location of Forsmark is marked by a yellow triangle.*

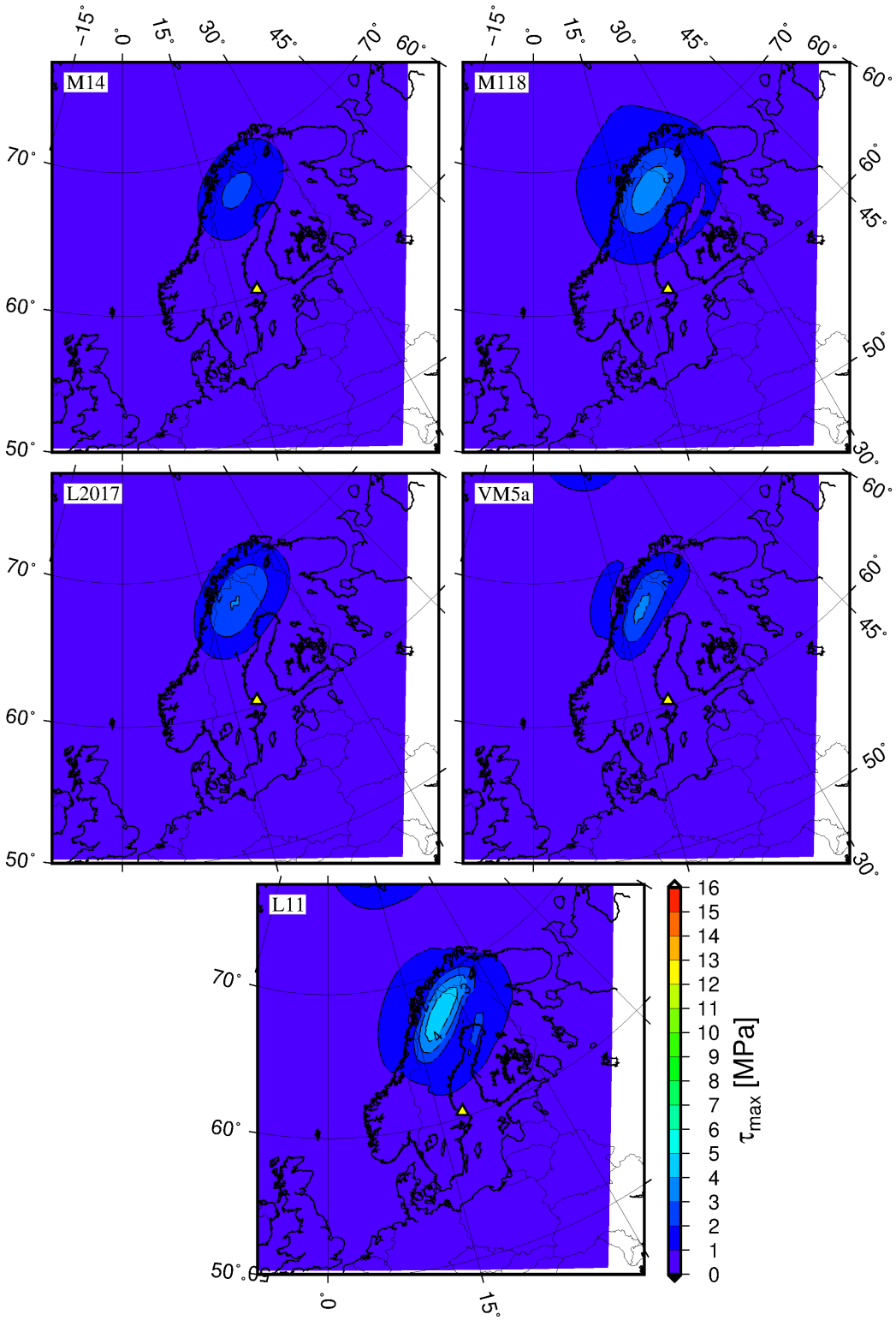

Figure 6-20. *Maximum glacially induced shear stress, t_{max}, at 2.5 km depth at EOG of the RCP85 ice sheet projection for all earth models. Location of Forsmark is marked by a yellow triangle.*

6.3 Temporal evolution of the induced glacial stresses at Forsmark

We study the stress field at Forsmark using a sub-modelling approach as described in section 2.1, which allows us to access stresses with a 1 km depth interval, starting from a depth of 500 m. Here we present the stress data at 500 m depth. As in the sections above we present the modelling result for one ice history at the time, with the five different earth model responses. We show the maximum horizontal stress (S_H) including declination, the minimum horizontal (S_h), the vertical (S_Z), and the maximum shear stress (t_{max}) through modelling time. A word of caution is warranted in that there is a 180-degree ambiguity in the S_H declination, this should be kept in mind while interpreting the plots of the S_H declination.

Using the large NH40 Saalian type ice model, Figure 6-21 shows both the effects of the significant growth of the ice sheet prior to arrival at Forsmark and the relatively short-lived peak of vertical stress at Forsmark, in agreement with the evolution of the ice cover seen in Figure 3-3. Prior to the ice-sheet margin arriving at Forsmark negative horizontal stresses develop. This can be observed prior to both periods of glacial coverage, with the effect even more pronounced in-between the two pulses, a period during which the volume and maximum thickness of the ice-sheet grows while the areal extent decreases. As the ice migrates in over Forsmark, an induced normal faulting stress state develops as the vertical stress increases to about 36 MPa but the S_H does not have time to develop to more than at most 30.4 MPa, in the M14 model (Figure 6-22, upper panel). The smallest S_H (18.2 MPa) is induced in the M118 earth model as a consequence of the model's strong mantle. It is to be noted that the peak S_H occurs 1 kyr after the GM, indicating, as discussed above, that the earth is far from isostatic equilibrium at the GM.

When the ice sheet rapidly retreats from Forsmark stresses decline quickly after which we see a transition to a more gradual decline in the horizontal stresses, governed by post-glacial rebound. During that transition, horizontal stresses increase in all earth models except L11. The magnitude and duration of this increase can be related to the viscosity of the mantle (the lower viscosity in the upper and lower mantle, the shorter transition period). However, in the case of the L11 earth model the thickening of the lithosphere to the east dampens the effect. During the post-glacial phase horizontal stresses in the VM5a and the L11 earth models become negative, related to them having the lowest mean viscosity in the activated part of the mantle.

The evolution of t_{max} is complex but in general we see an increase when the ice-sheet advances towards and in over Forsmark. Peak values are reached during the final advancement of the ice-sheet a few thousand years before GM. The orientation of S_H up until the second advancement of the ice-sheet in over Forsmark is in general in an NNE-SSW direction (Figure 6-22, lower panel). For models M14, M118, and L2017 the orientation flips counter-clockwise by 90 degrees once, or shortly after, the ice reaches Forsmark after which it stays this way for the rest of the simulation. For the L11 model the direction stays fairly the same, NNE-SSW, throughout most of GM, EOG and following post-glacial phase up until the last few kyrs of the simulation when it also flips into the same orientation as seen for models M14, M118, and L2017. The orientation of S_H induced by VM5a largely follows that of M14, M118, and L2017 up until EOG when it initially flips clockwise by 90 degrees to a NW-SE direction, as seen for the L11 model, followed by a gradual rotation over a period of 4-5 kyr into a N-S direction that mostly remains for the remainder of the simulation.

The glacially induced stresses at 500 m depth in Forsmark under the influence of the UMISM ice sheet (Figure 6-23) follows in general the same pattern as observed for the NH40 ice sheet. The main difference being that the difference in magnitude of S_H and S_Z are smaller during the peak of glaciation over Forsmark. In fact, in the M14 earth model the induced S_H grows larger than S_Z shortly following the GM during the ~ 4 kyr long period during which the UMISM displays a short hiatus prior to the deglaciation phase (Figure 3-3). While S_H grows largest in the M14 model (Figure 6-24, upper panel) and is smallest in the M118 model (29.2 MPa and 20.4 MPa respectively) at 14.5 kyr BP, peak S_H in the VM5a is slightly larger than peak S_H in the L11 at GM, opposite to what is seen under the load of the NH40 ice-sheet.

t_{max} in Forsmark under the UMISM load display similar trends as under the NH40 load in the sense that t_{max} increase as the ice-sheet advances towards and in over the area. However, during the period Forsmark is ice covered, with the exception of L11 and M118 and the first larger ice coverage in Forsmark, t_{max} decrease. This was also seen during the first smaller ice-coverage in NH40 while in the later, larger, ice-coverage in NH40 t_{max} continued to increase for a few kyr. The different behaviors can be understood from the interplay between the speed at which the ice sheet increases in thickness and the stiffness of the model. In a model with higher viscosity the bending of the lithosphere occurs over a longer timescale than in a weaker model, i.e. horizontal stresses build up slower. If at the same time there is a fast increase of the load S_Z will increase faster than Sh. Thus, with S_Z and S_h approximately equal to S_1 and S_3 it follows that t_{max} will increase if a fast load increase is imposed on a stiff earth model (such as L11 and M118). A second peak in t_{max} can be seen as the ice withdraws from the region, i.e. with the exception discussed above t_{max} peak when the UMISM ice-sheet margin passes Forsmark. A notable difference between the t_{max} under NH40 and UMISM is seen between the two periods of thicker ice coverage in Forsmark. Under the NH40 load t_{max} actually increase while under UMISM it initially decreases before starting to increase again. The difference can be understood from the differences in the two ice-sheets as seen in Figure 3-3. In the NH40 case the ice-sheet barely changes during this period and the margin is never further away from Forsmark than 100 km. In the UMISM case the ice-sheet shrinks significantly and initially withdraws so that the ice-sheet margin is 500 km away from Forsmark. As the UMISM ice-sheet start building up again and the ice-sheet margin approaches Forsmark we see how t_{max} once again increase to peak once the margin reaches the site.

The orientation of S_H under the UMISM load (Figure 6-24, lower panel) bear similarities to that which is seen under the NH40 load (Figure 6-22, lower panel). For the L11 earth model S_H is mostly oriented NNE-SSW up until the first glacial pulse after which the orientation rotates slightly to NE-SW. During the final glacial pulse, a more pronounced rotation towards an E-W orientation is seen followed by a return to a NE-SW orientation during the deglaciation and post-glacial phase. The S_H orientation in the other earth models are roughly the same throughout the simulation, the exception being the VM5a model. At early times, up until the first major pulse of ice over Forsmark the S_H orientations are identical to that of the L11 model. Halfway through the buildup of the ice the orientation flips by 90 degree to a NW-SE orientation only to rotate into an approximate E-W orientation during the withdrawl of the ice followed by yet another rotation into an NE-SW orientation similar to that of the L11 model. As the second major, and final, pulse of ice builds up SH orientation once again flips by 90 degree into a NW-SE orientation which then more or less remains throughout the remainder of the simulation. During deglaciation there is a small counterclockwise rotation, however M14, M118 and L2017 all recover from this while in VM5a the rotation continues throughout the postglacial phase all the way into an NE-SW orientation after which it reverses to reach an E-W orientation at the end of the simulation.

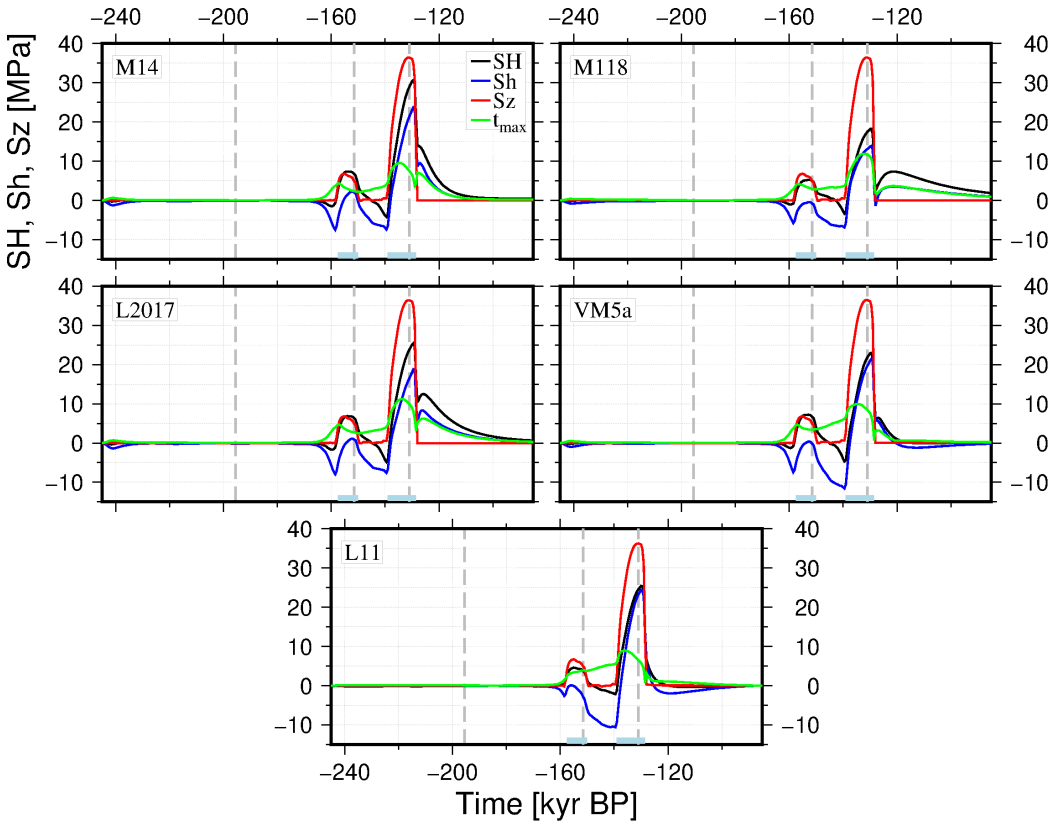

Figure 6-21. *Temporal evolution of maximum horizontal stress (S_H, black), minimum horizontal stress (S_h, blue) and vertical stress (S_Z, red) at 500 m depth beneath Forsmark for all earth models, loaded by the NH40 Saalian type ice sheet. Dashed vertical lines indicate times for which the ice sheet is seen in Figure 3-2 and Figure 3-3. Ice coverage at Forsmark is indicated by light blue bar at base of each plot.*

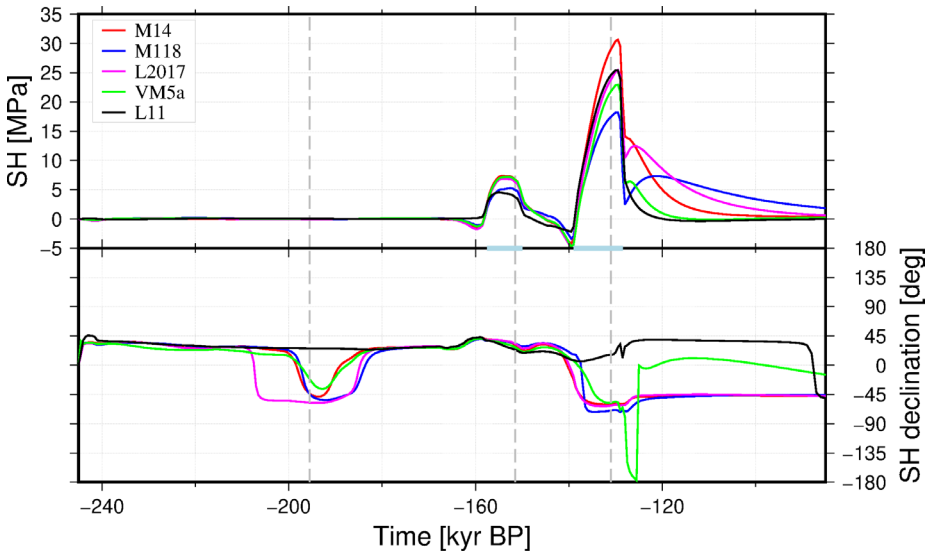

Figure 6-22. *Temporal evolution of maximum horizontal stress, S_H, upper panel, and S_H declination, lower panel, at 500 m depth beneath Forsmark for M14 (red), M118 (blue), L11 (black), L2017 (magenta) and VM5a (green) loaded by the NH40 Saalian type ice sheet. Vertical dashed lines indicate times for which the ice sheet is seen in Figure 3-2 and Figure 3-3. Ice coverage at Forsmark is indicated by light blue bar at base of each plot.*

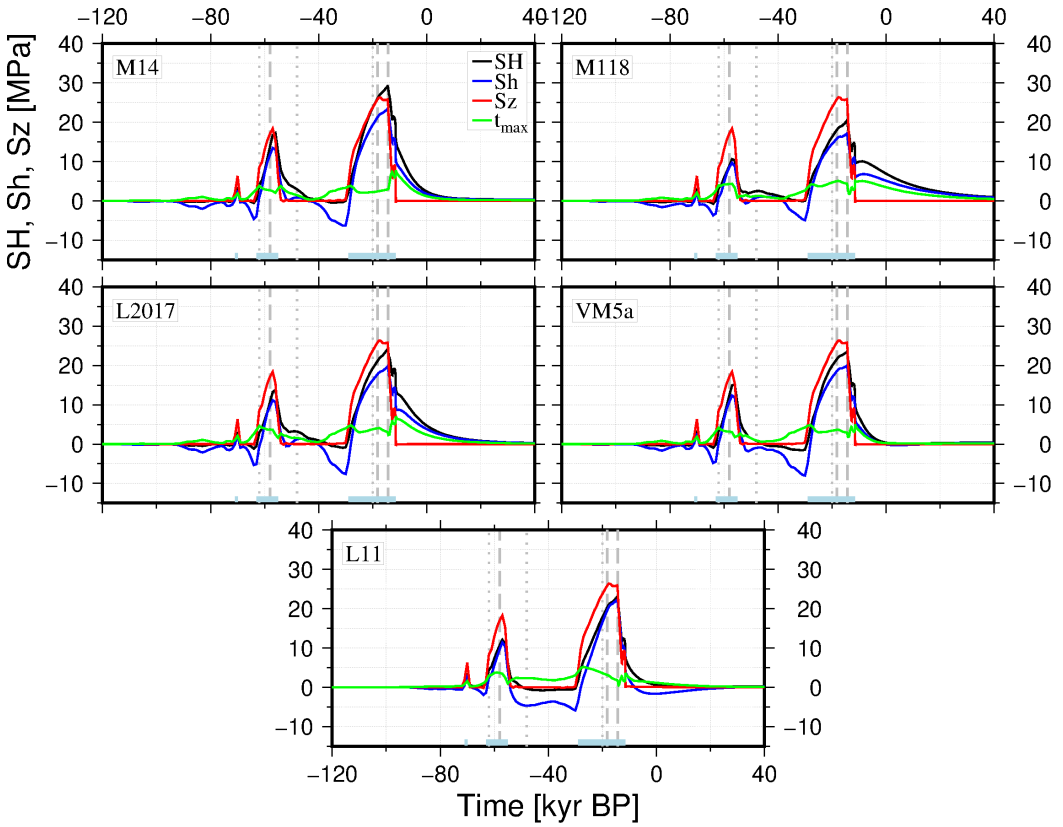

Figure 6-23. *Temporal evolution of maximum horizontal stress (S_H, black), minimum horizontal stress (S_h, blue) and vertical stress (Sz, red) at 500 m depth beneath Forsmark for all earth models, loaded by the UMISM Weichselian ice sheet reconstruction. Vertical dotted and dashed lines indicate times for which the ice sheet is seen in Figure 3-2 and Figure 3-3 (dashed) and Figure 3-4 and Figure 3-6 (dotted). Ice coverage at Forsmark is indicated by light blue bar at base of each plot.*

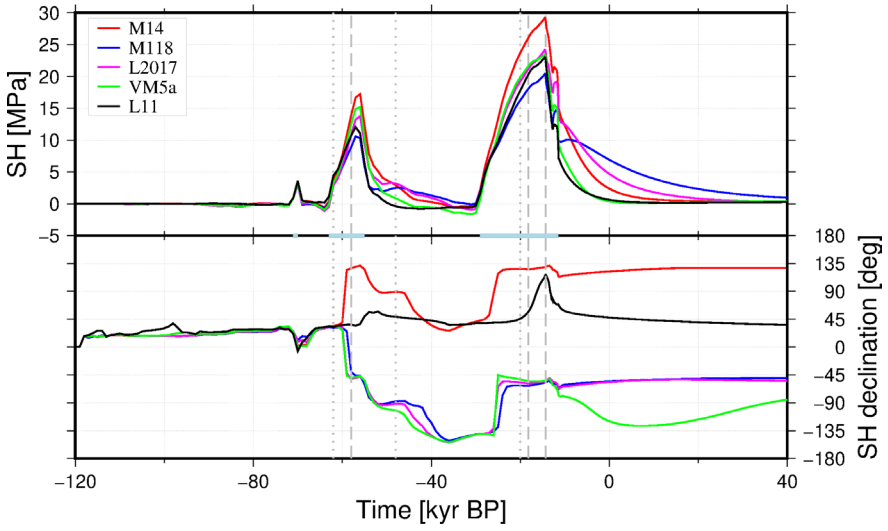

Figure 6-24. *Temporal evolution of maximum horizontal stress, S_H, upper panel, and S_H declination, lower panel, at 500 m depth beneath Forsmark for M14 (red), M118 (blue), L11 (black), L2017 (magenta) and VM5a (green) loaded by the UMISM Weichselian ice sheet reconstruction. Vertical dotted and dashed lines indicate times for which the ice sheet is seen in Figure 3-2 and Figure 3-3 (dashed) and Figure 3-4 and Figure 3-6 (dotted). Ice coverage at Forsmark is indicated by light blue bar at base of each plot.*

Stresses under the load of the RCP45 ice sheet at Forsmark (Figure 6-25) generally follow the trends seen for the larger NH40 and UMISM ice-sheets during ice-free periods as well as during ice-sheet advance and retreat. However, following the rapid advance of the ice sheet, the RCP45 ice sheet swaps into a more gradual phase of build-up locally at Forsmark, bordering a hiatus (Figure 3-4). During this time S_Z does not continue to increase as it is a direct response to the weight of the "regional" ice sheet thickness (regional here varies with elastic thickness of the lithosphere – a thicker lithosphere yields a larger flexural rigidity and hence promotes longer wavelengths of deformation. This implies that the area considered regional increases with increasing lithospheric thickness given comparable elastic properties). As a consequence, S_H grows larger than S_Z prior to the GM in all earth models except the L11. For M14, M118 and L2017 also S_h grows larger than S_Z prior to the GM, thus producing a reverse induced stress field.

The largest peak S_H (24.7 MPa) is again found in the M14 earth model (Figure 6-26, upper panel) but the smallest is now found in L11 (15.0 MPa). For all models peak S_H occurs at GM indicating that the models at this time are closer to isostatic equilibrium than was the case under the influence of the NH40 and the UMISM ice sheets. In the case of L11, the picture is consistent with L11 producing the smallest U_Z of all earth models loaded by RCP45 (Figure 5-2). As argued above, this is most likely due to the combination of a thickening of the lithosphere under Forsmark eastwards, coupled to a greater distance from Forsmark to the centre of the ice sheet, compared to the UMISM and NH40 cases. However, comparing Figure 5-2 and Figure 6-26 again highlights the danger in drawing too firm conclusions about the stress based on the vertical displacement. While the L11 earth model displays both the smallest U_Z and S_H at GM, the VM5a earth model displays the greatest U_Z but the second smallest S_H among the earth models at GM. It should further be noticed that the local ice thickness at Forsmark in RCP45 is only about 2/3 of the maximum ice thickness of the ice sheet at GM (Figure 3-4) in contrast to the NH40 and UMISM ice sheets where the local ice thickness at Forsmark at GM is about 9/10 of the maximum ice thickness of respective ice sheets. This will cause the S_H evolutions observed in the earth models loaded by the RCP45 ice sheet to deviate from the evolutions observed under the influence of the NH40 and UMISM ice sheets, as the geometry of the deformation field changes with respect to Forsmark, which will be located further up the flanks of the subsidence bowls with RCP45 compared to UMISM and NH40.

t_{max} under RCP45 follows the same pattern as was observed under the influence of the NH40 and UMISM ice-sheets. That is, t_{max} in Forsmark grows largest when the ice-sheet margin approaches the site to peak at the time when margin is just outside or right at the location. A clear expression for this can be seen from the elevated tmax already from the beginning and all the way up until the RCP45 ice-sheet reaches Forsmark after some 35 kyr. This is not seen for any of the other models. However, a quick comparison of the ice-sheet evolutions as seen in Figure 3-3 and Figure 3-4 it is noted that the RCP45 ice sheet grows fairly massive from onset. This is similar to the NH40 ice-sheet. But, where the NH40 margin prior to the first advancement in over Forsmark is always more than 500 km away from Forsmark, the RCP45 margin is only within 50–150 km away from Forsmark prior to its first migration in over the site. In fact, in all models except L11, t_{max} at 20 kyr matches or even slightly supersedes the peak t_{max} at later times.

S_H orientation induced by RCP45 (Figure 6-26, lower panel) in general also display the same trends as seen before with L11 having a roughly NE-SW direction throughout while for the other models an approximate NE-SW direction is observed prior to the first advance of the ice-sheet in over Forsmark and in-between the two periods of ice-coverage at the site. Once the ice-sheet start building up a significant mass over Forsmark the S_H orientation in all earth models except L11 flips by 90 degree to an NNW-SSE to NW-SE orientation. During the deglaciation S_H rotates into an approximate NE-SW orientation for the M14, L2017, and VM5a earth models followed by a rotation into a WNW-ESE orientation while in the M118 earth model the S_H orientation progresses directly from NW-SE into WNW-ESE with passing through a NE-SW orientation.

For the smaller ice sheets RCP45e and RCP85, normal stress evolutions beneath Forsmark are the opposite to those observed for the larger ice sheets in that horizontal stresses are negative during the glacial pulses at Forsmark, even during periods when the ice sheet margin advances in over the site (Figure 6-27 to Figure 6-30). For earth models M14, M118 and L2017, S_H becomes positive and hence greater than S_Z in the inter-stadial between the two major advances of both the ice sheets as well as during the post-glacial rebound following final retreat of the ice sheets, although the magnitudes are small (at most 0.7 MPa), the same applies for the VM5a loaded by RCP85. Of the earth models, L2017 displays the greatest negative as well as positive S_H and L11 the smallest. The peak negative S_H at Forsmark is found in L2017 and amounts to -4.3 MPa under the load of RCP45e and -1.3 MPa under the load of RCP85. Maximum horizontal tensile stresses, equal to S_h, at Forsmark reach -10.4 MPa and -3 MPa 2-3 kyr after the GM under RCP45e and RCP85 respectively.

For t_{max}, however, the evolution follows the same rules as seen for the larger ice-sheets, that is growth as the ice-sheet margin approaches Forsmark. For the S_H orientation (Figure 6-27 and Figure 6-30, lower panels) we note that we can group the earth models into two groups of similar trends, one containing the L11 and VM5a models and one containing the other models. The two groups still have large similarities (keep in mind while interpreting the declination plots that there is a 180-degree ambiguity in the plots). For the smaller RCP85 ice-sheet that never reaches Forsmark we find that the S_H orientation generally is either N-S or E-W with relatively quick 90-degree flips between. Under the larger load of the RCP45e ice-sheet which barely reaches Forsmark we see a larger variation of the SH orientations with a preference for either an NNE-SSW (M14, M118, L2017) or an NW-SE (L11, VM5a) at early times prior to the first build-up of the ice-sheet followed by rotation into an orientation gradually changing between E-W to NE-SW and back.

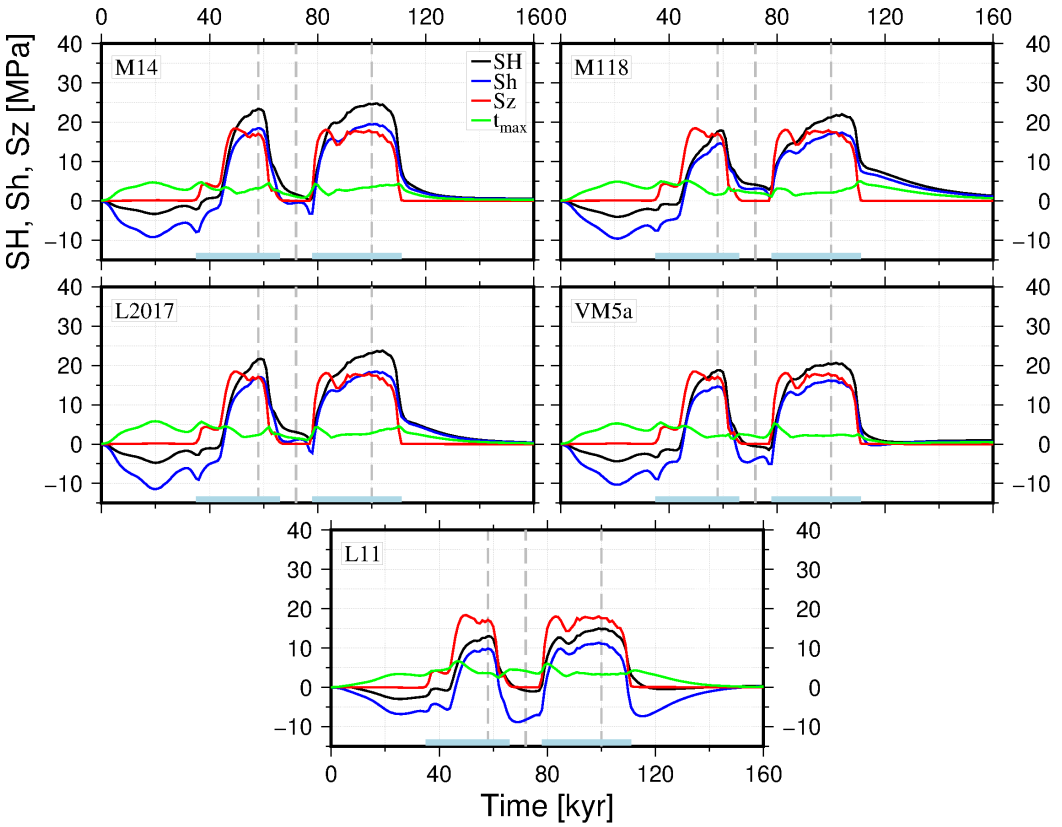

Figure 6-25. *Temporal evolution of maximum horizontal stress (S_H, black), minimum horizontal stress (S_h, blue) and vertical stress (Sz, red) at 500 m depth beneath Forsmark for all earth models, loaded by the RCP45 ice sheet projection. Vertical dashed lines indicate times for which the ice sheet is seen in Figure 3-4 and Figure 3-5. Ice coverage at Forsmark is indicated by light blue bar at base of each plot.*

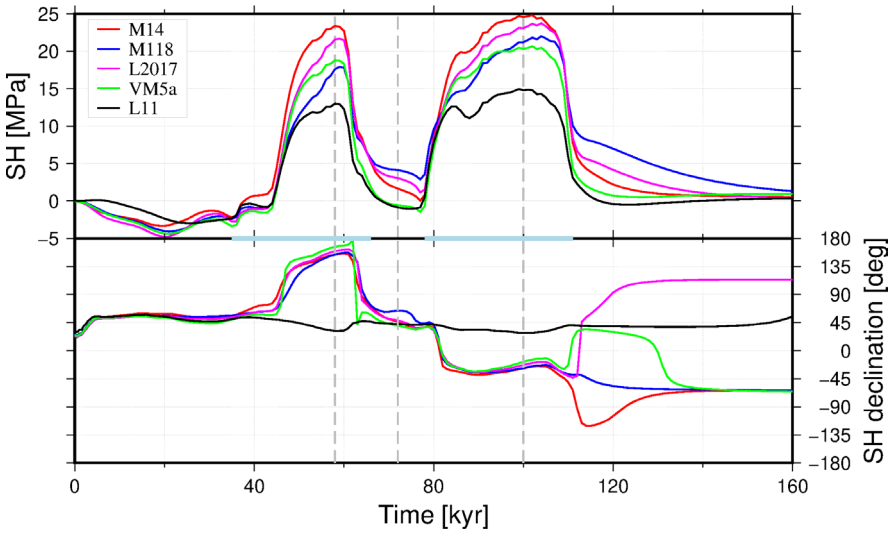

Figure 6-26. *Temporal evolution of maximum horizontal stress, S_H, upper panel, and S_H declination, lower panel, at 500 m depth beneath Forsmark for M14 (red), M118 (blue), L11 (black), L2017 (magenta) and VM5a (green) loaded by the RCP45 ice sheet projection. Vertical dashed lines indicate times for which the ice sheet is seen in Figure 3-4 and Figure 3-5. (dotted). Ice coverage at Forsmark is indicated by light blue bar at base of each plot.*

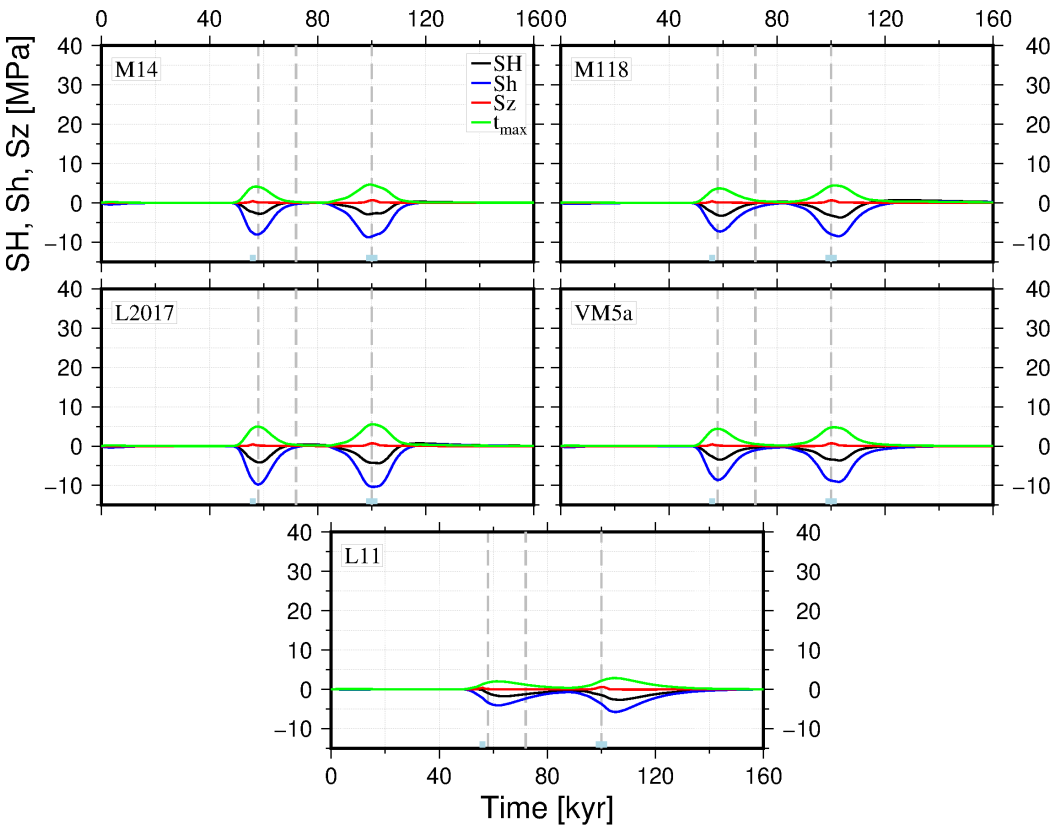

Figure 6-27. *Temporal evolution of maximum horizontal stress (S_H, black), minimum horizontal stress (S_h, blue) and vertical stress (S_z, red) at 500 m depth beneath Forsmark for all earth models, loaded by the RCP45e ice sheet projection. Vertical dashed lines indicate times for which the ice sheet is seen in Figure 3-4 and Figure 3-5. Ice coverage at Forsmark is indicated by light blue bar at base of each plot.*

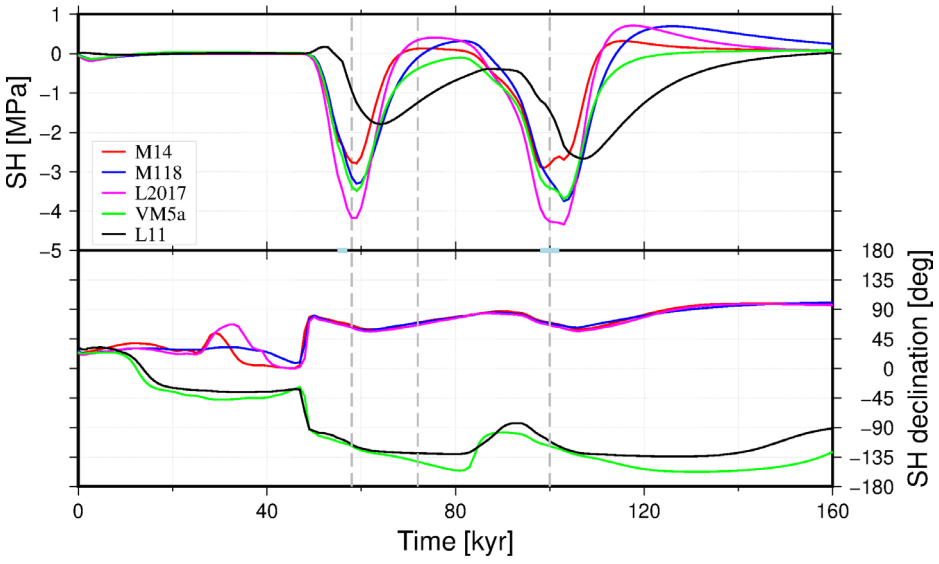

Figure 6-28. *Temporal evolution of maximum horizontal stress, S_H, upper panel, and S_H declination, lower panel, at 500 m depth beneath Forsmark for M14 (red), M118 (blue), L11 (black), L2017 (magenta) and VM5a (green) loaded by the RCP45e ice sheet projection. Vertical dashed lines indicate times for which the ice sheet is seen in Figure 3-4 and Figure 3-5 (dotted). Ice coverage at Forsmark is indicated by light blue bar at base of each plot.*

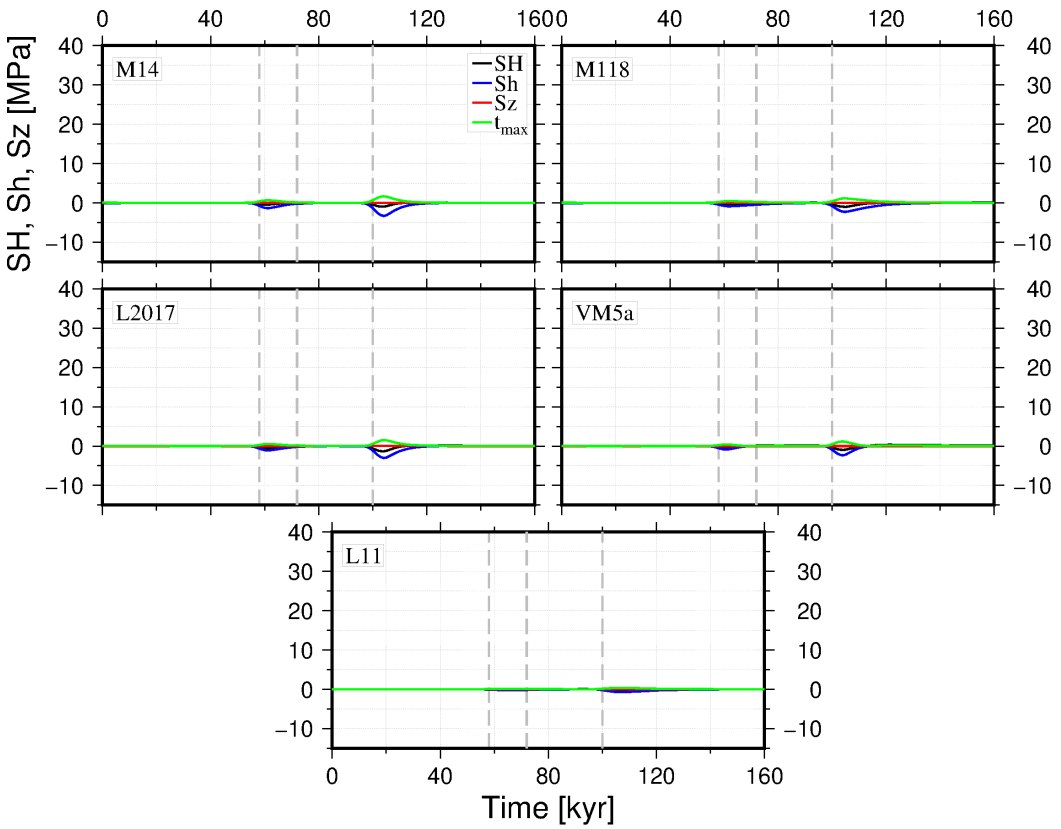

Figure 6-29. *Temporal evolution of maximum horizontal stress (S_H, black), minimum horizontal stress (S_h, blue) and vertical stress (Sz, red) at 500 m depth beneath Forsmark for all earth models used herein, loaded by the RCP85 ice sheet projection. Vertical dashed lines indicate times for which the ice sheet is seen in Figure 3-4 and Figure 3-5. The ice never reaches Forsmark.*

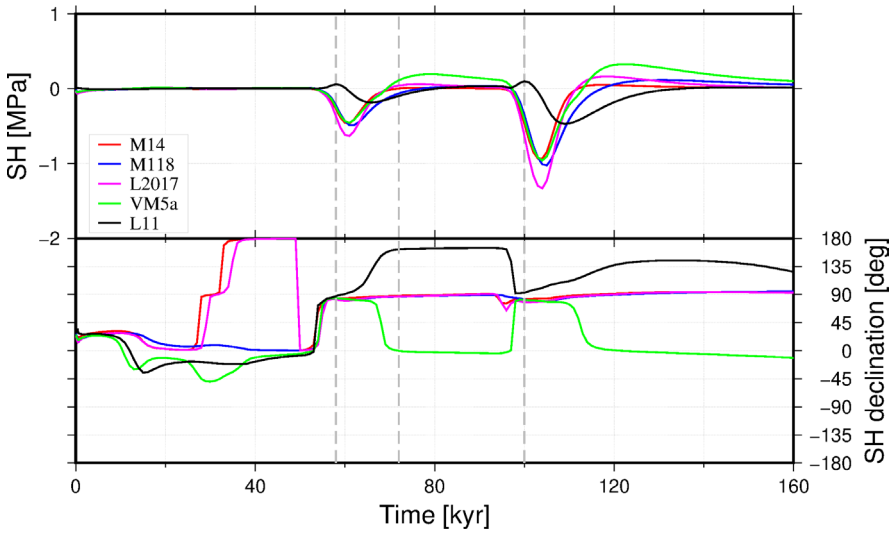

Figure 6-30. *Temporal evolution of maximum horizontal stress, S_H, upper panel, and S_H declination, lower panel, at 500 m depth beneath Forsmark for M14 (red), M118 (blue), L11 (black), L2017 (magenta) and VM5a (green) loaded by the RCP85 ice sheet projection. Vertical dashed lines indicate times for which the ice sheet is seen in Figure 3-4 and Figure 3-5 (dotted). The ice never reaches Forsmark.*

6.4 Impact of extended residence of ice at the glacial maximum

Using the ice models with a hiatus of 25 and 50 kyr (UMISM, NH40 and RCP45e) at the glacial maximum, we study how the maximum horizontal stress would evolve with prolonged residence times at the GM. Figure 6-31 displays S_H at 500 m depth beneath Forsmark in earth models M14, VM5a and L11 loaded by the original and perturbed ice sheets. The point in time at which the hiatuses are introduced is indicated. It is clear already from the original models with no hiatus' that the stresses are not at equilibrium at the glacial maximum, as they continue to change. For both NH40 and UMISM, S_H continues to increase during the hiatus but also for the unperturbed ice sheets an initial increase can be observed. This is more pronounced for the UMISM, as during the 3.9 kyr following GM relatively small changes in the overall volume and areal extent occurred but rather a redistribution causing growth in some places and thinning in other. As a consequence, the crustal stresses caused by the unperturbed UMISM actually grow larger than the stresses in the models with an introduced hiatus until a rapid thinning of the ice sheet starts at 14.3 kyr BP.

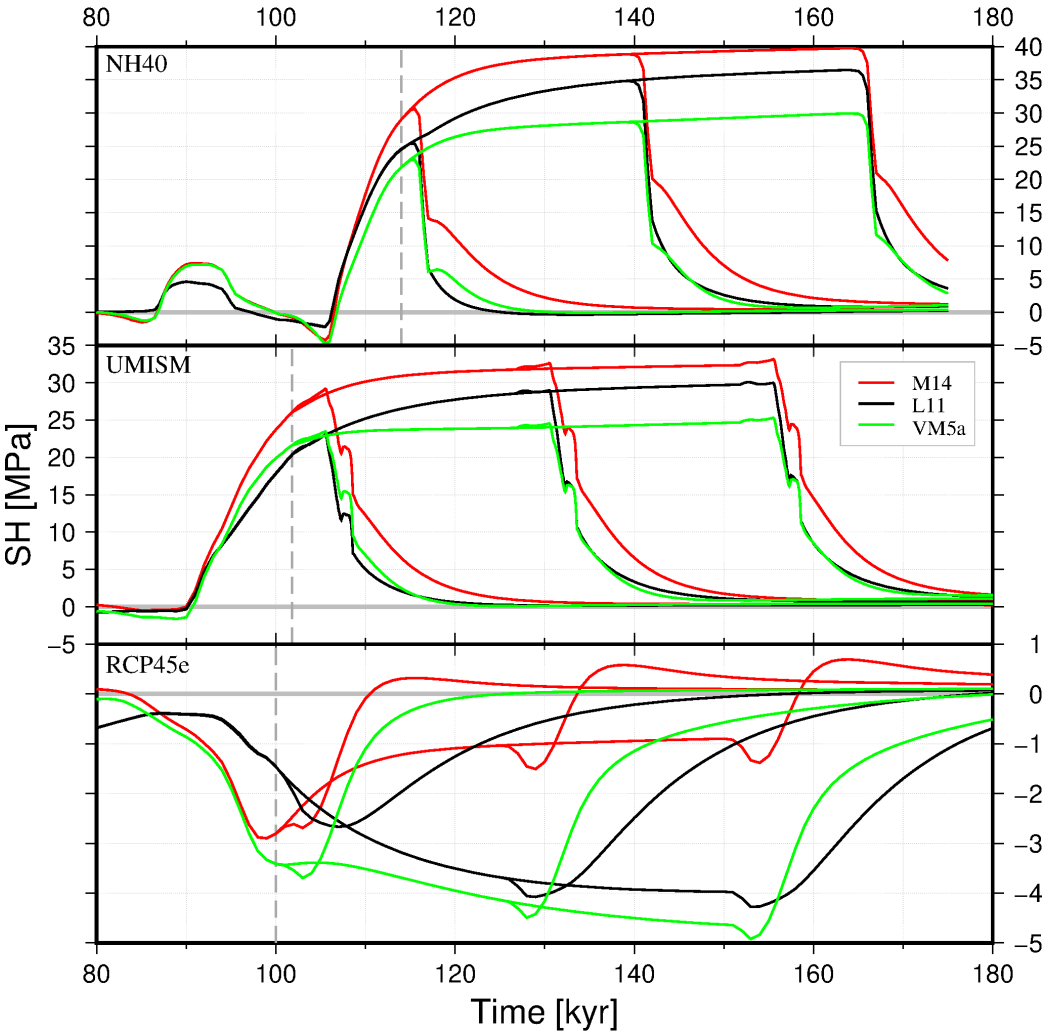

Figure 6-31. *Maximum horizontal stress (S_H) at 500 m depth beneath Forsmark for earth model M14 (red), L11 (black) and VM5a (green) loaded by the NH40 (upper panel), UMISM (middle panel) and RCP45e (lower panel) ice sheets with the original GM ice and the GM ice extended by 25 kyr and 50 kyr, from the time indicated by the vertical dashed line.*

The increase in stress following GM or the introduced hiatus in UMISM decrease with the duration of the hiatus but is still visible after a hiatus of 50 kyr, indicating that even after this period of time isostatic equilibrium has not been reached. This can also be seen directly from the evolution of the stress during the hiatus which has still not fully levelled out after 50 kyr, although for the VM5a the increase after 25 kyr is fairly small. The magnitude of the increase is clearly affected by the viscosity of both the upper and lower mantle, with VM5a displaying the faster approach to equilibrium (despite having the same viscosity in the upper mantle as M14) and the L11 the slowest.

Comparison of the stress evolution in the model loaded by the UMISM reconstruction and the NH40 also indicates that the crustal stresses induced by the NH40 ice sheet are further from isostatic equilibrium than those induced by the UMISM reconstruction. This is due to the much more rapid ice growth in NH40 prior to the glacial maximum compared to the UMISM.

Under the load of RCP45e, the development of S_H during the hiatus becomes more complex as was observed also for U_Z at Forsmark during the hiatus. At the start of the hiatus, S_H in Forsmark is negative. While S_H in L11 continues to decrease throughout the hiatus, in VM5a S_H initially increases slightly after which it decreases again. In M14, S_H instead increases throughout the hiatus. In conclusion, neither of the models have reached isostatic equilibrium after the 50 kyr hiatus although the M14 model is close. We note here that for L11 this conclusion would have been hard to draw based on an investigation of U_Z alone (Figure 5-5) which appears to have levelled off already approximately 17 kyr after the hiatus was introduced. This implies that stresses are better suited to determine whether or not a GIA process is close to, or has reached, isostatic equilibrium.

The evolution of S_H seen in Figure 6-31 may seem counter-intuitive when compared to U_Z as seen in Figure 5-5 and requires some further discussion. At the GM in RCP45e, Forsmark is located right at the margin of the RCP45e ice sheet (Figure 3-5). During a rapid build-up of an ice sheet the mantle will not have time to react and effectively adds to the instantaneous elastic thickness. With time, however, the viscous flow in the mantle reduces this effect and the effective flexural rigidity reduces to that of the elastic lithosphere. At the beginning of loading, the wavelength of deformation will therefore be longer. In a region around the margins of a growing ice sheet the land will initially subside but with time, as the wavelength of deformation decreases with the effective flexural rigidity, land may uplift again. Similarly, the curvature will change, increasing in some regions and decreasing in others. This temporal behaviour will decrease in magnitude with increasing elastic thickness of the lithosphere as well as be less pronounced in the case of a slow growth of the ice sheet. It will further be damped by a migration of the ice-sheet margin and hence will mainly be notable in the case of a hiatus in the ice sheet configuration preceded by a rapid growth of the ice-sheet. This is what we observe in the temporal behaviour of S_H during the introduced hiatus following GM in the RCP45e model. At GM the surface deformation curvature at Forsmark in the RCP45e model is concave, hence S_H is tensile. If the curvature increases S_H will decrease (become more tensile). In the case of M14 and at early times of the hiatus in VM5a, the effective elastic thickness is fairly large, placing Forsmark in a region where the curvature of the surface deformation decreases and S_H therefore increases (becomes less tensile). Conversely, further away from the ice sheet interior the curvature of the surface deformation increases. With time, the effective elastic thickness of the lithosphere in VM5a decreases, as the high-viscosity lower 40 km of the lithosphere deforms viscously. The wavelength of deformation then becomes shorter, bringing the region where the curvature of the surface deformation increases further in, eventually migrating in over Forsmark, hence turning S_H from increasing to decreasing and thus more tensile again. The L11 earth, as pointed out earlier, does locally have a greater elastic thickness than M14 but the rapid thinning of the lithosphere towards the ice-sheet interior results in an effective flexural rigidity which is lower than in the M14 model, bringing the region where the curvature of the surface deformation increases in over Forsmark.

6.5 Impact of multiple glaciations

To study the impact of multiple glaciations we compare the stresses induced by the RCP45 and the RCP45x ice sheets, where the latter is ice-free for the first 70 kyr and then ramped up linearly to the ice configuration at 73 kyr in the original RCP45 model. From 73 kyr the continued ice sheet evolution in the two models is identical. Figure 6-32 shows the maximum horizontal stress (S_H) at 2.5 km depth beneath Forsmark for the RCP45 and RCP45x ice histories for all earth models as well as their difference.

We see that the simulations with the full RCP45 ice history have a few MPa of remaining S_H at 70 kyr (in earth models M14, M118 and L2017), producing a difference with the RCP45e simulations. The difference in S_H between the two ice models decreases rapidly as the ice advances in the next glacial period. Only for earth model M118 is there an appreciable difference, of 8.6 %, in S_H magnitude at GM. During the de-glaciation phase, the S_H magnitudes are very similar between the RCP45 and RCP45x results, except for the stronger model M118, where there is slightly less than 1 MPa difference at the last time step of the ice model. If the model is allowed to continue to relax, as in Figure 6-32, the difference is about 230 kPa after an additional 40 kyr.

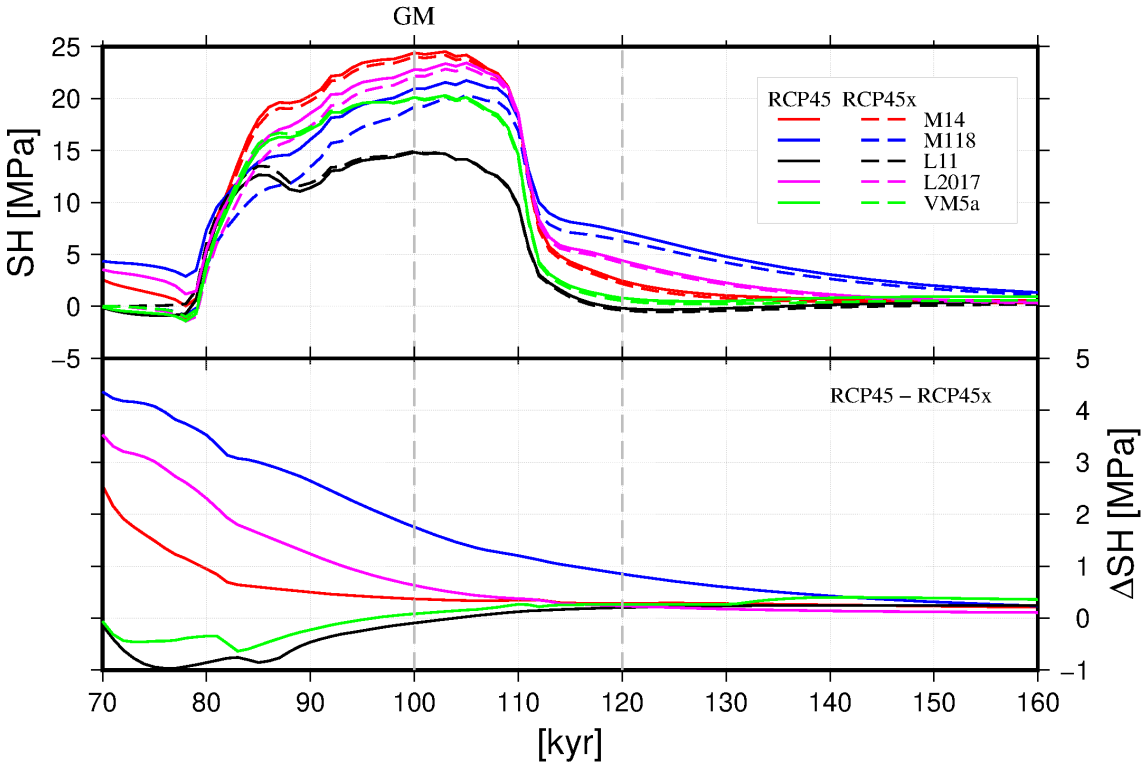

Figure 6-32. *Maximum horizontal stress (S_H) at 2.5 km depth beneath Forsmark for earth models M14 (red), M118 (blue), L11 (black), L2017 (magenta), andVM5a (green) (upper panel) loaded by the full RCP45 ice sheet (solid lines) and the RCP45x ice sheet without ice prior to 73 kyr (dashed lines) and SH difference between RCP45 and RCP45x for each earth model (lower panel). Vertical dashed lines indicate the glacial maximum, GM, and last time step of the ice model.*

7 Discussion

The focus of this report is an investigation into how glacially induced stresses in the crust at 500 m depth beneath Forsmark would vary with different types of future glaciations, from very large scale Saalian type ice sheets to much smaller ice sheets that do not cover Forsmark. It is important to note that the particular horizontal stress magnitudes presented in this report should not be taken as accurate predictions, but rather as indications on how induced horizontal stresses may relate to the loading stress, and how the stresses induced by different ice models in different earth models relate to each other. The vertical stress, which only depends on the weight of the ice column, is of course easily predicted given a specific ice sheet model.

The horizontal stresses obtained in the simulations depend on a number of factors, one of which is the methodology used for the GIA calculations. Our finite element methodology has the advantage that the earth and ice models can vary in three dimensions and that stresses can be easily extracted from the models. However, as pointed out already in L2009, the methodology uses a flat earth approximation and does not implement the effects of internal buoyancy and self-gravitation. The flat-earth approximation and exclusion of self-gravitation compensate each other (Amelung and Wolf 1994, Schotman et al. 2008) to a significant degree. We do include material compressibility, which alleviates some of the problems of the incompressibility assumed in the Wu (1992, 2004) methodology that we use, but internal buoyancy is not accounted for, which has some effect on the simulated displacements and stresses. Tests indicate that this may not be a significant issue (H. Steffen, private communication). We also do not include sea-level variations in our modelling but this is of lesser concern for locations under the ice sheet, and shore-line displacement is not the topic of interest. The new developments in methodology discussed in Section 2.2 can potentially provide more physically complete simulations in the future.

As the precise configuration and volume of the Weichselian ice sheet is not known, studies of GIA during and after the glaciation usually solve for both the ice reconstruction and the earth model. This couples a specific ice reconstruction to a specific earth model (e.g. Argus et al. 2014, Lambeck et al. 2017). In this study we use ice models that have been developed with rather general, and sometimes simplified, earth models. Specifically, none of the earth models used here were developed simultaneously with one of the ice models used here, although the M14, M118 and L11 earth models were selected based on their fit to the UMISM ice model (Schmidt et al. 2014). We do not see this as a problem for the current study as it is focused on an investigation of how different ice sheet evolutions affect the stress evolution in the earth, and we use five different earth models to capture a significant part of the variability associated with the uncertainty in the exact rheology and elastic composition of the Earth. We have seen here that earth models with varying lithospheric thickness or very strong mantle behave different to the three more “average” earth models, this should however not exclude these models as potentially closer to the correct description of the Earth. This is also why we will not assign any of the earth models as more appropriate than the other.

The earth models affect the stress evolution in the crust in two different ways. The elastic structure of the earth has a large impact on the magnitude of the induced horizontal stresses. We use data based on seismic velocities in the PREM model (Dziewonski and Anderson 1981) as our basis for the elastic structure, i.e. Young’s modulus and Poisson’s ratio. Using averages of these parameters over large depth sections can potentially produce unrealistically large stresses near the Earth’s surface. As shown in Table 4-2, we use a Young’s modulus of 64 GPa for the upper 15 km of the models. This is similar to what has been measured on rock samples from Forsmark (SKB 2005) but may be too high for the average stiffness of the rock mass at 500 m depth in Forsmark, considering the fractured nature of the uppermost crust. The second major influence on the stresses comes from the mantle viscosities, and the viscosity structure. Viscosity both affects the temporal evolution and the magnitude of the horizontal stresses, as we have seen here for the high viscosity lower mantle model M118. While the evolution and magnitude of crustal stresses and surface displacements are dependent not only on the mobility of the upper mantle but also on the (uppermost) lower mantle, the sensitivity to the lower mantle mobility diminishes with time. Currently available observational data and associated uncertainties can therefore only very crudely constrain the viscosity of the lower mantle beneath Fennoscandia, so estimates of lower mantle viscosity under Fennoscandia are rather variable (e.g. Schmidt et al. 2014).

The scenario used here to study the effect of previous glaciations on the displacements and stresses during subsequent glaciations involves two similar sized pulses of ice. In this scenario, Forsmark is covered by ice well before and during GM in both pulses and we find that the uplift due to the earlier glaciation is more or less counteracted by the subsidence under the later glaciation at and following the GM of the latter. However, one could also have considered scenarios where the size of glaciations differed significantly and/or Forsmark never being ice-covered during the glaciation (which would require a comparatively small sized glaciation). In the case where a smaller glaciation is followed by a significantly larger the conclusions drawn here should not change. However, in the case where a larger glaciation (e.g. an UMISM sized) is followed by a smaller one (e.g. a RCP85 sized) the effect of a previous glaciation could be larger than observed here and potentially also modify whether or not a fore-bulge would exist in the Forsmark area during the smaller glaciation or not. The potential effect of a previous glaciation will however decrease with an increased duration of the interglacial (while increase with the viscosity of the mantle). It is not unlikely that a smaller glaciation would also be associated with a longer interglacial, hence reducing the effect of previous glaciations. Any definite scenario would, however, need to be studied individually.

8 Conclusions

Summarizing stress maps and the stress evolution at Forsmark, we find that:

- the spatial distribution and temporal evolution of the glacially induced stress field is to first order dependent on the size and evolution of the ice sheet. Variations in how the Earth is modelled mainly affects the resulting stress magnitudes and to some degree also the areal distribution and temporal evolution.
- the ice load induces vertical stresses, S_Z, in the Earth which are directly proportional to the local thickness of the ice sheet. The magnitude of the induced horizontal stresses depends on the flexure of the lithosphere, which in turn depends both on the regional thickness of the ice sheet and on temporal evolution of the ice volume. Long residence times imply more time for viscous flow and thus shorter wavelength flexure, whether or not this leads to larger or smaller horizontal stresses depends on the proximity to the ice sheet margin. We see in the stress maps and the temporal evolution plots that while the ice sheet is present, the maximum horizontal stress S_H is generally lower than S_Z. In some models, however, S_H can reach a magnitude larger than S_Z at the GM, but we find that it does not significantly exceed S_Z in any of the earth models used here.
- tensional horizontal stresses develop around the edge of a stationary ice sheet, but also at a certain point as an ice sheet advance toward it. The magnitude of the tensional stress depends on the size, distance to and residence time of the ice sheet. We note for example that the large NH40 induces less tensional stress at Forsmark on advance than does the much smaller RCP45e ice sheet.
- ahead of the advancing ice sheet, and during ice growth at a point, the induced stress field is normal. Depending on ice evolution and earth model, the induced stress field develops to strike-slip and even reverse, if the ice is stationary during some time. During deglaciation, the stress state often develops into reverse, for locations that have been significantly ice covered.
- high mantle viscosity decreases the induced horizontal stress magnitudes and increases the response (relaxation) time of the system. Although the upper mantle viscosity exerts most of the effect on the Earth response, for larger ice sheets the viscosity of the (uppermost) lower mantle also plays a role in controlling the induced stresses.
- the highest compressive horizontal stresses induced in our suit of ice and earth models are produced by the NH40 Saalian type ice model and the M14 earth model, where S_H reaches 30.4 MPa at 500 m depth in Forsmark. The highest tensional stress occurs with the RCP45 ice model and the L2017 earth model, where S_h reaches -11.4 MPa.
- the GIA models are generally not in isostatic equilibrium at the GM. Prolonging the glacial maximum produces increased horizontal stress at sites well inside the ice-sheet margin, potentially to magnitudes greater than S_Z while at sites close to the margin horizontal stress may both increase and decrease. The evolution is to first order controlled by the effective elastic thickness of the lithosphere.
- a prior glaciation has some effect on the early development of stress during the next glaciation (depending on the time between glaciations), but the effect decreases during ice growth and is generally very small at the next glacial maximum.
- t_{max} in Forsmark generally increases when the ice-sheet margin approaches the site, and peaks just before or at the time the margin is at Forsmark. If, however, the increase in the ice-thickness at Forsmark is sufficiently fast and the Earth sufficiently stiff, t_{max} may continue to increase above the value attained at the time the ice-margin were located in Forsmark.
- The orientation of S_H in the L11 earth model under the load of the larger ice-sheets is surprisingly stable varying mainly between NNE-SSW to NE-SW orientation. For the other earth models under the same load the S_H orientation is typically the same as for L11 prior to the build-up of significant ice-load at Forsmark (> 500 m of ice) at which point the S_H orientation preferentially rotates into a NW-SE orientation. Under the load of the smaller ice-sheets S_H orientations tend to be either N-S or E-W, but deviations to this can be seen for both the smaller and larger ice-sheets studied herein.

References

SKB's (Svensk Kärnbränslehantering AB) publications can be found at www.skb.com/publications.

Abaqus, 2007. Abaqus manuals, version 6.7, SIMULIA. Available at: www.simulia.com

Amelung F, Wolf D, 1994. Viscoelastic perturbations of the Earth: significance of the incremental gravitational force in models of glacial isostacy, Geophysical Journal International 117, 864–879.

Argus D F, Peltier W R, Drummond R, Moore A W, 2014. The Antarctica component of postglacial rebound model ICE-6G_C (VM5a) based on GPS positioning, exposure age dating of ice thicknesses, and relative sea level histories, Geophysical Journal International 198, 537-563.

Artemieva I M, Thybo H, 2008. Deep Norden: Highlights of the lithospheric structure of Northern Europe, Iceland, and Greenland, Episodes 31, 98–106.

Bängtsson E, Lund B, 2008. A comparison between two solution techniques to solve the equations of glacially induced deformation of an elastic earth, International Journal of Numerical Methods in Engineering 75, 479-502

Colleoni F, Liakka J, 2020. Transient simulations of the MIS 6 Late Saalian Eurasian ice sheet. SKB TR-19-17, Svensk Kärnbränslehantering AB.

Comsol, 2021. Comsol Multiphysics. Available at: www.comsol.com, [28 October 2021].

Dziewonski A M, Anderson D, 1981. Preliminary reference earth model (PREM), Physics of the Earth and Planetary Interiors 25, 297–356.

Gasperini P, Sabadini R, 1990. Finite-element modeling of lateral viscosity heterogeneities and postglacial rebound. Tectonophysics 179, 141–149.

Hampel A, Lüke J, Krause T, Hetzel R, 2019. Finite-element modelling of glacial isostatic adjustment (GIA): Use of elastic foundations at material boundaries versus the geometrically non-linear formulation, Computers & Geosciences 122, 1-14.

Huang P, Steffen R, Steffen H, Klemann V, Wu P, van der Wal W, Martinec Z, Tanaka Y, 2023. A commercial finite element approach to modelling Glacial Isostatic Adjustment on spherical self-gravitating compressible earth models, Geophysical Journal International 235, 2231–2256, doi:10.1093/gji/ggad354

IPCC 2013, Climate Change 2013 – The Physical Science Basis: Working Group I Contribution to the Fifth Assessment Report of the Intergovernmental Panel on Climate Change. Cambridge University Press.

Johnston P, Wu P, Lambeck K, 1998. Dependence of horizontal stress magnitude on load dimension in glacial rebound models, Geophysical Journal International 132, 41-60, doi:10.1046/j.1365-246x.1998.00387.x

Kierulf H P, Steffen H, Barletta V R, Lidberg M, Johansson J, Kristiansen O, Tarasov L, 2021. A GNSS velocity field for geophysical applications in Fennoscandia, Journal of Geodynamics 146, 101845, doi: 10.1016/j.jog.2021.101845

Lambeck K, Purcell A, Zhao S, 2017. The North American Late Wisconsin ice sheet and mantle viscosity from glacial rebound analyses, Quaternary Science Review 158, 172-210

Latychev L, Mitrovica J, Tromp J, Tamisiea M, Komatitsch D, Christara C, 2005. Glacial isostatic adjustment on 3-D Earth models: a finite volume formulation, Geophysical Journal International 161, 421–444.

Liakka J, Lord N S, Kennedy-Asser A, Lunt D J, Williams C J, Näslund J O, 2024. Assessing future ice-sheet variability for long-term safety of deep geological repositories. Advances in Geosciences 65, 71-81.

Lidberg M, Johansson J, Scherneck H G, Davis J L, 2007. An improved and extended GPS-derived 3D velocity field of the glacial isostatic adjustment (GIA) in Fennoscandia, Journal of Geodesy 81, 213–230.

Lidberg M, Johansson J, Scherneck H G, Milne G A, 2010. Recent results based on continuous GPS observations of the GIA process in Fennoscandia from BIFROST, Journal of Geodesy 50, 8–18.

Lund B, 2005. Effects of deglaciation on the crustal stress field and implications for endglacial faulting: A parametric study of simple Earth and ice models. SKB TR-05-04, Svensk Kärnbränslehantering AB.

Lund B, Schmidt P, 2011. Stress Evolution and Fault Stability at Olkiluoto During the Weichselian Glaciation, Working report 2011-14, Posiva Oy, Olkiluoto, Finland.

Lund B, Schmidt P, Hieronymus C, 2009. Stress evolution and fault stability during the Weichselian glacial cycle. SKB TR-09-15, Svensk Kärnbränslehantering AB.

Martinec Z, 1999. Spectral, initial value approach for viscoelastic relaxation of a spherical earth with a three-dimensional viscosity – I. Theory., Geophysical Journal International 137, 469–488.

Mitrovica J X, Latychev K, Tamisiea M E, 2007. Time Variable gravity: glacial isostatic adjustment, in Herring T (ed). Treatise on geophysics 3. Amsterdam, Holland: Elsevier, 197-211.

Nordman M, Milne G, Tarasov L, 2015. Reappraisal of the Angerman River decay time estimate and its application to determine uncertainty in Earth viscosity structure, Geophysical Journal International 201, 811–822.

Past Interglacials Working Group of PAGES, 2016. Interglacials of the last 800,000 years, Reviews of Geophysics, 54, 162-219, doi: 10.1002/2015RG000482.

Peltier W R, 1974. The impulse response of a Maxwell Earth, Reviews of Geophysics and Space Physics 12, 649–669.

Pérez-Gussinyé M, Lowry A R, Watts A B, Velicogna I, 2004. On the recovery of effective elastic thickness using spectral methods: example from synthetic data and from the Fennoscandian Shield, Journal of Geophysical Research 109, B10409.

Pérez-Gussinyé M, Watts A B, 2005. The long-term strength of Europe and its implications for plate-forming processes, Nature 436, 381–384.

Priestly K, McKenzie D, 2006. The thermal structure of the lithosphere from shear wave velocities, Earth and Planetary Science Letters 244, 285–301.

Reusen J M, Steffen R, Steffen H, Root B C, van der Wal W, 2023. Simulating horizontal crustal motion of glacial isostatic adjustment using compressible Cartesian models, Geophysical Journal International 235, 542-553, doi: 10.1093/gji/ggad232.

Root B C, Tarasov L, van der Wal W, 2015. GRACE gravity observations constrain Weichselian ice thickness in the Barents Sea, Geophysical Research Letters 42, 3313–3320. doi: 10.1002/2015GL063769.

Schmidt P, Lund B, Hieronymus C, 2012. Implementation of the glacial rebound prestress advection correction in general-purpose finite element analysis software: Springs versus foundations, Computers & Geoscience 40, 97–106.

Schmidt P, Lund B, Hieronymus C, Maclennan J, Árnadóttir Th, Pagli C, 2013. Effects of present-day deglaciation in Iceland on mantle melt production rates, Journal of Geophysical Research 118, 3366–3379, doi:10.1002/jgrb.50273.

Schmidt P, Lund B, Näslund JO, Fastook J, 2014. Comparing a thermo-mechanical Weichselian Ice Sheet reconstruction to reconstructions based on the sea level equation: aspects of ice configurations and glacial isostatic adjustment, Journal of Geofysical Research, Solid Earth 5, 371–388, doi:10.5194/se-5-371-2014.

Schotman H H A, Wu P, Vermeersen L L A, 2008. Regional perturbations in a global background model of glacial isostacy, Physics of the Earth and Planetary Interiors 171, 323–335, doi:10.1016/j.pepi.2008.02.010, 2008.

Sigmundsson F, 1991. Post-glacial rebound and asthenosphere viscosity in Iceland, Geophysical Research Letters 18, 1131–1134.

Simon K M, Riva R E M, Kleinherenbrink M, Frederikse T, 2018. The glacial isostatic adjustment signal at present day in northern Europe and the British Isles estimated from geodetic observations and geophysical models, Solid Earth 9, 777–795, doi: 10.5194/se-9-777-2018.

SKB, 2005. Preliminary site description. Forsmark area – version 1.2. SKB R-05-18, Svensk Kärnbränslehantering AB.

SKB, 2010. Climate and climate-related issues for the safety assessment SR-Site, SKB TR-10-49, Svensk Kärnbränslehantering AB.

SKB, 2023. Post-closure safety for SFR, the final repository for short-lived radioactive waste at Forsmark. Climate and climate-related issues, PSAR version. SKB TR-23-05, Svensk Kärnbränslehantering AB.

Spada G, Barletta V R, Klemann V, Riva R E M, Martinec Z, Gasperini P, Lund B, Wolf D, Vermeersen L L A, King M A, 2011. A benchmark study for glacial isostatic adjustment codes, Geophysical Journal International 185, 106-132, doi:10.1111/j.1365-246X.2011.04952.x.

Steffen H, Wu P, 2011. Glacial isostatic adjustment in Fennoscandia - A review of data and modeling, Journal of Geodynamics 52, 169–204, doi:10.1016/j.jog.2011.03.002.

Steffen H, Kaufmann G, Lampe R, 2014. Lithosphere and upper-mantle structure of the southern Baltic Sea estimated from modelling relative sea level data with glacial isostatic adjustment, Solid Earth 5, 447–459. doi: 10.5194/se-5-447-2014.

Steffen H, Olesen O, Sutinen R, 2021. Glacially-triggered faulting, Cambridge University Press, 438 pp, doi: 10.1017/9781108779906.

Thölix L, Korhonen H, Ruosteenoja K, 2019. Climate Projections for Olkiluoto, Working report 2018-09, Posiva OY, Olkiluoto, Finland.

Vachon R, Schmidt P, Lund B, Plaza-Faverola A, Patton H, Hubbard A, 2022. Glacially induced stress across the arctic from the Eemian interglacial to the present - Implications for faulting and methane seepage, Journal of Geophysical Research, Solid Earth 127, e2022JB024272, doi: 10.1029/2022JB024272.

van der Wal W, Barnhoorn A, Stocchi P, Gradmann S, Wu P, Drury M, Vermeersen L L A, 2013. Glacial isostatic adjustment model with composite 3D earth rheology for Fennoscandia, Geophysical Journal International 194, 61–77, doi: 10.1093/gji/ggt099.

Vestøl O, Ågren J, Steffen H, Kierulf H, Tarasov L, 2019. NKG2016LU: a new land uplift model for Fennoscandia and the Baltic Region, Journal of Geodesy 93, 1759–1779, doi: 10.1007/s00190-019-01280-8.

Wessel P, Luis J, Uieda L, Scharroo R, Wobbe F, Smith W H F, Tian D, 2019. The Generic Mapping Tools Version 6. Geochemistry, Geophysics, Geosystems 20, 5556-5564, doi: 10.1029/2019GC008515

Wolf D, 1991. Viscoelastodynamics of a stratified, compressible planet: incremental field equations and short- and long-time asymptotes, Geophysical Journal International 104, 401–417.

Wong M C, Wu P, 2019. Using commercial finite-element packages for the study of Glacial Isostatic Adjustment on compressible self-gravitating spherical earth – 1: harmonic loads, Geophysical Journal International 217, 1789-1820.

Wu P, 1992. Deformation of an incompressible viscoelastic flat earth with power-law creep: a finite element approach, Geophysical Journal International 108, 35–51.

Wu P, 2004. Using commercial finite element packages for the study of earth deformations, sea levels and the state of stress, Geophysical Journal International 158, 401–408.

Wu P, Peltier W R, 1982. Viscous gravitational relaxation. Geophysical Journal of the Royal Astronomical Society 70, 435-485.

Zhao S, Lambeck K, Lidberg M, 2012. Lithosphere thickness and mantle viscosity inverted from GPS-derived deformation rates in Fennoscandia. Geophysical Journal International 190, 278-292, doi: 10.1111/j.1365-246X.2012.05454.x.